Phononic Metamaterials for Surface Acoustic Wave Sensing

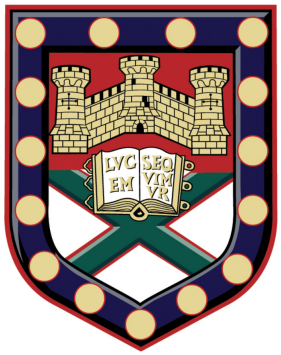

Jessica Frances Brown

A thesis submitted for the degree of
Doctor of Philosophy in Physics

in the

EPSRC Centre for Doctoral Training in Metamaterials
College of Engineering, Mathematics and Physical Sciences

October, 2022

Declaration

Submitted by Jessica Frances Brown to the University of Exeter as a thesis for the degree of Doctor of Philosophy in Physics in July 2022.

 I certify that all material in this thesis that is not my own work has been identified and that no material has previously been submitted and approved for the award of a degree by this or any other University.

I acknowledge financial support from the Engineering and Physical Sciences Research Council (EPSRC) of the United Kingdom, via the EPSRC Centre for Doctoral Training in Metamaterials (Grant No. EP/L015331/1).

Jessica Frances Brown

July 2022

Abstract

This thesis investigates the sensitivity of phononic metamaterials to the presence of materials and changes in their environment.

The behaviour of surface acoustic waves (SAWs) in periodic arrays of holes was investigated with finite element modelling and experimentally. SAW bandstructures and bandgap attenuation were obtained from simulations of arrays of cylindrical and annular holes which were filled with materials with different SAW velocities. Each type of hole array exhibited two distinct scattering regimes (Mie and Bragg scattering). The dependence of the bandgap frequency on the velocity was found to be stronger for annular holes than for cylindrical holes, suggesting that annular holes are potentially a better route to create tuneable phononic metamaterials. Annular holes also displayed a higher bandgap attenuation than cylindrical holes, meaning that annular hole arrays might be exploited for greater sensitivity in applications such as mass loading sensing.

SAW attenuation due to mass loading of air was calculated by measuring SAW amplitude on a SAW device using an oscilloscope system and by laser Doppler vibrometry (LDV). An extraordinary increase of 2 to 3 orders of magnitude in mass loading attenuation was observed at the bandgap frequency when a phononic metamaterial was present, with only 4 resonator elements needed to produce this result. The measurements obtained by both experimental systems displayed similar frequency dependencies of mass loading attenuation coefficients. Some mass loading effects were also reproduced using finite element modelling. These approaches show great promise for improving the sensitivity of SAW pressure sensors.

Finally, bandstructures were obtained from finite element simulations for an array of annular holes filled with a small sphere comprised of materials with different SAW velocities. The array exhibited similar scattering regimes as before, with an overlapping region. The dependence of the bandgap frequency on the velocity was found to be stronger when the annular holes contained the sphere than when they are fully-filled, suggesting that annular holes are potentially a good candidate for probing biological cells. Higher bandgap attenuation by up to a factor of 2 was exhibited by the single spherical inclusion compared to fully-filled holes. Since annular holes have more degrees of geometrical freedom than conventional phononic crystals, devices with greater sensitivity might be realised for applications such as biological sensing and lab-on-a-chip diagnostics.

Acknowledgements

They say it takes a village to raise a child and the same is definitely true of a PhD thesis! I'm so grateful to so many people for their support in getting me to this point. As with all acknowledgment sections there are too many to mention each by name, but I'd like to highlight a few people.

Firstly my thanks must go to my primary supervisor, Geoff Nash, for seeing something in me and giving me this opportunity in the first place, and for his kind and enthusiastic support and encouragement at every step of the way. I'd also like to thank members of the Nash Group, past and present - Hannah Barnard, Huanling Zou, Caroline Pouya, Prarthana Vadegadde Dakappa, Vicky Kyrimi, Milly Owens, Cheng Shi and Ben Ash - helpful discussions over many cups of tea in the office have made my PhD work better and more enjoyable! Thanks must also go to my second supervisor, Peter Petrov, for useful advice and food for thought in tying everything together.

Next I'd like to thank my friends and colleagues in the Metamaterials CDT, particularly those in the 2017 cohort - they've made my PhD journey less isolating, and also helped to give me something to look forward to every Friday afternoon after a long week of simulations!

My heartfelt thanks must go to Michael Graham and singers in the University of Exeter Chapel Choir, and the Chapel community - singing with the Chapel Choir has been an incomparable source of joy when times have been tough. I'm so grateful to have had so many wonderful musical experiences with them, and I know that they're heading towards amazing things. What a privilege to be part of such a legacy.

Closer to home, my family has had my back from the very beginning. Thank you to my parents, Jonathan and Rebecca, my sister Helen (who's inspired me with her own PhD journey) and my grandparents – without your unwavering encouragement and support, I'd have never been brave enough even to start this process, let alone power through and get to the end!

Finally, my fiancé Ed has been an absolute rock. Thank you for bringing me coffee (sometimes) and gin (often), and sitting with me while I stressed over the literature review and referencing – this thesis literally wouldn't been written without you, and for that I'll be grateful forever.

At the risk of sounding conceited, I'm very proud of myself for reaching this milestone - during my PhD journey I've faced a life-changing medical diagnosis, a broken knee, and a global pandemic amongst other obstacles - I'm so thankful for the people around me, named and unnamed, who've helped to support me throughout my PhD and beyond.

With gratitude,
Jessica

Contents

List of Figures

Chapter 1

Introduction

1.1 Context

Surface acoustic waves (SAWs) are elastic waves which propagate on the surface of solids. They were first proposed by Lord Rayleigh [1], who developed a mathematical description for them in 1885. There are several different types of SAW, including the Lamb wave [2] which oscillates in the direction of the surface plane normal, the Love wave [3] which oscillates parallel to the surface plane, and the Rayleigh wave [1] which has an elliptical oscillation, and is the SAW predominantly investigated in this thesis.

SAWs occur on many different length scales and surface materials, from earthquakes in the Earth's crust [3] to microchips in mobile devices [4]. White and Voltmer [5] invented the interdigital transducer (IDT) in 1965, which allowed microscopic SAWs to be generated more easily on piezoelectric substrates by applying an AC voltage across a pair of metal electrodes with interlocking fingers, transforming the way SAWs were generated and detected. This opened up the field, leading to an enormous range of diverse applications for SAW devices.

Introducing a pattern on the surface through which SAWs propagate can affect their behaviour [6] [7]. Attracting interest from the 1990's, phononic crystals are composite materials whose elastic properties are varied periodically [8], and they exhibit bandgaps where acoustic waves (including SAWs) of particular

frequencies cannot propagate, often caused by deconstructive Bragg interference [9]. Patterns tend to consist of elements such as parallel stripes [10] or square arrays of holes [11]. Phononic crystals with directional bandgaps were reported experimentally in 1998 by de Espinosa et al. [12], but a complete bandgap in all propagation directions was not realised until 2001 by Vasseur et al. [13]. This was then extended to SAWs in 2004 by Tanaka et al. [14], and for a piezoelectric lithium niobate substrate by Laude et al. in 2005 [15] as shown in Figure 1.1.

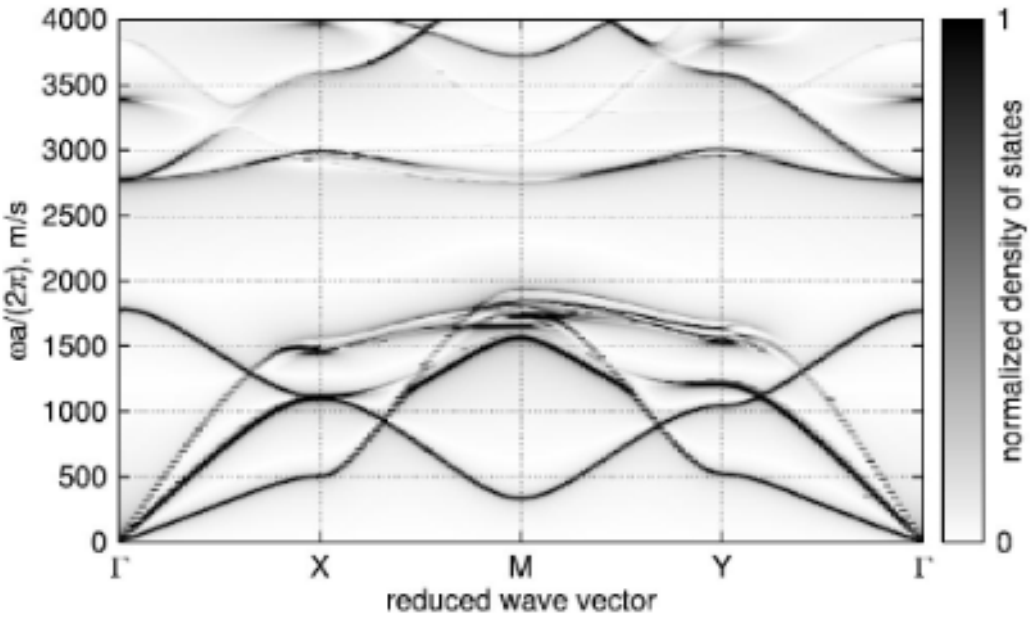

FIGURE 1.1: From [15]. The surface acoustic wave bandstructure for the $\Gamma - X - M - Y - \Gamma$ path in the first irreducible Brillouin zone, for a square array of circular holes in lithium niobate.

Changing the array element geometry can have a dramatic effect on the behaviour of the overall structure. For example, the bandgap frequency can be significantly lowered by the presence of a locally resonating component in the array, due to other scattering mechanisms (such as Mie resonance [16]) which contribute to acoustic energy loss. Olsson et al. [17] provided a brief mathematical explanation of bandgap origin in terms of Bragg and Mie scattering which has been used as the analytical model comparison for the bandgaps measured in this thesis. Pillars are the structure most commonly used to introduce local

resonance into phononic crystals. A locally resonant phononic crystal was first fabricated by Liu et al. [18], whose 'sonic crystal' structure consisted of sub-wavelength elements and exhibited exotic behaviours such as negative elastic constants and total wave reflection within a certain tunable frequency range, as shown in Figure 1.2.

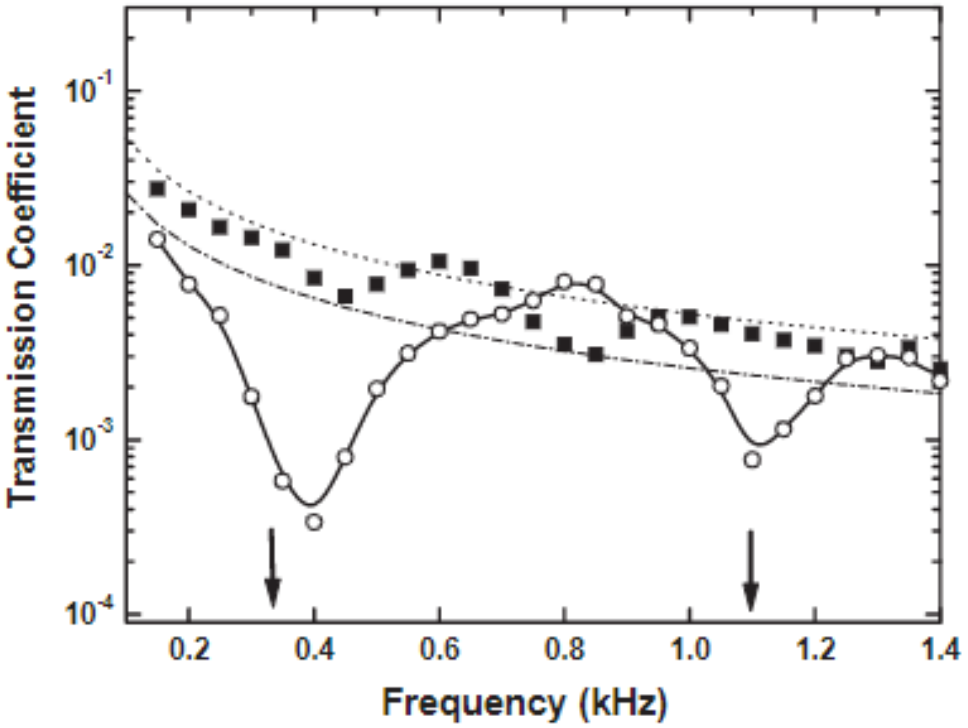

FIGURE 1.2: From [18]. Transmission coefficient plotted as a function of frequency. Opened dots (joined by the solid line) are the measured transmission amplitude for their 'sonic crystal' sample. The solid squares are the measured transmission amplitude for an epoxy sample with a random pattern of metallic particles 1 cm in diameter coated with silicon rubber on its surface. The dotted line and the dot–dashed line give, respectively, the calculated transmission amplitudes of an unpatterned epoxy slab and an unpatterned slab of the same density as the composite material containing the metallic particles. The two arrows indicate the calculated dip frequency positions (using the multiple scattering method [19]) for hexagonally arranged locally resonant units. The two dips in the 'sonic crystal' transmission represent bandgaps caused by negative effective elastic constants.

Other explorations of local resonance include Sainidou et al. [20], who were able to tune bandgaps by modifying the array element geometry by characterising the resonance modes responsible for bandgaps. Khelif et al. [21] were also able

to replicate the changes in bandgap characteristics following changes in the unit cell geometry, suggesting that this is a hallmark of local resonance. Importantly for this thesis, bandgap characteristics (such as frequency limits) were extracted at the X point of the first Brillouin zone (where wavenumber $k = 0.5$ in units of $\frac{\pi}{a}$), confirming that mode behaviour at this point is a fair representation of the full Brillouin zone, at least for square arrays of circular or cylindrical elements. Some mathematics behind the bandgap origin for locally resonant systems have been derived by Jia et al. [22] and Yip et al. [23]. Many other groups (such as Achaoi et al. [24], Sellami et al. [25]) have investigated local resonance as a phenomenon and have all replicated the reduction in bandgap frequency from modifying the unit cell to include a resonating element, as shown in Figure 1.3.

At this point, it is important to introduce the concept of metamaterials, which are artificial composite structures exhibiting properties and behaviours not found in nature. In a similar way to locally resonant structures, their behaviour is influenced more by the characteristics of the individual elements forming the overall structure, known as meta-atoms, rather than the properties of the base materials from which the elements and overall structure are comprised. They also tend to be periodic [26], with subwavelength distances separating the meta-atoms, giving rise to characteristics as observed in both conventional Bragg phononic crystals and also locally resonant phononic crystals. These include phononic bandgaps, also at lower frequencies due to the resonant frequencies of the meta-atoms being larger than the scale of the meta-atoms themselves.

These factors mean that metamaterials can be engineered to exhibit new behaviours, for example displaying negative refraction [27], and be double negative in that their permittivity and permeability are both negative [28]. The two previous examples were observed first for electromagnetic metamaterials, as they were discovered earlier, but have also been explored more recently for elastic metamaterials [29] [30]. Lu et al. [31] review some of the key differences between

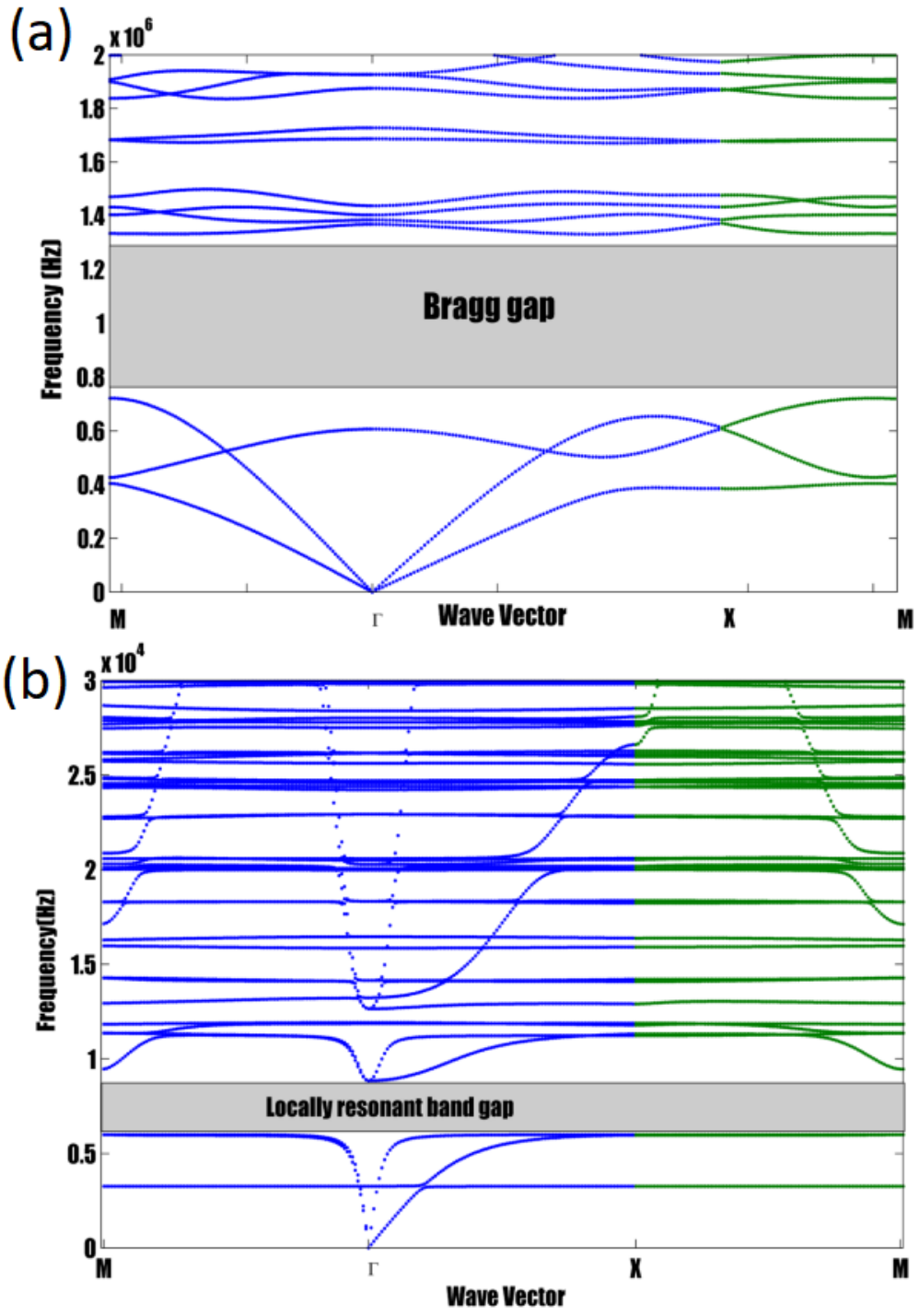

FIGURE 1.3: From [25]. The elastic wave bandstructure of (a) solid carbon cylinders and (b) hollow carbon cylinders arranged in a square epoxy resin lattice. The reduction in bandgap frequency can be clearly seen.

phononic crystals and elastic metamaterials.

For a number of years, SAW devices have been exploited for sensing purposes

since Rayleigh SAWs possess an out-of-plane component of oscillation. The sensitivity of a SAW device is typically quantified by measuring a shift in SAW velocity, frequency or phase as a function of various material parameters including mass, density, elastic moduli or pressure (for example) [32]. Sensing often takes place in a sensing layer located on top of the substrate, particularly for chemical sensing applications where molecules adsorb onto the sensing layer. Some applications where sensing occurs in layers were reviewed by Bo et al. [33], which include but are not limited to sensors for temperature, pressure and humidity. Some frequency shift-based pressure sensors have sensitivities of up to 8 kHz atm^{-1}. However, the addition of a sensing layer can increase the complexity in device fabrication and also may introduce misleading false positive or negative results [32], so avoiding a sensing layer where possible is beneficial for some applications. Sensitivity can also be extracted by measuring SAW attenuation, and is also typically achieved by quantifying shifts in SAW wave parameters as above. More specifically, mass loading attenuation in the presence of gas under different pressures can be induced on SAW devices. An expression for mass loading attenuation as a function of frequency and pressure (amongst other material properties) was derived in 1972 by Slobodnik [34].

Sensing can also be performed by patterned devices as an alternative to a sensing layer on a blank surface. Mehaney [35] developed a 1D phononic crystal-based sensor to measure properties (sound velocity, density, temperature and more) of a layer of biodiesel, located in a defect in the crystal structure. Khaligh et al. [36] measured the acidity of vinegar in a locally resonant cavity in a 2D phononic crystal structure comprised of circular holes, as shown via frequency shifts in Figure 1.4. Similarly Gharibi et al. [37] and Mehaney et al. [38] also induced locally resonant cavities in their 2D phononic crystal sensors in order to detect materials in or on the defects and measure their properties.

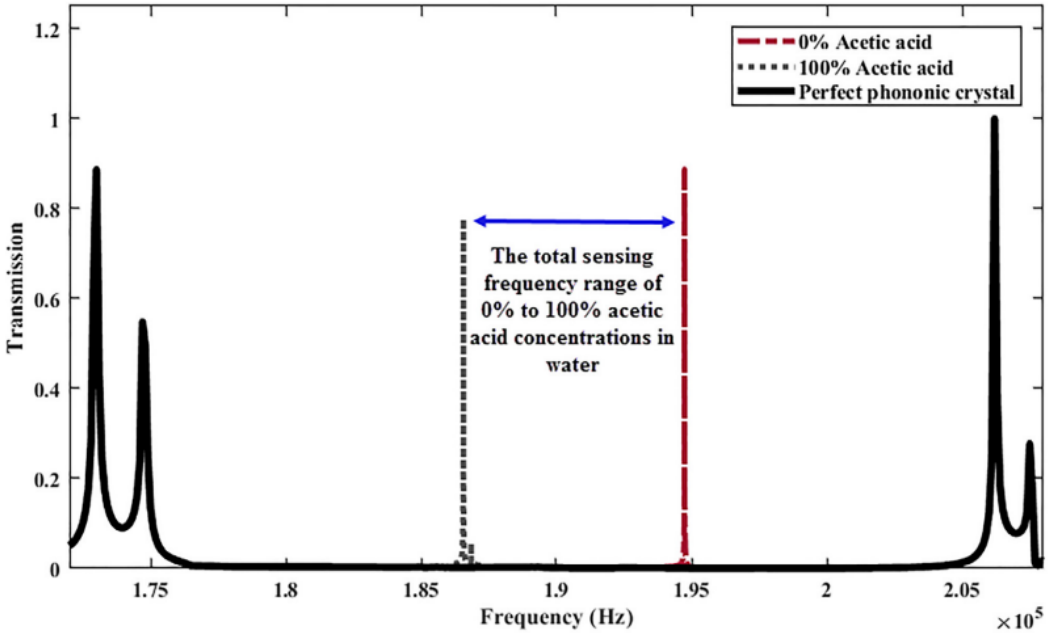

FIGURE 1.4: From [36]. The frequency bandwidth of the total sensing region for 0-100% acetic acid concentration, in the bandgap.

1.2 Motivation

In the majority of the work reviewed above, sensing and probing takes place within defects or cavities in the periodic structure. In this thesis, the sensitivity of hole phononic metamaterials is quantified when holes (annular and cylindrical) are filled with different materials of different geometries. This is in contrast to existing literature as the positioning of the object of interest is directly within the array elements themselves rather than in or on a non-patterned defect in the array. It is proposed that the work presented in this thesis are the first studies of sensing taking place directly from the inclusions in the array elements, rather than in a waveguiding cavity where acoustic energy is confined.

The annular hole geometry in particular could prove to be a very versatile candidate, scalable from micrometre length scales (as investigated here) to metres (such as for seismic applications), in order to be implementable for a wide range of sensing and probing applications. This work is proof of the concept that annular holes are sensitive to being filled directly, and the clear trends established

when the inclusion material properties are varied are further evidence of their applicability for realising more efficient and predictable sensing devices.

In terms of mass loading, a method of quantifying SAW mass loading attenuation is presented. This was achieved by directly measuring changes in SAW amplitude. Again, this work is proof of the concept that SAW mass loading attenuation can be quantified accurately in this way, as an alternative to more conventional approaches such as measuring shifts in SAW wave parameters.

1.3 Overview

The results of this thesis build upon the first study of annular hole phononic crystals performed by Ash et al. [39]. Using finite element modelling (FEM) and experiments, the sensitivity of these phononic metamaterials to the presence of materials and changes in their environment is investigated.

Chapter 2 contains an overview of the theory and mathematics behind the phenomena explored in this thesis. The SAW equation is derived and the Rayleigh wave solution introduced. Mechanisms behind mass loading attenuation are derived and explained. The method for calculating bandstructures (via eigenvectors and eigenfrequencies) in periodic structures such as phononic crystals is presented, followed by descriptions of some mechanisms (Bragg and Mie scattering) giving rise to bandgaps in phononic metamaterials. Finally, a brief overview of the annular hole phononic metamaterial predominantly investigated in this thesis can be found, which combines characteristics of Bragg and locally resonant phononic crystals.

The use of the finite element method (FEM) for modelling SAW bandstructures and propagation in phononic metamaterials is described in Chapter 3. This begins with an explanation of the basic working principles of FEM, such as discretisation, meshing and perfectly matched layers. COMSOL Multiphysics,

the FEM software package used in this thesis, is then described, with a focus on eigenfrequency and frequency domain studies to investigate the bandstructures and transmission respectively.

In Chapter 4, an explanation of the materials and methods used in experiments can be found, beginning with a description of the crystallography of lithium niobate ($LiNbO_3$), and the use of metal interdigital transducers (IDTs) to generate and detect SAWs on piezoelectric substrates. Next, the steps required for the preparation and fabrication of the SAW metamaterials investigated in this thesis are detailed, such as cleanroom preparation of substrates, focused ion beam (FIB) milling, scanning electron microscopy (SEM) imaging, and the mounting of the substrates on copper printed circuit boards. The experimental techniques for characterising and measurement of SAWs are then described, such as the oscilloscope system which sends and receives pulsed RF signals across the IDTs, and laser Doppler vibrometry (LDV) which is able to image the SAWs directly for amplitude measurements. A brief description of some data reduction and analysis techniques can also be found.

The first results presented in this thesis are detailed in Chapter 5, which is a computational study of the effects on the bandstructures and bandgap attenuation of cylindrical and annular holes in lithium niobate substrates, when the holes were filled with different materials. The main findings in this chapter were that each type of hole array exhibited a Mie scattering regime at lower inclusion material SAW velocity (V_i) and a Bragg scattering regime at higher V_i. The dependence of the bandgap frequency on the velocity was found to be higher for the annular holes than cylindrical holes, suggesting that the annular holes are potentially a better route for tuneable phononic metamaterials. In terms of the bandgap attenuation, the annular holes displayed higher values than cylindrical holes, suggesting that annular hole arrays also might lead to greater sensitivity in devices designed for applications such as mass loading sensing.

A study of mass loading effects in a phononic metamaterial is presented in Chapter 6, and includes experimental and simulation results. By measuring SAW amplitudes in air and in a vacuum, it was found that an extraordinary increase of up to 3 orders of magnitude in attenuation due to mass loading across an annular hole metamaterial array on a $LiNbO_3$ substrate (compared to an unpatterned $LiNbO_3$ surface) was exhibited at the bandgap frequency, and validated by an oscilloscope system, an LDV system and a computational study. The implication of these results is that annular holes are a potential candidate for improving the sensitivity of gas pressure sensors.

The final results presented in this thesis are described in Chapter 7, which is a similar study to that in Chapter 5 but with the inclusion geometry modified to a small sphere, intended to represent an analogue of a biological cell. Again, it was found that the array exhibited Mie-like, Bragg-like, and true Bragg scattering regimes at low, mid, and high V_i respectively. The dependence of the bandgap frequency on the velocity was found to be stronger when the annular holes contained the sphere than for when they were fully-filled, suggesting that the annular holes are potentially a good candidate for probing biological cell-like analogues. The bandgap attenuation was also calculated with respect to either a blank surface or empty holes. In the first case, higher bandgap attenuation was exhibited overall by the single spherical inclusion than by fully-filled holes. In the second case, annular holes appeared to be less sensitive to the presence of a single spherical inclusion compared to being fully-filled. Using annular hole arrays might give rise to devices with greater sensitivity for applications such as biological sensing and lab-on-a-chip diagnostics.

Finally, Chapter 8 summarises the results obtained in this thesis, and potential directions for future work are suggested.

Chapter 2

Surface Acoustic Waves, Phononic Crystals and Elastic Metamaterials

2.1 Overview

In this chapter, an overview of the background, theory and mathematics behind surface acoustic waves (SAWs), phononic crystals and metamaterials is presented. In section 2.2, SAWs are introduced and the SAW equation derived, and in sections 2.3 and 2.4 an mechanism affecting SAW propagation, mass loading, is discussed. Phononic crystals and local resonance are introduced in section 2.5 with an explanation of how SAW bandstructures are calculated, and how Bragg and Mie scattering can lead to the formation of bandgaps. In section 2.6 a brief overview of metamaterials is presented, with a focus on the annular hole geometry used throughout this thesis.

2.2 Surface Acoustic Waves

Rayleigh waves are a type of surface acoustic wave (SAW), so named after Lord Rayleigh who discovered them in 1885 [1]. They are elastic waves which

propagate on the surface of a solid, and possess both transverse and longitudinal components, meaning particles under the influence of the wave move in ellipses in the plane normal to the surface and parallel to the direction of propagation (as seen in Figure 2.1).

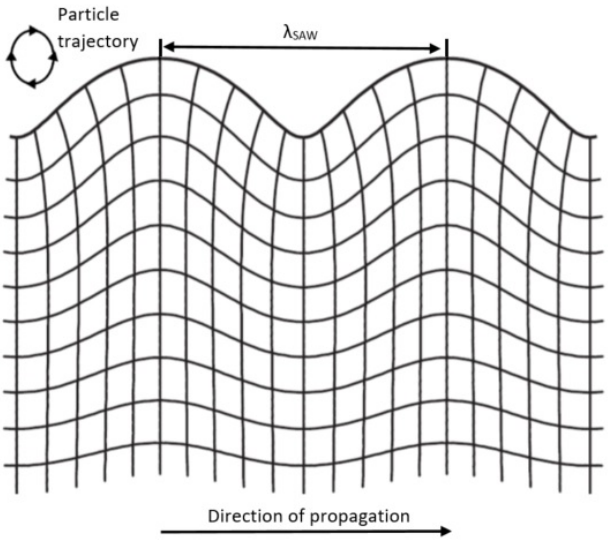

FIGURE 2.1: Reproduced from [40]. A diagram showing the propagation of a Rayleigh wave with elliptical particle motion. Each grid intersection point represents a particle.

They can occur on many scales, from earthquakes in the Earth's crust, to millimetre-scale lab-on-a-chip devices. Basic SAW devices for electronics applications have sizes on the order of centimetres, and typically support SAWs with amplitudes on the order of picometres and frequencies up to 1 GHz. They are fabricated by using photolithography to pattern metal interdigital transducers (IDTs) on piezoelectric substrates. Applying a voltage across the IDTs excites a mechanical response on the surface of the substrate, a SAW [5]. The surface acoustic wave equation can be derived by considering the piezoelectric effect in a homogeneous piezoelectric insulator [40].

2.2.1 SAW Equation Derivation

Material elasticity can be described by the displacement from the equilibrium position of a solid, strain S, and internal forces within it acting to restore the solid to a non-deformed state, stress T. Considering an element volume (much smaller than characteristic dimensions such as wavelength, and much larger than interatomic distances) with equilibrium position $\mathbf{x} = (x_1, x_2, x_3)$, displaced by amount $\mathbf{u} = (u_1, u_2, u_3)$, the strain can be defined by a symmetrical second rank tensor:

$$S_{ij}(x_1, x_2, x_3) = \frac{1}{2}\left(\frac{\partial u_i}{\partial x_j} + \frac{\partial u_j}{\partial x_i}\right) \qquad i, j = 1, 2, 3. \tag{2.1}$$

In a homogeneous insulating piezoelectric material, an applied electric field $\mathbf{E}$ induces strain components S_{ij} in the material, so the stress components T_{ij} are written:

$$T_{ij} = \sum_k \sum_l c^E_{ijkl} S_{kl} - \sum_k e_{kij} E_k \qquad i, j, k, l = 1, 2, 3. \tag{2.2}$$

where c^E_{ijkl} is the stiffness tensor for constant electric field and e_{kij} is the piezoelectric coupling coefficient which relates elastic fields to electric fields. Because of symmetry, indices i, j and k, l can be interchanged.

The displacement vector $\mathbf{D}$ also depends on strain S_{ij} as:

$$D_i = \sum_j \epsilon^S_{ij} E_j + \sum_j \sum_k e_{ijk} S_{jk} \qquad i, j, k = 1, 2, 3. \tag{2.3}$$

where ϵ^S_{ij} is the permittivity tensor for constant strain and e_{ijk} is the piezoelectric tensor. The electric field can be expressed in terms of the electric potential

Φ as $E_i = -\partial\Phi/\partial x_i$. Using Newton's second law, the equation of motion can be written:

$$\rho\frac{\partial^2 u_i}{\partial t^2} = \sum_j\sum_k\left\{e_{ijk}\frac{\partial^2\Phi}{\partial x_j\partial x_k} + \sum_l c^E_{ijkl}\frac{\partial^2 u_k}{\partial x_j\partial x_l}\right\} \tag{2.4}$$

where ρ is the density of the material.

The enclosed charge is zero as the material is an insulator ($\nabla\cdot\mathbf{D} = 0$) which reduces the equation to:

$$\sum_i\sum_j\left\{\epsilon^S_{ij}\frac{\partial^2\Phi}{\partial x_i\partial x_j} - \sum_k e_{ijk}\frac{\partial^2 u_j}{\partial x_i\partial x_j}\right\} = 0 \tag{2.5}$$

Displacements $\mathbf{u}$ and potential Φ have the form of plane waves in an infinite medium as follows:

$$\mathbf{u} = \mathbf{u}_0\exp[i(\omega t - \mathbf{k}\cdot\mathbf{x})] \tag{2.6}$$

$$\Phi = \Phi_0\exp[i(\omega t - \mathbf{k}\cdot\mathbf{x})] \tag{2.7}$$

Here, ω is the wave frequency, $\mathbf{k} = (k_1, k_2, k_3)$ and $\mathbf{u}_0$ and Φ_0 are constants. Substituting this into equations 2.3 and 2.4, four equations in the four variables u_1, u_2, u_3 and Φ are obtained. By setting the determinant of coefficients to zero, four solutions with different values of $\mathbf{k}$ are found. One solution is the electrostatic solution for an isotropic medium, while the others are non-dispersive acoustic waves.

Solutions are obtained for surface acoustic waves by defining a piezoelectric half-space shown in Figure 2.2.

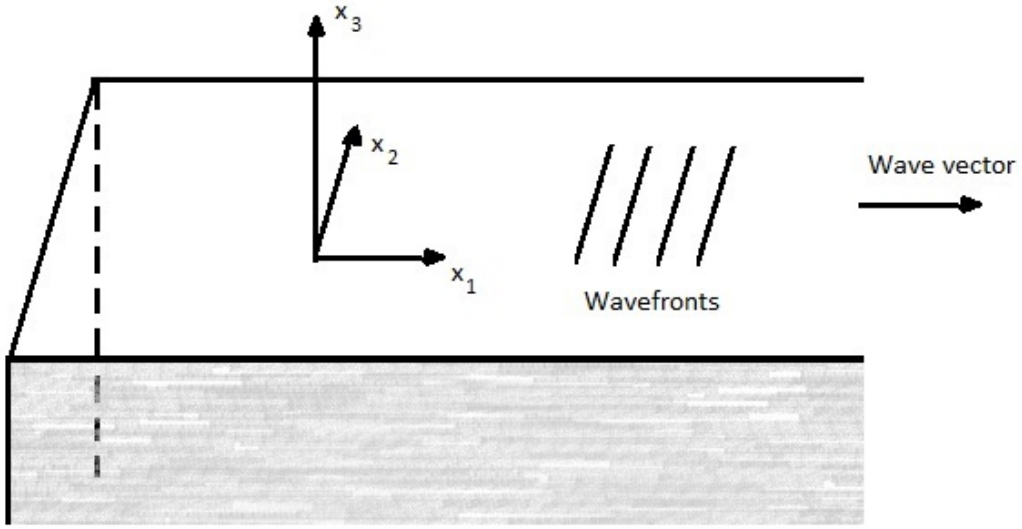

FIGURE 2.2: Reproduced from [40]. A schematic showing axes, wavefronts, propagation and media for piezoelectric half-space.

Conventionally the x_1 direction is the wave propagation direction and the x_3 direction is defined as being parallel to the outwardly-directed surface normal. The material is infinite in the x_1 and x_2 directions. Also by convention, the space is vacuum for $x_3 > 0$ and for $x_3 < 0$ the space is occupied by the material. The sagittal plane is the plane defined by the surface normal and wave propagation direction, the (x_1, x_3) plane. The wavefronts are parallel to the x_2 direction. A boundary condition is applied so there is no net force acting on the surface:

$$T_{13} = T_{23} = T_{33} = 0 \qquad \text{at} \quad x_3 = 0 \tag{2.8}$$

The continuity of electric fields must also be taken into account due to the piezoelectricity of the material. There are two surface cases, the first being where there is a vacuum above the material, the free-surface case, and the second being where a thin, infinitely conductive metal film of negligible weight is deposited on the material, known as the metallised case.

For a free surface, there is an electric potential in the vacuum satisfying the Laplace equation $\nabla^2\Phi = 0$. Φ can be written as:

$$\Phi = f(x_3)\exp[i(\omega t - \beta x_1)] \tag{2.9}$$

if β is the wavenumber.

Substituting this into the Laplace equation with the condition that Φ vanishes at $x_3 \to \infty$, the vacuum potential for $(x_3 \geq 0)$ is:

$$\Phi = \Phi_0 \exp(-|\beta|x_3)\exp[i(\omega t - \beta x_1)] \tag{2.10}$$

where Φ_0 is a constant. D_3 must be continuous at the interface between the medium and the vacuum since there are no free charges, meaning that for $x_3 = 0$:

$$D_3 = \epsilon_0|\beta|\Phi \tag{2.11}$$

For the metallised case, charges in the metal screen the electric field, meaning that $\Phi = 0$ at $x_3 = 0$.

Surface wave solutions are found by considering partial waves satisfying equations of motion in an infinite medium (Equations 2.3 and 2.4), either the free-surface or metallised case and Equation 2.7. Partial wave displacements $\mathbf{u}'$ and Φ' are of the form:

$$\mathbf{u}' = \mathbf{u}'_0 \exp(i\gamma x_3)\exp[i(\omega t - \beta x_1)] \tag{2.12}$$

$$\Phi' = \Phi'_0 \exp(i\gamma x_3)\exp[i(\omega t - \beta x_1)] \tag{2.13}$$

assuming β is real, $\gamma = f(V_l, V_t)$ is the wavevector x_3 component. V_l and V_t are the longitudinal and transverse wave velocities in the medium. If $\mathbf{u}'$ and Φ' are substituted into Equations 2.3 and 2.4, which are then solved numerically, eight γ values are found. Solutions are valid if the imaginary component of γ is negative as $\mathbf{u}'$ and Φ' are both required to be zero when $x_3 \to -\infty$.

Four γ values are valid, so partial waves are written as:

$$\mathbf{u}'_m = \mathbf{u}'_{0m} \exp(i\gamma_m x_3) \exp[i(\omega t - \beta x_1)] \tag{2.14}$$

$$\Phi'_m = \Phi'_{0m} \exp(i\gamma_m x_3) \exp[i(\omega t - \beta x_1)] \tag{2.15}$$

where $m = 1, 2, 3, 4$. In a half-space, it is assumed the solution is a linear sum:

$$\mathbf{u} = \sum_{m=1}^{4} A_m \mathbf{u}'_m \tag{2.16}$$

$$\Phi = \sum_{m=1}^{4} A_m \Phi'_m \tag{2.17}$$

where A_m coefficients are chosen to satisfy boundary conditions. Substituting Equations 2.16 and 2.17 into the wave equation, valid solutions are only found when values of β give a determinant of coefficients equalling zero. β is changed iteratively until this condition is satisfied. $\mathbf{u}$ and Φ are subject to a number of material characteristics including permittivity, stiffness, orientation and piezoelectricity. The most common SAW solution is elliptical motion in the sagittal plane, called the piezoelectric Rayleigh wave which is the solution which will be used. Other solutions, including the Lamb wave and the Love wave, are beyond

the scope of this work and will not be discussed as they do not have out-of-plane components of oscillation necessary for sensing applications.

There are no analytical solutions to the SAW equation, due to the complexity of the systems from which they are generated. Reasons include (but are not limited to) an unbounded surface in the vertical direction and piezoelectric coupling in very anisotropic substrates. Numerical methods must therefore be relied upon for theoretical investigation of the behaviour of SAWs, as discussed with a focus on the finite element method in Chapter 3.

SAWs are most commonly generated and detected using metal interdigital transducers (IDTs) patterned on piezoelectric substrates [5]. This is described in more detail in section 4.3 of Chapter 4.

2.3 Mass Loading Attenuation

SAWs can be attenuated through mechanisms such as boundary scattering or changes in elastic properties of propagation media, but in the presence of gases, liquids, or any other material present on the substrate surface, a process known as mass loading attenuation can occur. SAWs are particularly susceptible to mass loading attenuation due to their out-of-plane displacement component, and quantifying this sensitivity leads to applications in gas and pressure sensing and safety.

SAW mass loading attenuation can manifest itself through a number of mechanisms, but is commonly measured using a chemical adsorption layer on top of the substrate, through which chemical or conductivity changes caused by the external environment are measured through a frequency, velocity or phase shift of the SAW in an oscillator circuit after propagating through the adsorption layer. The attenuation can also be quantified by directly measuring SAW amplitudes.

2.3.1 Theory

Slobodnik [34] explored mechanisms behind attenuation due to gas loading, and proposed that the dominant source of attenuation is likely to be from the emission of compressional sound waves into the gas from the vibration of surface. These compressional sound waves are generated when the phase matching condition

$$\cos\zeta = \frac{\lambda_{gas}}{\Lambda_s} \tag{2.18}$$

is met, where ζ is the angle at which the compressional waves are launched and λ_{gas} is their wavelength, and Λ_s is the SAW wavelength. A schematic illustrating the compressional sound waves emitted into a gas from a SAW propagating on a solid-gas boundary, and the origin of the quantities used in Equation 2.18 can be seen in Figure 2.3.

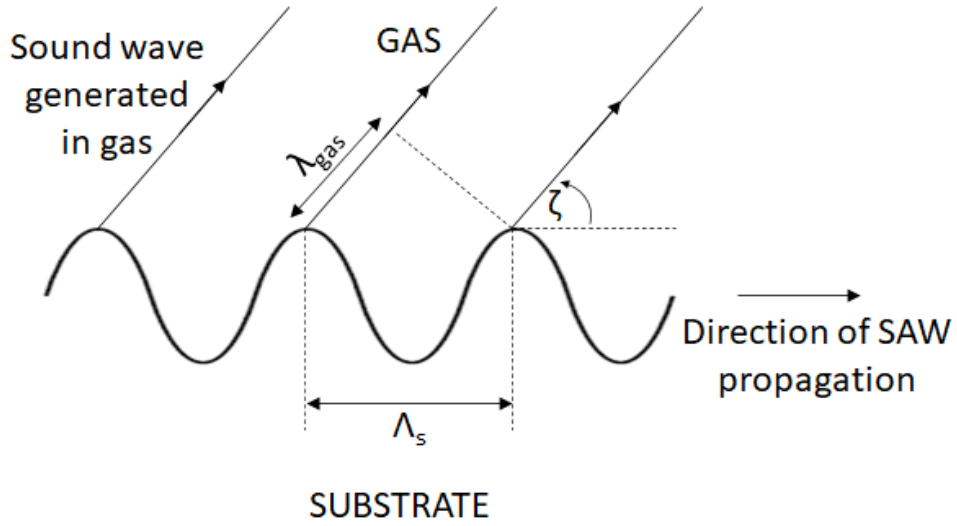

FIGURE 2.3: Adapted from [34]. A schematic illustrating the compressional sound waves emitted into a gas from a SAW propagating on a solid-gas boundary.

An approximate expression for the gas loading attenuation α was derived by Arzt et al. [41]:

$$\alpha = \frac{\rho_{gas} v_{gas}}{\rho_s v_s \Lambda_s} \tag{2.19}$$

where ρ_{gas} is the density of the gas, v_{gas} is the longitudinal speed of sound in the gas, ρ_s is the substrate density, v_s is the SAW velocity and repeated terms are defined above. Equation 2.19 can be rewritten in terms of frequency, pressure, temperature and atomic weight with a number of steps. Firstly, using the expression $f = v_s/\Lambda_s$ and relating the longitudinal speed of sound in the gas to its compression modulus (labelled λ by Slobodnik) $v_{gas} = (\lambda/\rho_{gas})^{1/2}$, Equation 2.19 can be rewritten as:

$$\alpha = \frac{f}{\rho_s v_s^2} \left(\rho_{gas} \left(\frac{\lambda}{\rho_{gas}} \right)^{1/2} \right) \tag{2.20}$$

For ideal gases and SAW frequencies below 1 GHz:

$$\rho_{gas} = \frac{MP}{RT} \tag{2.21}$$

$$\lambda = \frac{\gamma P}{K_s} \tag{2.22}$$

where M is the molar mass, P is the pressure, R is the universal gas constant, T is the temperature, K_s is the adiabatic compressibility and γ is the ratio of specific heats (constant pressure/constant volume). This allows Equation 2.20 to be rewritten in Np m^{-1} as:

$$\alpha = \frac{fP}{\rho_s v_s^2} \left(\frac{\gamma M}{RT} \right)^{1/2} \tag{2.23}$$

This equation for SAW mass loading attenuation was used as a theoretical baseline against which experimental results were compared in Chapter 6.

2.4 Phononic Crystals and Metamaterials

Phononic crystals (PnCs) are periodic composites analogous to photonic crystals, in that material properties (e.g. density and elasticity) are varied periodically. Typically this might involve fabricating holes in the crystal surface, and this can give rise to interesting waveguiding or lensing effects due to the presence of phononic bandgaps, where no waves can propagate.

PnCs can control acoustic and elastic waves, and can be characterised with band diagrams displaying phonon dispersions. Band diagrams are formed by calculating eigenfrequencies within the first Brillouin zone of a periodic structure with lattice vectors $\mathbf{a}_i$, $i = 1, 2, 3$. The first Brillouin zone is the primitive cell in reciprocal space, described by $\mathbf{G}$:

$$\mathbf{G} = m_1\mathbf{b}_1 + m_2\mathbf{b}_2 + m_3\mathbf{b}_3,$$
$$\mathbf{b}_1 = 2\pi\frac{\mathbf{a}_2 \times \mathbf{a}_3}{\mathbf{a}_1 \cdot (\mathbf{a}_2) \times \mathbf{a}_3}, \qquad \mathbf{b}_2 = 2\pi\frac{\mathbf{a}_3 \times \mathbf{a}_1}{\mathbf{a}_2 \cdot (\mathbf{a}_3) \times \mathbf{a}_1}, \qquad \mathbf{b}_3 = 2\pi\frac{\mathbf{a}_1 \times \mathbf{a}_2}{\mathbf{a}_3 \cdot (\mathbf{a}_1) \times \mathbf{a}_2}, \tag{2.24}$$

where $\mathbf{G}$ is the reciprocal lattice vector and m_i is an integer. Since SAW PnCs are periodic in only two dimensions, $\mathbf{a}_3$ is defined as the device surface normal, the unit vector in the x_3 direction. Bandgaps and other features can be identified by sweeping wavevectors over multiple directions within the Brillouin zone and presenting them on the same axis. By convention, wavevectors are swept as in Figure 2.4 if the structure is a 2D square array.

The wavevector $\mathbf{k} = \mathbf{k}_1 + \mathbf{k}_2 + \mathbf{k}_3$ is defined as $\mathbf{k}_i$ in the $\mathbf{b}_i$ direction. The Γ point, the centre of the Brillouin zone, is where the band diagram wavevector

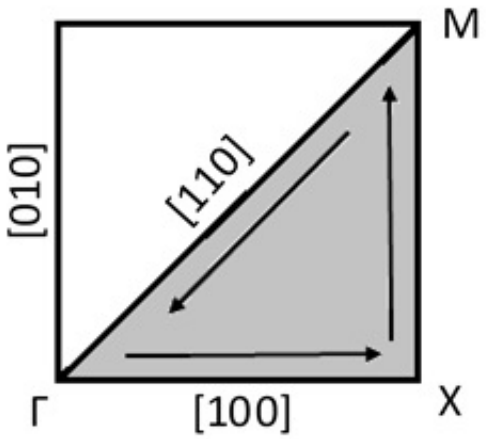

FIGURE 2.4: Sweeping wavevectors in the first Brillouin zone for 2D square arrays.

axis starts, at $|\mathbf{k}| = 0$. $\mathbf{k}_1$ is then increased to the X point, the [100] Brillouin zone boundary, then $\mathbf{k}_2$ is increased to the M point [110] boundary at constant $\mathbf{k}_1$. Finally, $\mathbf{k}_1$ is decreased to the Γ point.

Bloch theory [6] is used to calculate the eigenfrequencies. Displacement $\mathbf{u}$ at location $\mathbf{x}$ and time t are given the form:

$$\mathbf{u}(\mathbf{x}, t) = \exp[i(\mathbf{k} \cdot \mathbf{x} - \omega t)] \sum_{G} u_{\mathbf{k}}(\mathbf{G}) \exp(i\mathbf{G} \cdot \mathbf{x}) \tag{2.25}$$

In elastic composites, the wave equation is defined as:

$$\rho \frac{\partial^2 u}{\partial t^2} = \nabla_T \cdot (\rho c_T^2 \nabla_T u) \tag{2.26}$$

Here ρ is the mass density, c_T is the transverse wave speed and ∇_T is the 2D differential vector operator. The density and speed are functions of location since the structure is periodic, $\big(c_t(\mathbf{x}), \rho(\mathbf{x})\big)$. These can be Fourier transformed into $\rho(\mathbf{G})$and $\tau(\mathbf{G})$. Here $\rho c_T^2 = \tau(\mathbf{x})$. Equation 2.25 can be substituted into 2.26 yielding:

$$\sum_{\mathbf{G}'}[\tau(\mathbf{G}-\mathbf{G}')(\mathbf{k}+\mathbf{G})\cdot(\mathbf{k}+\mathbf{G}')-\omega^2\rho(\mathbf{G}-\mathbf{G}')]u_{\mathbf{k}}(\mathbf{G}')=0 \tag{2.27}$$

Consider a square array of cylinders (a ubiquitous PnC design) of material with density ρ_a in a background material with density ρ_b, with unit cell filling fraction f. Average parameters $\overline{\rho}$ and $\overline{\tau}$ and 'contrast' parameters $\Delta\rho$ and $\Delta\tau$ can be defined so that:

$$\rho(\mathbf{G})=\begin{cases}\rho_a f+\rho_b(1-f)\equiv\overline{\rho}, & \mathbf{G}=0\\ (\rho_a-\rho_b)F(\mathbf{G})\equiv\Delta\rho F(\mathbf{G}), & \mathbf{G}\neq 0\end{cases} \tag{2.28}$$

Here, $F(\mathbf{G})$ is the structure factor:

$$F(\mathbf{G})=A_c^{-1}\int_a d^2x\exp(-i\mathbf{G}\cdot x) \tag{2.29}$$

This is integrated over the cylinder cross section while A_c is the area of the unit cell. Using this, Equation 2.26 can be written:

$$[\overline{\tau}|\mathbf{k}+\mathbf{G}|^2-\overline{\rho}\omega^2]u_{\mathbf{k}}(\mathbf{G})+\sum_{\mathbf{G}'\neq\mathbf{G}}[\Delta\tau(\mathbf{k}+\mathbf{G})\cdot(\mathbf{k}+\mathbf{G}')-\Delta\rho\omega^2]F(\mathbf{G}-\mathbf{G}')]u_{\mathbf{k}}(\mathbf{G}')=0 \tag{2.30}$$

This is a set of linear, homogeneous equations of eigenvectors $u_{\mathbf{k}}(\mathbf{G})$ and eigenfrequencies $\omega(\mathbf{k})$ if $\mathbf{G}$ is allowed to take all possible values. Plotting the calculated eigenfrequencies as a function of wavevector (k) gives rise to the phononic bandstructure of a material or structure. If different filling fractions and materials are studied, bandgaps may be found.

2.4.1 Phononic Crystals

As discussed before, bandgaps prohibit waves of certain frequencies propagating through a crystal and can occur under a number of circumstances, leading to applications in frequency filters or wave confinement. Bandgaps can be formed when waves are scattered by changes in the density or wave velocity in a substrate. One important scattering mechanism is Bragg scattering, where peak constructive interference occurs in a periodic array of scatterers, such as holes as seen in Figure 2.5, when the Bragg law condition is met:

$$2d \sin\theta = n\lambda \tag{2.31}$$

Here d is the separation between the scatterers, n is an integer, λ is the wavelength and θ is the scattering angle [9]. A schematic of this process can be seen in Figure 2.6.

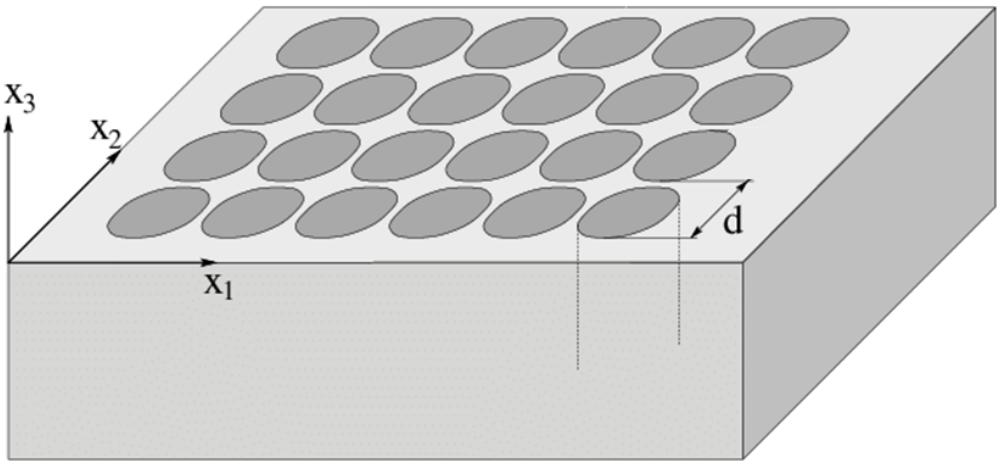

FIGURE 2.5: Adapted from [15]. A schematic of a conventional hole-based phononic crystal.

In conventional Bragg PnCs as discussed above, bandgaps are predominately caused by destructive Bragg interference due to the periodicity of the array elements preventing specific frequencies from propagating. SAWs of frequencies

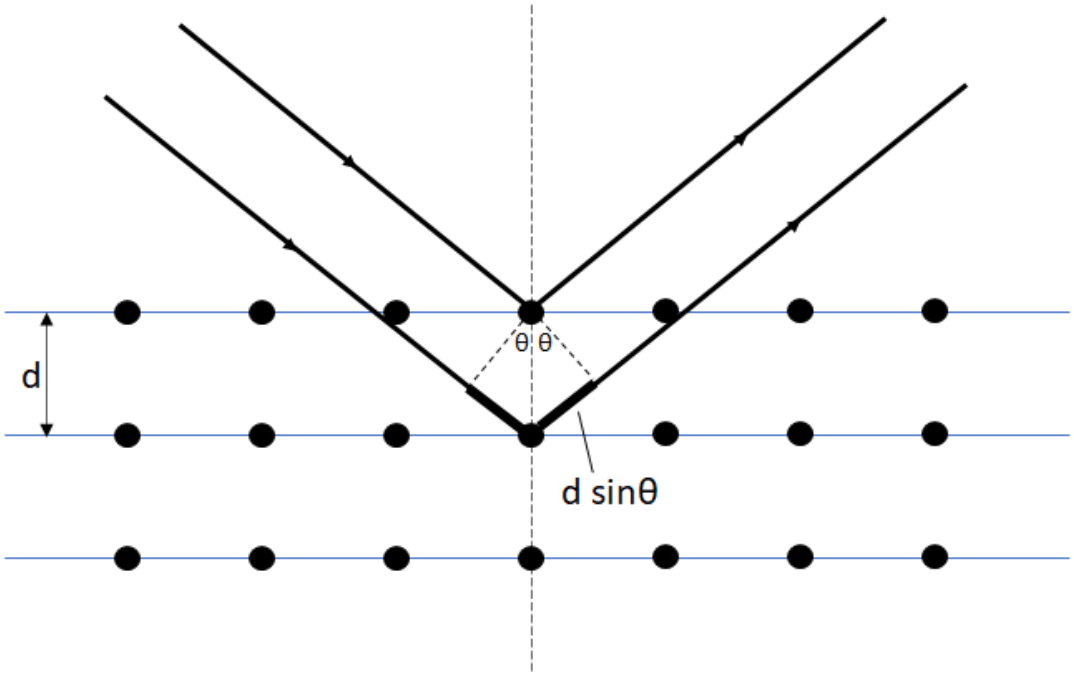

FIGURE 2.6: A schematic of the mechanism behind Bragg scattering and interference.

just above the bandgap are 'leaky', meaning that acoustic energy is transferred into the bulk of the material due to the coupling of SAWs to bulk waves which contributes to attenuation, but the mechanisms are not well understood [42]. The slowest bulk solution is known as the 'soundline', which is often plotted on bandstructure diagrams. SAW effects are often difficult to observe at frequencies close to the soundline, so integrating local resonators into PnC structures can play a part in engineering bandgaps by ensuring they occur at lower frequencies with respect to the soundline in the first Brillouin zone. This can increase the efficiency of devices by reducing the 'leakiness' of the SAWs and allowing SAW bandgaps to be observed and defined more easily. Examples of SAW bandstructure diagrams can be seen from Chapter 5 onwards.

2.4.2 Locally Resonant Phononic Crystals

When PnCs are fabricated with an array of resonators rather than just scatterers, local resonance is introduced into the system. An example of this is an array of cylindrical pillars (rather than holes in a Bragg phononic crystal).

Compared to conventional phononic crystals where the origin of the bandgap is predominantly from Bragg scattering, in locally resonant systems the characteristics of the individual array elements play more of a part in the bandgap origin, so for example the bandgap may evolve with pillar height.

Mie scattering [16], important in locally resonating systems, occurs when the diameter of the scatterers is comparable to the wavelength of the scattered wave (unlike Rayleigh scattering which is when the scatterer diameter is much smaller than the wavelength), is often a mechanism behind this. Mie scattering is also characterised by an asymmetry in scattering directions of the incident wave while Rayleigh scattering is isotropic. A simple schematic of Mie scattering can be seen in Figure 2.7.

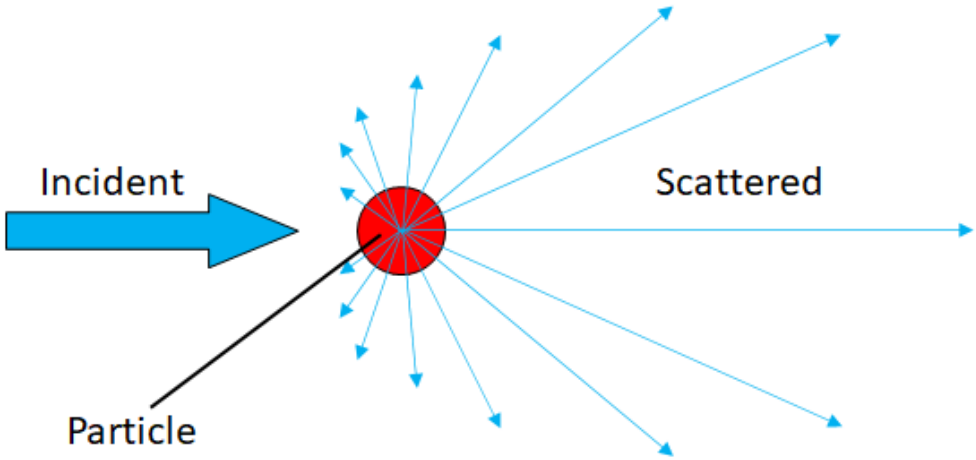

FIGURE 2.7: A schematic of Mie scattering.

In microfluidics, the Mie scattering regime can be important in describing the acoustic radiation force that droplets and particles experience. A general approach is to consider the theory of ray acoustics and Snell's law relating angles of incidence and reflection, to calculate acoustic fields and intensity profiles within fluids [43].

In this thesis, a simple but key difference between Bragg and Mie scattering is that Bragg scattering occurs between neighbouring array elements (i.e. between unit cells), while Mie scattering occurs across each individual array element (i.e. within a single unit cell).

2.5 Metamaterials

Metamaterials, which consist of meta-atoms, are composites that do not typically exist in nature. In recent years they have attracted much attention, particularly for electromagnetic wave applications. This is due to their exhibition of interesting behaviours such as negative refractive indices, which are achieved by the geometry and periodicity of the meta-atoms giving rise to resonant frequencies and wavelengths much larger than the scale of the meta-atoms themselves.

Elastic metamaterials operate on the same principle, in that material properties such as elastic moduli and mass density (rather than permittivity and permeability in, for example, the electromagnetic case) are modulated on length scales similar to the acoustic wavelength. This allows for the subwavelength (specifically) manipulation of elastic waves within the structure and leads to a number of novel effects including phononic waveguiding [44] and even acoustic cloaking [45].

2.5.1 Annular Hole Phononic Metamaterial

With bandgaps originating from both Mie and Bragg scattering, the array elements of annular hole phononic metamaterials consist of resonating pillars inside holes, which combine characteristics of both conventional phononic crystals and local resonating phononic crystals. Originally investigated by Ash et al. [39], finite depth annular holes are a novel structure which improve upon purely

hole-based phononic crystals by reducing fabrication time, and by lowering the bandgap compared to pillar-based locally resonating phononic crystals to avoid leaky SAWs. A schematic of the geometry can be seen in Figure 2.8. Also in terms of the geometry, the annular holes have another degree of freedom with two radii (labelled r_1 and r_2) compared to one of a conventional pillar-based phononic crystal, allowing for more precise tuning of phononic bandstructures if required. The annular holes also exhibit much higher bandgap attenuation than either hole- or pillar-based phononic crystals, pointing to applications in sensing environmental changes with fewer array elements required than previous device designs.

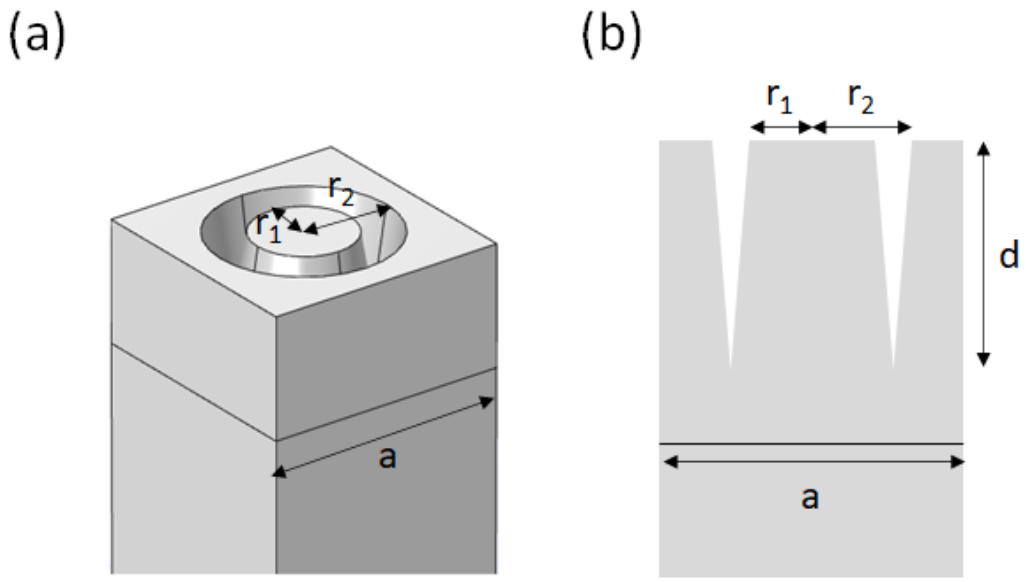

FIGURE 2.8: A schematic of the annular hole geometry in (a) 3D and (b) 2D. r_1 and r_2 are the inner and outer radii respectively, d is the depth and a is the lattice constant.

In this thesis, the annular hole geometry was adapted and the structure investigated in a number of ways. In Chapter 5, the bandstructures and bandgap attenuation of annular holes were compared to those of cylindrical holes when the holes were filled with materials of different SAW velocities. In Chapter 6, the mass loading on an annular hole phononic metamaterial was studied experimentally and computationally. In Chapter 7, a similar study to Chapter 5 is

presented, with the modification of the hole inclusion geometry so as it became a small sphere, intended to represent a biological cell-like analogue.

2.6 Summary

An overview of the background, theory and mathematics behind surface acoustic waves (SAWs), phononic crystals and metamaterials was presented in this chapter. SAWs were introduced in section 2.2 and the SAW equation derived, and an important mechanism affecting SAW propagation, mass loading was discussed in sections 2.3 and 2.4. These mathematics and mechanisms must be considered when applying in numerical models, as will be seen in Chapter 3. Section 2.5 introduced the concepts of phononic crystals and local resonance and an explanation of how SAW bandstructures are calculated, along with some mechanisms behind the formation of bandgaps. These are important concepts underlying the numerical modelling and design of the structures and devices used in later chapters. A brief overview of metamaterials was presented in section 2.6, focusing on the annular hole geometry used throughout this thesis.

Chapter 3

Finite Element Modelling with COMSOL Multiphysics

3.1 Overview

In this chapter, the principles of Finite Element Modelling (FEM) and methods for simulating surface acoustic wave (SAW) dispersions and propagation in phononic metamaterials are described. In section 3.2, FEM working principles such as meshing and perfectly matched layers are explored, while in section 3.3 a description of COMSOL Multiphysics, the FEM software package used for this thesis, can be found. Sections 3.3.1 - 3.3.2 contain descriptions of some methods used to simulate SAW dispersions in unit cell eigenfrequency models, and SAW propagation in frequency domain transmission models. A summary of the chapter can be found in section 3.4.

3.2 Background

Finite element modelling (FEM), or finite element analysis, is a powerful computational tool used by physicists, engineers and mathematicians to simulate and solve an enormous range of problems numerically [46]. When conventional

analytical methods are not suitable, such as problems involving complicated geometries or those without a straightforward analytical solution, FEM is a good technique to turn to. Boundary value problems for partial differential equations (PDEs) are solved, meaning that dependent variables (such as mechanical displacement or electric potential) have to satisfy PDEs in a domain of known independent variables and boundary conditions.

The principle behind FEM is for PDEs to be approximated with numerical model equations (NMEs), which are attained with discretisation, and so whose solutions are approximations of the real PDE solutions. Discretisation is achieved by dividing a larger continuous domain into discrete, non-differential finite elements, which are usually triangular or quadrilateral for 2D models, or tetrahedral for 3D models. NMEs are solved at element vertices, characteristic points lying on the element circumference called nodes, so that the dependent variable values can be explicitly calculated, and the element boundaries are connected to multiple other elements which then fill the entire geometry of the domain. The values of the dependent variables away from the vertices are approximated by using the solutions at each node.

FEM can support many different types of study step, such as time dependent where dependent variables evolve with time, frequency domain which represent a 'snapshot' of the model at chosen frequencies, or eigenfrequency studies for eigenmodes and eigenfrequencies for linearised models [47].

In an FEM model, the mesh is the group of finite elements which comprise the domain geometry, and meshing is the term for the process of building it. Important mesh characteristics to consider are the size, shape and distribution of the elements as these factors can have a major impact on the final model. The number of elements per unit space is known as the mesh density, which also profoundly affects both the accuracy and time of the solution, as a higher density mesh results in a more accurate solution but at the expense of computational

time and resources. An example of a course and sparse mesh compared to a fine and dense mesh where the domain geometry is better approximated which therefore results in better accuracy and higher resolution can be seen in Figure 3.1.

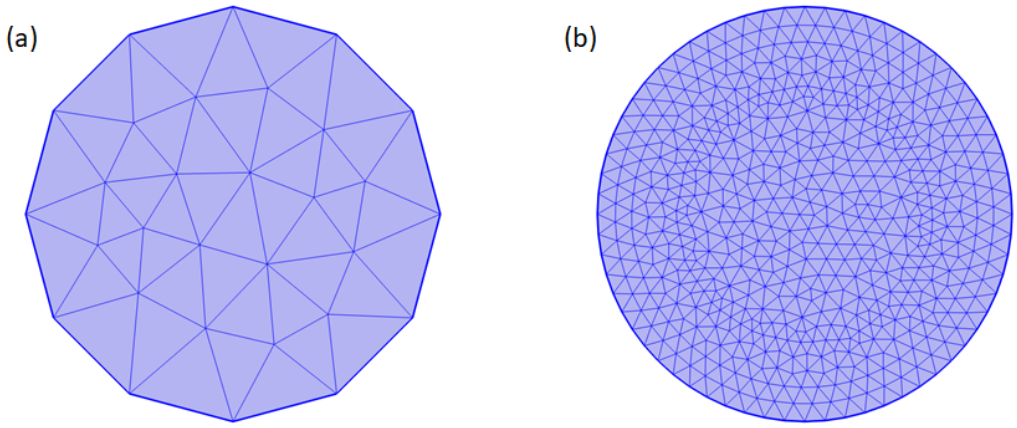

FIGURE 3.1: A mesh density comparison of a 2D circle with free triangular mesh elements for (a) a course, sparse mesh and (b) a fine, dense mesh, which better approximates the domain geometry.

The representation of waveforms is also important, so for any simulations involving waves, the minimum mesh density must be 5 finite elements per wavelength (of the highest frequency investigated). Optimising the density is called mesh refinement, and solutions are incrementally improved with an incrementally finer mesh. When the solutions stop changing as the mesh is made finer, the optimal mesh density is achieved. Curved geometries or sub-wavelength features may need a finer mesh density compared to the rest of the geometry, and mesh densities can be tailored to accommodate this while also reducing the number of finite elements and therefore solution time without sacrificing accuracy. Graded mesh distributions such as those seen in Figure 3.2 can also be exploited.

Finite elements are usually triangular/quadrilateral in 2D, and tetrahedral in 3D, meaning tessellation in complicated geometries is easy to achieve, and due to the high rotational symmetry of the resulting mesh, wave propagation or

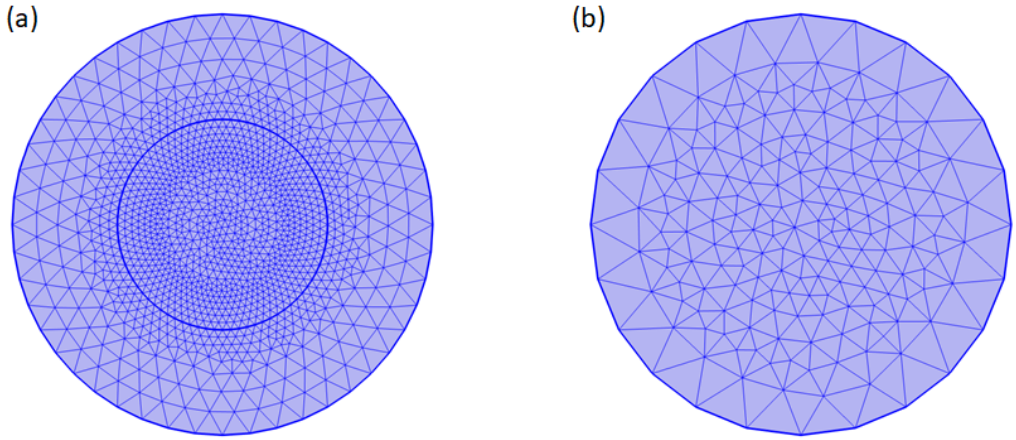

FIGURE 3.2: A mesh density comparison of a 2D circle with free triangular mesh elements for (a) a separate subdomain with an increased mesh density and (b) a single circular domain with a graded mesh distribution.

scattering can be accurately represented in all directions. When the direction of wave propagation is known or assumed such as in boundary layers (far from scattering), quadrilateral elements can be used which can minimise reflection. The elements on the face of such a layer can then be swept, where repeating layers matching those below are built, from a source face to a destination face. An example of this can be seen in Figure 3.3. Swept meshes must be used for perfectly matched layers (PMLs).

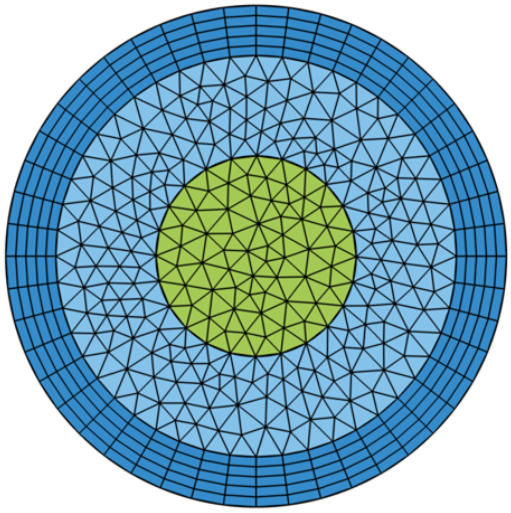

FIGURE 3.3: From [48]. FEM mesh of a 2D circle, with free triangular mesh elements in the inner subdomains and a swept quadrilateral mesh on the boundary subdomain.

In order to minimise spurious reflections at domain boundaries, virtual domains called perfectly matched layers (PMLs) are often used. These behave as a coordinate transform whose form is defined by a stretching function, which is calculated based on the wavelength of each simulation frequency and a 'typical' wavelength from the model [47] [49]. In a given direction, coordinate stretching is applied, and for stretching in a single direction, the complex displacement $\Delta\mathbf{x}$ is given as:

$$\Delta\mathbf{x} = \lambda f_i(\xi) - \Delta_w \xi \tag{3.1}$$

where λ is a typical wavelength, Δ_w is the PML domain width (defined in the geometry) and ξ is a dimensionless coordinate, varying from 0 to 1 over the PML domain. Two typical stretching functions are the polynomial $f_p(\xi)$, and the rational $f_r(\xi)$:

$$f_p(\xi) = s\xi^p(1-i), \tag{3.2}$$

$$f_r(\xi) = s\xi\left(\frac{1}{3p(1-\xi)+4} - \frac{i}{3p(1-\xi)}\right), \tag{3.3}$$

where p is the PML scaling factor and s is the PML curvature parameter. p scales the PML effective width, useful in scenarios where plane waves are incident at an angle so the PML must compensate for seeing a longer wavelength in the direction of stretching. s dictates the distribution of the mesh elements within the domain with the stretched coordinate, and increasing its value increases the density of mesh elements close to the PML inner boundary. If the wave field is comprised of many different wavelengths or a mixture of propagating and evanescent components, increasing the mesh resolution at the boundary

is required, at the expense of the requirement of more mesh elements in the domain itself. In order for a PML to be effective, the 3 parameters λ, p and s must be optimised through an iterative process analogous to refinement of the mesh.

The polynomial stretching function $f_p(\xi)$ has real and imaginary parts which are both finite and equal, meaning that this function is appropriate for simulations with many different wave types, since propagating and evanescent waves on a similar length scale are handled in a similar way. The effective thickness of the PML is scaled by the real part of the rational stretching function $f_r(\xi)$ to a quarter of the typical wavelength, while the imaginary part attenuating the waves is stretched towards infinity. This means that any propagating wave will be absorbed perfectly by the PML if the mesh resolution is sufficient, so this stretching function is appropriate for simulations with propagating waves with a mixture of wavelengths and incident angles.

By definition finite element models must have finite sized geometries, so domain truncation is needed to fulfil this. Using PMLs is a way of achieving this, for example for models simulating free space without having domain boundaries exhibit spurious reflections. Implementing stretching functions in elastic fields for example is comparable to anisotropic and complex values of densities and elastic moduli in domains, so the PML domains must replicate this anisotropy in order for perfect absorption without reflection to be successful [50]. A circular/spherical domain surrounded by a square-shaped/cubic PML domain with correct mesh can be seen in 2D and 3D in Figure 3.4, where the mesh on the boundaries of the real domains is swept to the exterior of the virtual PMLs with quadrilateral elements. Corner boundaries of square domains must be separate from the remaining PMLs in order to be successful.

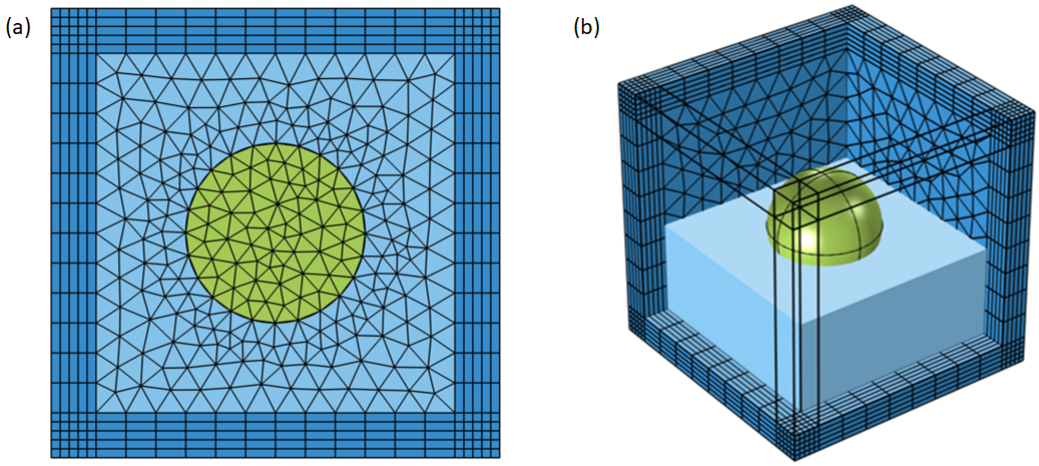

FIGURE 3.4: From [48]. FEM meshes of a (a) 2D circle and (b) a 3D sphere, both with free triangular/tetrahedral mesh elements in the inner subdomains and a correct swept quadrilateral mesh on the PML virtual domains (coloured darker blue), minimising spurious reflections at the real domain boundaries (coloured lighter blue).

3.3 COMSOL Multiphysics

In this thesis, COMSOL Multiphysics was the FEM software package used for all simulations. COMSOL has a huge number of modules specific to different physics applications, such as the Acoustics module, Electrostatics module, Solid Mechanics module, the Particle Tracing module, and many others. Each physics module has a number of default and additional parameters which can be set up, defined and varied as desired. Each module can also be used alone or be coupled with other modules via Multiphysics interfaces, which allows a vast array of physics problems to be simulated. The piezoelectric effect, for example, can be simulated by coupling the Solid Mechanics and Electrostatics modules.

Most COMSOL models are constructed through the same process, by firstly defining the spatial dimension (2D, 3D or 2D axisymmetric) and then choosing the physics modules. Then, definitions can be specified, such as global or geometric parameters, lattice vectors, global variables (functions of defined parameters i.e. reciprocal lattice vectors) or any material properties which need to be entered manually. PMLs can also be defined here, along with anisotropic

material domains requiring a custom coordinate system to define a crystallographic axis.

Once the domain geometry has been constructed, each subdomain has material properties applied, which are either chosen from a library of commonly used pre-defined materials, or defined manually. The physics modules then need relevant physics conditions to be applied, such as boundary conditions (periodic conditions, fixed displacement constraints) and domain conditions (volume forces, material models). Depending on the physics modules and boundary conditions, multiphysics coupling is then applied as necessary. The mesh is then built and study steps are selected from a list including the eigenfrequency study, frequency domain study, time domain study and stationary study amongst others. A parametric sweep can also be applied which sweeps through a range of values of chosen parameters from the definitions and repeats simulations for chosen combinations of parameter and study step values.

Lastly the computational algorithm used by the simulation is selected, which is called the solver. COMSOL has 2 types of solver, the first type being direct (MUMPS, PARDISO and SPOOLS) which are usually chosen by default by COMSOL and solve simulations in one large step, and the second type being iterative, which converge on a solution over a number of steps n. The relative error decreases as n increases, and when the error reaches a value below a defined relative tolerance, the iterative solver model is converged. Compared to direct solvers, iterative solvers require much less memory but depend highly on the system of equations being solved. The MUMPS direct solver was used predominantly in this thesis due to its efficiency in calculating solutions for the particular problems investigated.

3.3.1 Eigenfrequency Models for SAW Dispersions

An important technique used in this work was using COMSOL to calculate eigenfrequencies of unit cells, to investigate surface acoustic wave dispersions in phononic metamaterials patterned in lithium niobate ($LiNbO_3$), a piezoelectric material often used in SAW applications whose properties are discussed further in Chapter 4. The model setup was adapted from Ash et al. [39], who adapted it from a setup defined by Assouar et al. [51], and the geometry of a typical $LiNbO_3$ unit cell can be seen in Figure 3.5. The full geometry has three subdomains, labelled A, B and C. A is the active subdomain at the top which includes the phononic metamaterial pattern, B is the bulk subdomain and C is the bottom PML. The bulk domain B is much deeper than the active domain A so as to properly resolve SAW displacement modes at the surface.

To model the piezoelectric effect in the $LiNbO_3$, the 'Solid Mechanics' physics module with the 'Linear Elastic Material' material model was applied to the whole geometry, and was coupled to the 'Electrostatics' module by the 'Piezoelectric Effect' Multiphysics coupling, also over the whole geometry. The 'Free' and 'Fixed Constraint' boundary conditions were applied to the very top and very bottom boundaries respectively. The 'Fixed Constraint' was required to eliminate any in-plane displacement modes as displacement is forced to zero ($\mathbf{u} = 0$) at the bottom. Periodic Floquet boundary conditions were applied on the remaining opposite parallel boundaries to simulate an infinite square array. This was set up by defining $\mathbf{u}_{dst} = \mathbf{u}_{src} e^{-\mathbf{k_F} \cdot (\mathbf{r}_{dst} - \mathbf{r}_{src})}$ where $\mathbf{u}_{dst}$ and $\mathbf{u}_{src}$ are the displacements on the boundary condition destination and source faces, $\mathbf{r}_{dst}$ and $\mathbf{r}_{src}$ are the spatial coordinates at the boundaries and $\mathbf{k_F}$ is the wavevector (controlling this of the periodic boundary conditions allows the excitation wavevector being solved for by the simulation to be controlled).

Since in experiments 128°YX $LiNbO_3$ was used, this could be simulated by applying density, relative permittivity, elasticity matrix, piezoelectric coupling

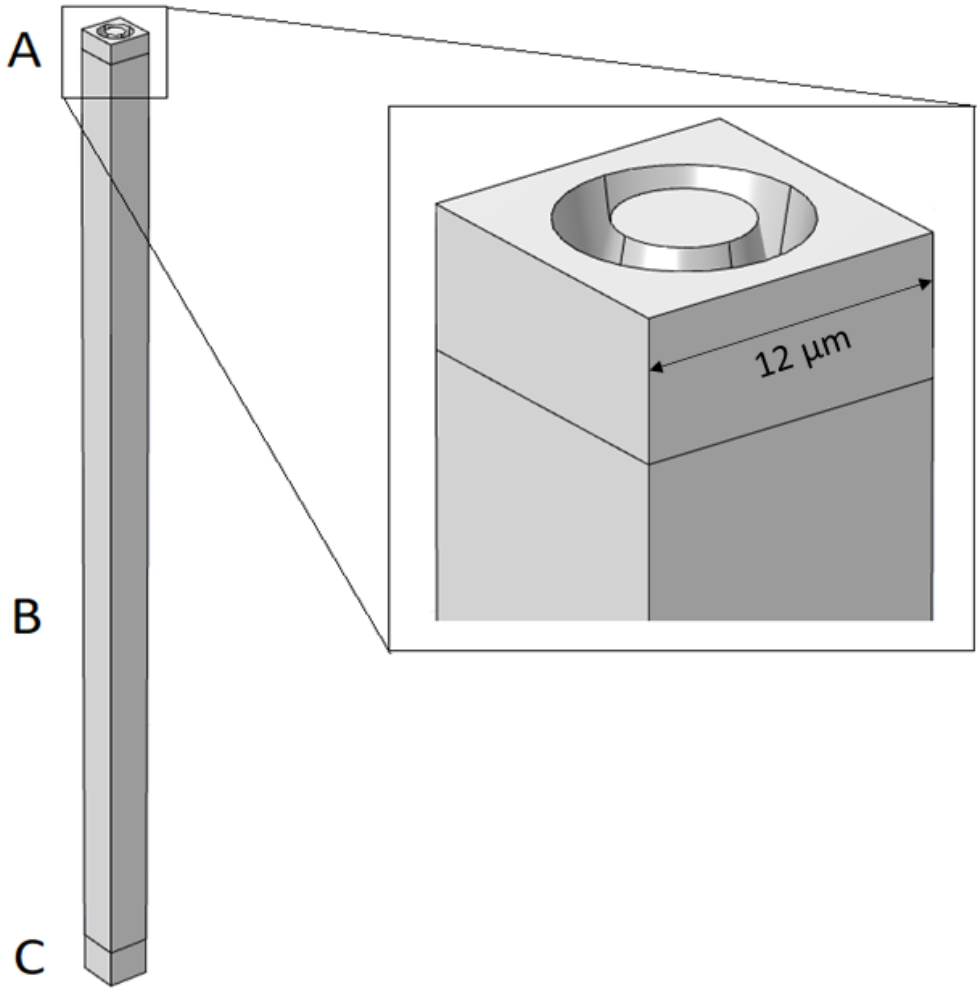

FIGURE 3.5: A schematic of a typical $LiNbO_3$ annular hole unit cell for calculating SAW dispersions. A is the top active subdomain which includes the phononic metamaterial structure, B is the bulk subdomain and C is the bottom PML.

matrix properties to the $LiNbO_3$ domain, and also a Euler transformation rotated coordinate system, which defines the material crystallographic axis. In this case the Euler transformation was (0, -0.663, 0).

In the active subdomain A a free tetrahedral mesh was used with a maximum element size in relation to the lattice constant $\frac{a}{8}$, and swept meshes were used in the bulk subdomain B and PML C with a maximum element size of $\frac{a}{2}$. The PML also had a 6 element distribution. A schematic of the mesh in a typical unit cell can be seen in Figure 3.6.

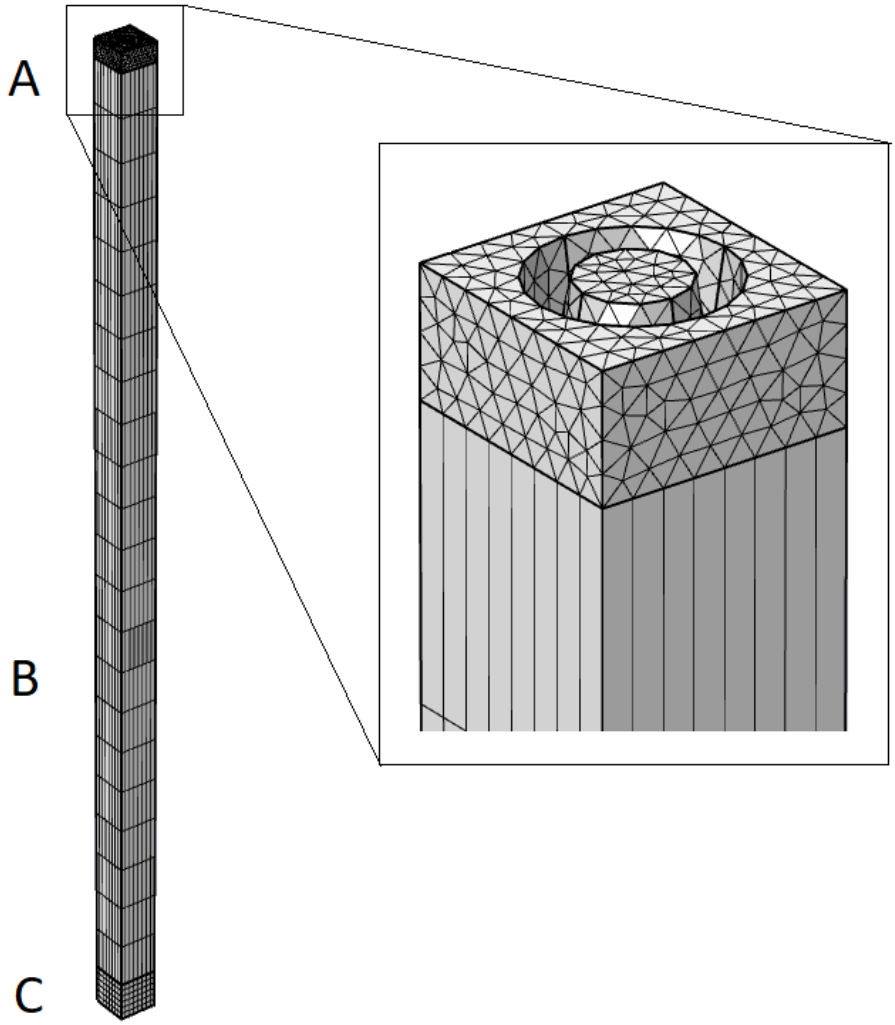

FIGURE 3.6: A schematic of the mesh in a typical unit cell. The active subdomain A has a free tetrahedral mesh, the bulk subdomain B and PML C have a swept mesh with maximum element size $\frac{a}{2}$, and the PML also has a 6 element distribution.

Bandstructures were found by running an eigenvalue study step on the unit cell, which solved for a specified number of frequencies (usually 10 in this thesis), searching for solutions around 0 Hz since the modes of interest were typically the lowest for each given wavevector. The study step performed a parametric sweep of the Floquet boundary condition $\mathbf{k}_F = k_x\hat{\mathbf{x}} + k_y\hat{\mathbf{y}} + k_z\hat{\mathbf{z}}$ within the first Brillouin zone defined by the geometry and reciprocal lattice vectors. The bandstructure could then be constructed by plotting the eigenfrequency solutions against wavevector.

SAW velocities for particular materials could also be calculated from the gradient of the lowest eigenfrequency found when the active subdomain A was blank (i.e. has no hole or pattern) and the entire model geometry was made up of that particular material.

3.3.2 Frequency Domain Models for SAW transmission

The transmission in phononic metamaterials with a finite array size could be investigated with a frequency domain study step at any frequency, as defined wavevectors were not required to drive excitation sources. This allowed the performance of the phononic metamaterial to be measured through quantities such as bandgap attenuation. Adapted from Ash et al. [39], a schematic of the typical geometry for a frequency domain transmission model can be seen in Figure 3.7, which shows a substrate of length L, width W and depth D surrounded by PMLs (coloured blue), and with a finite (4 elements) phononic metamaterial array and a SAW excitation source.

The setup was very similar to the eigenfrequency unit cell model (the same material models and physics modules, fixed constraint at the base, PMLs and piezoelectric multiphysics). The geometry width W corresponded to the lattice constant a, so the geometry could be modelled as infinite in the direction perpendicular to SAW propagation by applying Floquet periodic conditions on the long opposite faces. The frequency range investigated in this work was between 1-205 MHz, and following work by Ash et al. [39] a typical SAW frequency 140 MHz was defined, from which a typical wavelength λ was derived and used to inform the geometry dimensions. The depth D is 3λ and the length L is 15λ.

In order to generate SAWs, an edge load with an arbitrary amplitude of 1 N m^{-1} was applied the SAW source as labelled in Figure 3.7 in the direction of propagation. This negated the need to model interdigital transducers directly with a complicated scaling geometry and mesh, and additional electric potential

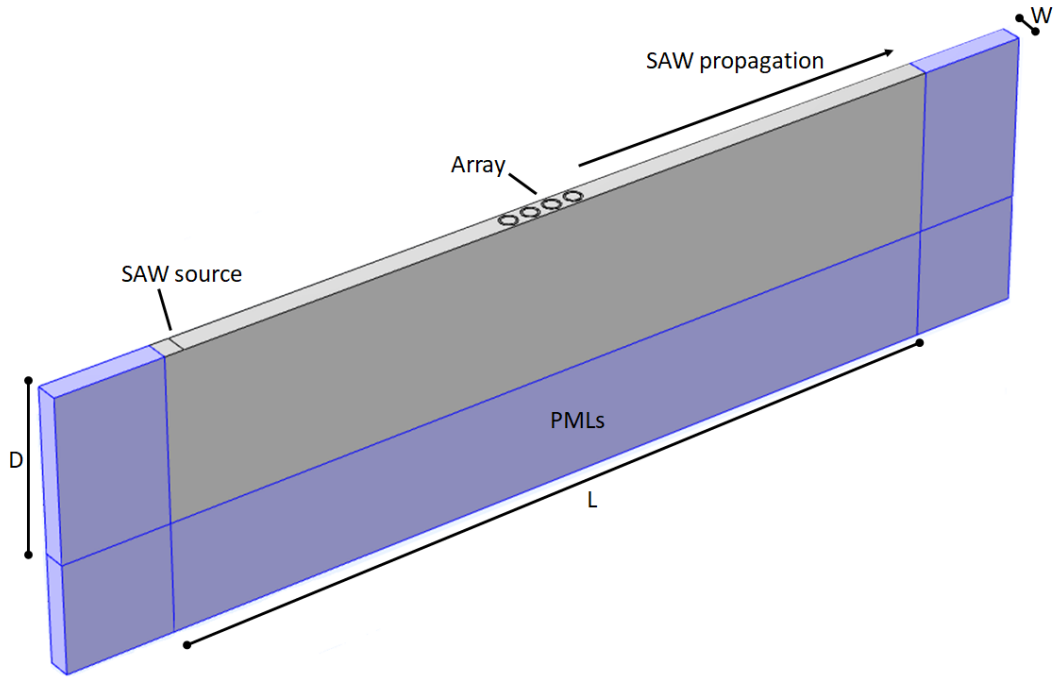

FIGURE 3.7: A schematic of the typical geometry for a frequency domain transmission model. A substrate of length L, width W and depth D is surrounded by PMLs (coloured blue) and patterned with a finite (4 elements) phononic metamaterial array, and the SAW excitation source can also be seen.

setup within the electrostatics module. The edge load could be excited at any frequency to simulate all required SAW frequencies.

A maximum mesh element size based on a maximum frequency of 205 MHz was chosen so as to resolve all SAW features properly at all frequencies. In the active domain (coloured grey in Figure 3.7), a free tetrahedral mesh was used, and in the PMLs a swept mesh with an element stretching distribution was used. An example of the full mesh can be seen in Figure 3.8.

Transmission could be investigated by comparing phononic metamaterial simulations to blank surface simulations. The average root-mean-square (RMS) SAW displacements were extracted from cut lines on the substrate surface on the opposite side of the SAW excitation source, after propagating through the phononic metamaterial array, and in the same location on the blank surface. The location and dimensions of the cut line can be seen plotted in red in Figure

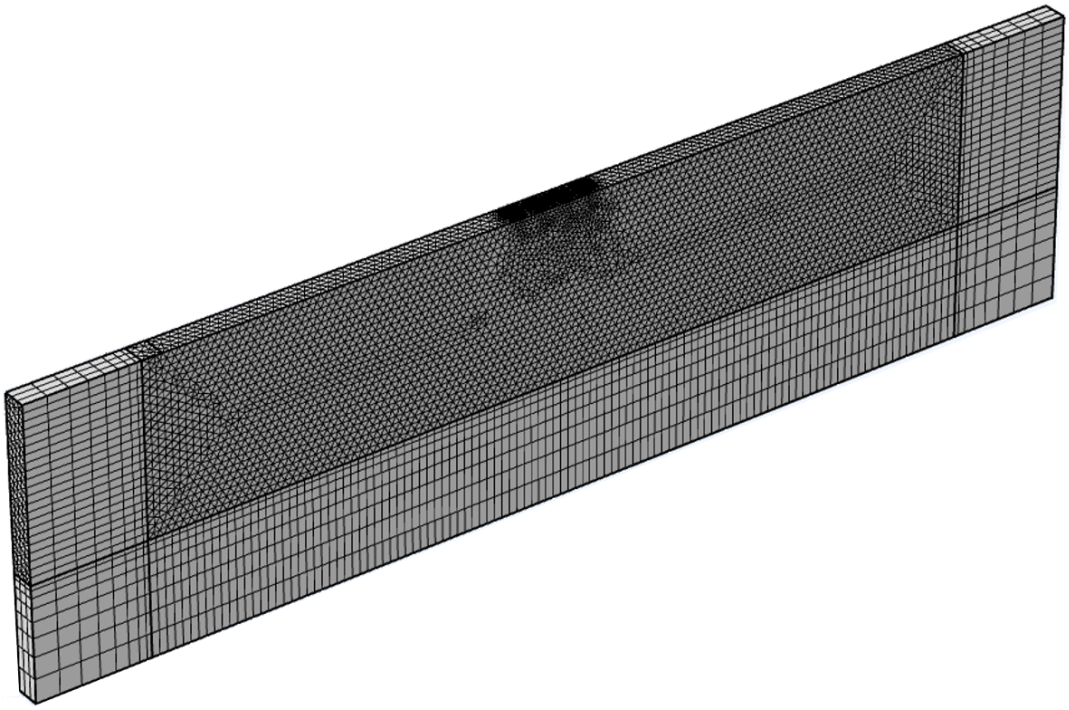

FIGURE 3.8: A schematic of the typical geometry mesh for a SAW transmission model, with a maximum element size based on a maximum frequency of 205 MHz.

3.9. The relative transmission spectrum could then be plotted by calculating the expression $T = 20\log_{10}\left(\frac{u_{ph}}{u_{blank}}\right)$ at each frequency, where u_{ph} and u_{blank} are the average RMS displacements for the phononic metamaterial and blank surface models respectively. Example displacement and transmission spectra are plotted in Figure 3.10.

Bandgap attenuation Γ could also be extracted by locating the bandgap frequency from the corresponding lowest RMS displacement value in the transmission step above, and calculating the in-plane displacement amplitude A at that value, and then calculating the expression $\Gamma = 20\log_{10}\left(\frac{A_{ph}}{A_{blank}}\right)$ at that frequency, where A_{ph} is the displacement amplitude for the phononic metamaterial and A_{blank} is the displacement amplitude for the blank surface. Further details on extracting this quantity can be found in Chapters 4, 5 and 7.

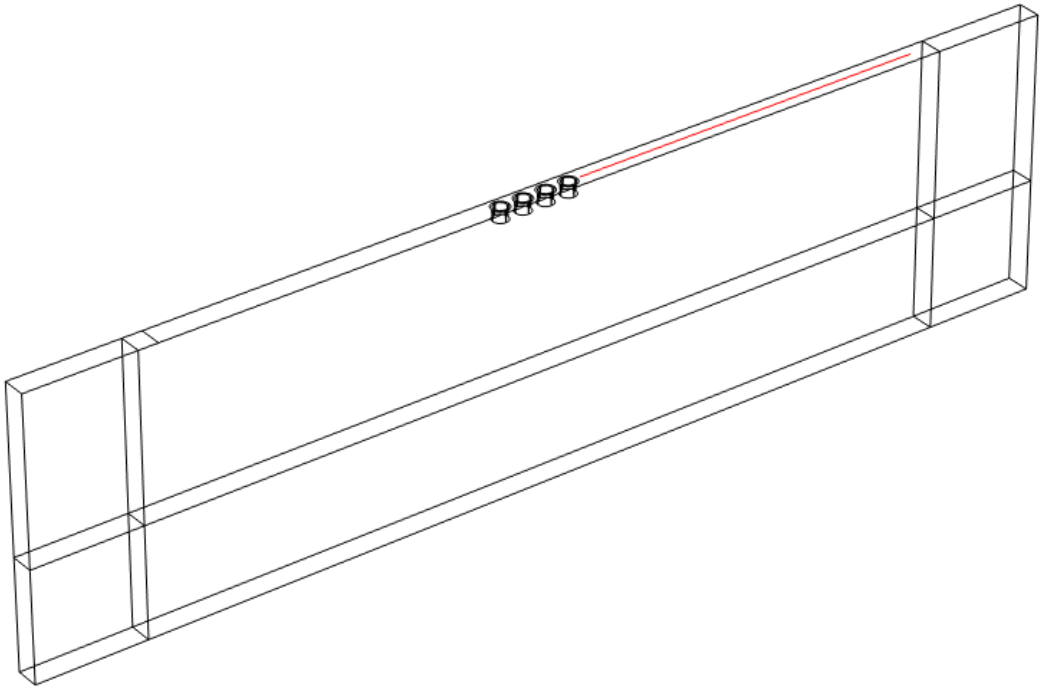

FIGURE 3.9: The location and dimensions of the cut line plotted in red on the surface of a typical phononic metamaterial model.

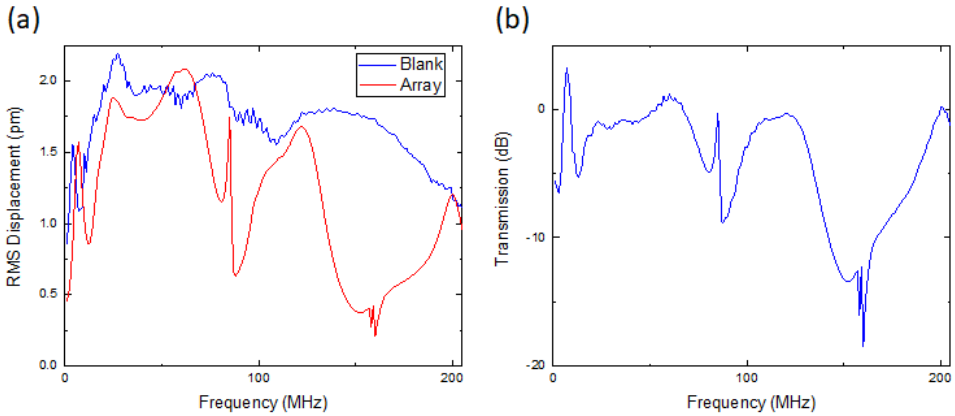

FIGURE 3.10: (a) Example RMS displacement plotted as a function of frequency for a blank surface and a phononic metamaterial and (b) the resulting transmission spectrum.

3.4 Summary

An outline of finite element modelling principles was presented in section 3.2, such as meshing and perfectly matched layers, followed by a discussion of the use of COMSOL Multiphysics to simulate SAW dispersions and propagation in

phononic metamaterials in section 3.3. A particular focus on using an eigenfrequency study step on unit cell models to calculate phononic bandstructures was presented in section 3.3.1, and the use of a frequency domain study to simulate SAW propagation and transmission in a finite phononic metamaterial was discussed in section 3.3.2 as these types of models form the basis of all the simulations undertaken in this thesis.

Chapter 4

Materials and Experimental Techniques

4.1 Overview

In this chapter, descriptions are presented of the materials and methods used to generate and detect surface acoustic waves in this thesis, and experimental techniques to fabricate and characterise SAW phononic metamaterial devices. In section 4.2 the crystallography of lithium niobate, a piezoelectric often used in SAW devices, is described, and in section 4.3 an explanation of how interdigital transducers can be used for SAW generation and detection. Descriptions of the experimental methods behind SAW device fabrication and characterisation can be found in section 4.4, such as focused ion beam etching, electrical characterisation with an oscilloscope system, and laser Doppler vibrometry.

4.2 Lithium Niobate

The behaviour of SAWs is highly dependent on the properties of the media on which they propagate, particularly for anisotropic piezoelectrics. The material from which devices were fabricated in this thesis was lithium niobate ($LiNbO_3$),

which is both highly anisotropic and highly piezoelectric and therefore efficient for SAW generation, but also widely commercially available.

$LiNbO_3$ is ferroelectric, and consists of planar oxygen sheets interspersed with atoms of lithium and niobium, as shown in Figure 4.1(a) [52]. There are several ways of defining the +c axis, such as the face normal to the axis becoming negatively charged when the structure is compressed. There is also 3-fold rotational symmetry about the c axis as seen in Figure 4.1(b) [52], and therefore $LiNbO_3$ has a hexagonal unit cell.

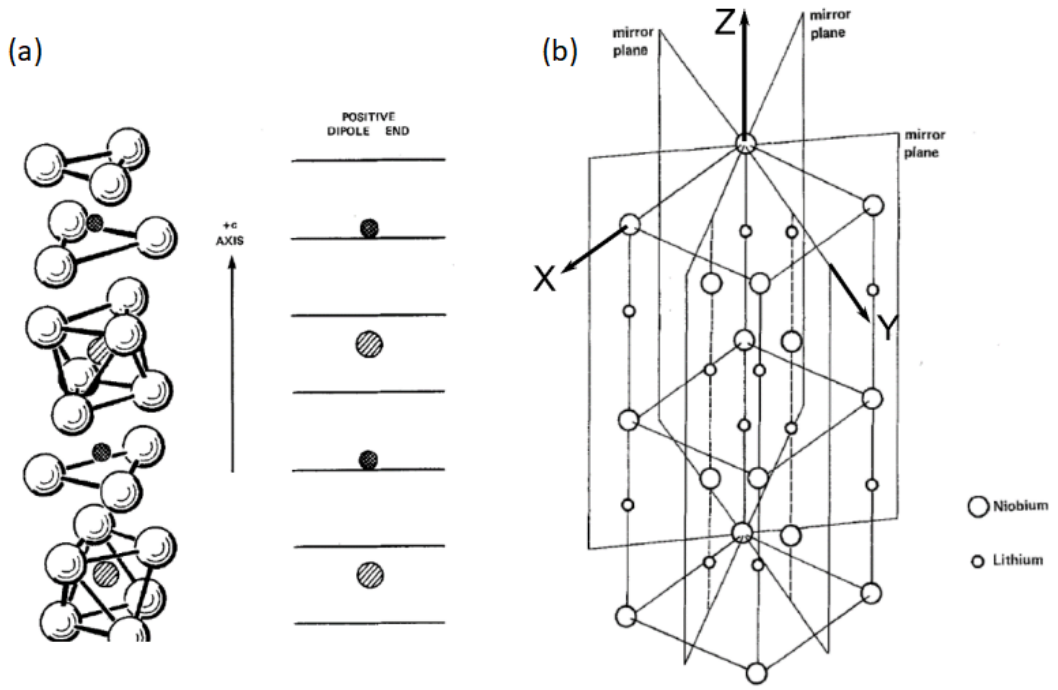

FIGURE 4.1: Taken from [52]. (a) A diagram of the crystal structure of $LiNbO_3$, where the lithium and niobium atoms are represented by shaded and cross-hatched circles respectively. (b) A diagram showing the hexagonal unit cell of $LiNbO_3$, with the rotational symmetry illustrated by mirror planes and highlighting of principle axes.

$LiNbO_3$ does not occur naturally and so when engineering it, standardised principle axes must be defined in order to maintain the crystal orientation consistently. The +Z axis is just taken to be the +c axis, while the X axis is perpendicular to the plane of symmetry and the Y axis is parallel to it. This forms right-handed Cartesian axes. Standard notation is used to define crystal cuts,

$(\theta - \vartheta)$, where θ is the surface normal and ϑ is the direction of propagation of the wave. SAWs in 128° YX $LiNbO_3$, which was used in this thesis, propagate in the X-direction while having a surface normal rotated clockwise about the +X axis of 128° from the +Y axis.

Crystal cuts can also be defined conveniently with Euler angles, such as in the case for 128° YX $LiNbO_3$ whose surface normal does not align with a crystal principle axis. Three angles α, β and γ define Euler angles and Euler transformed axes are (x, y, z) from the principle axes (X, Y, Z). Illustrated in Figure 4.2 [53], α is the angle between the x-axis and the axis defined by the line of nodes intersecting the planes defined by XY and xy (labelled N), β is the angle between the z-axis and the Z-axis, and γ is the angle between the N-axis and X-axis. The 128° YX $LiNbO_3$ cut can be achieved with a Euler angle transformation of (0, -38°, 0).

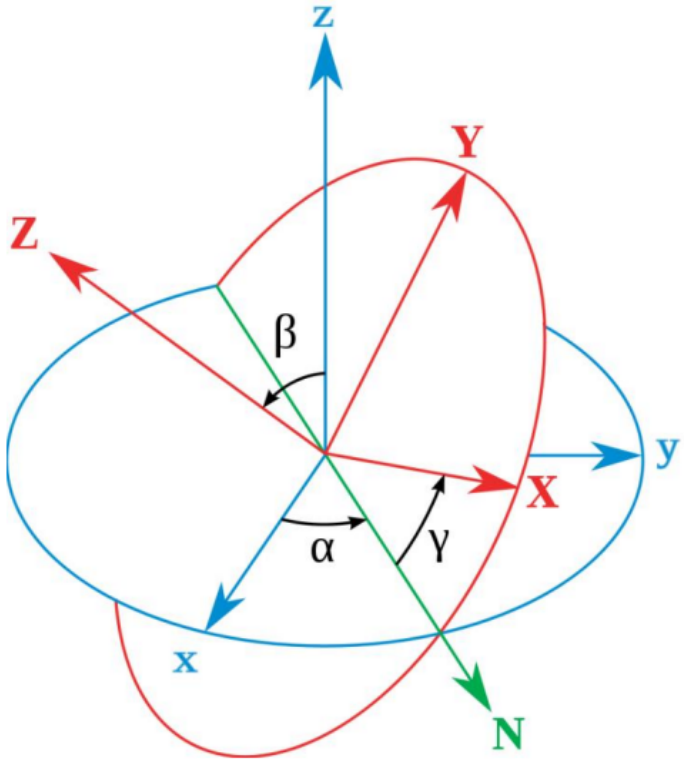

FIGURE 4.2: Taken from [53]. An illustration of the Euler angle transformation (α, β, γ) between the principle axes (X, Y, Z) and transformed axes (x, y, z), and the line of nodes N.

The orientation of the crystal cut and propagation direction is critical as seen in Figure 4.3 in which, for free and metallised cases, SAW velocity is plotted as a function of the direction of plate normal (in this case, $-\beta$, but labelled as μ) [54]. The SAW velocity changes markedly with the surface normal angle in both cases, and 128° YX $LiNbO_3$ with a free SAW velocity of around 3880 m s^{-1} is labelled on the plot.

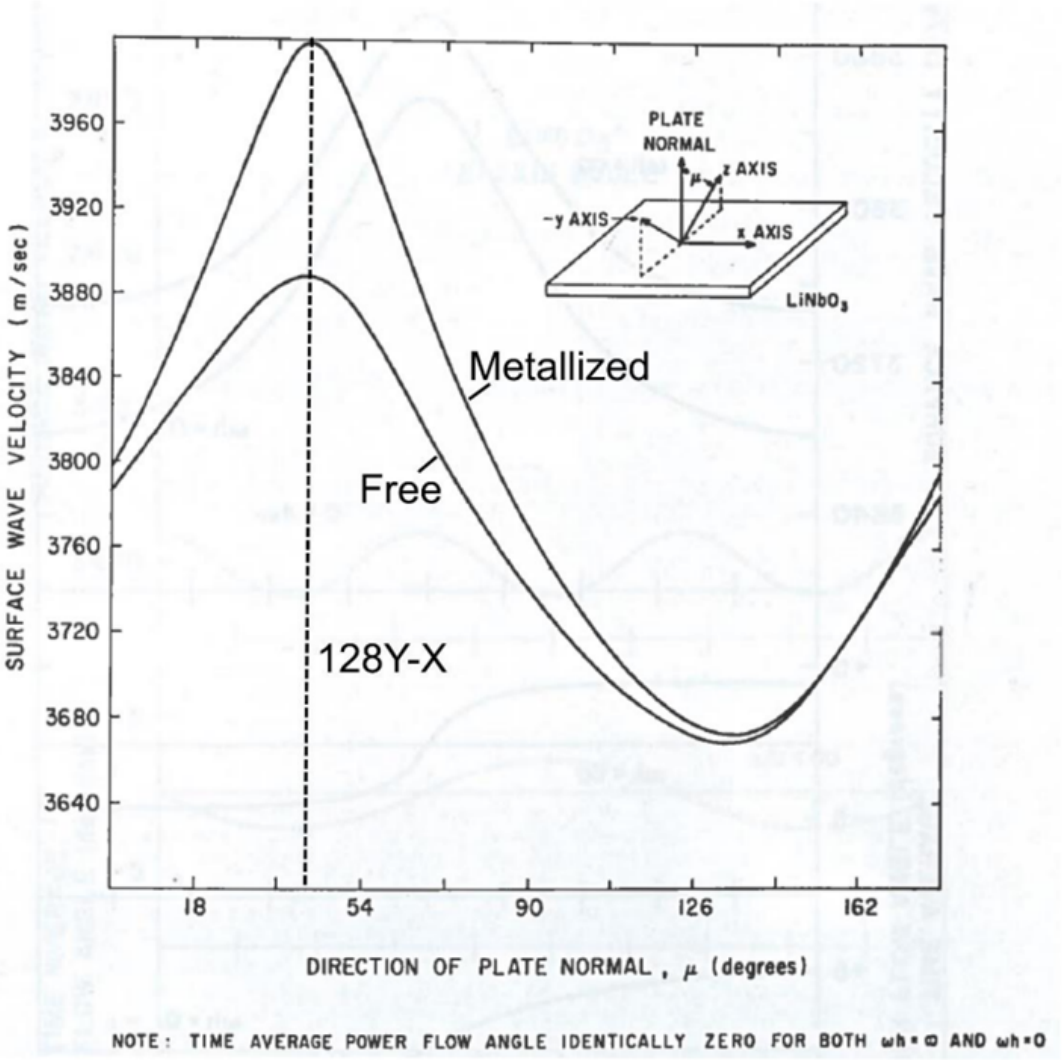

FIGURE 4.3: Taken from [54]. For the free and metallised cases, SAW velocity plotted as a function of the angle between the Z-axis and surface normal, with the direction of propagation in the direction of the X-axis.

SAWs are commonly generated on 128° YX $LiNbO_3$ through the use of interdigital transducers (IDTs).

4.3 Interdigital Transducers

For the SAWs generated experimentally in this work, interdigital transducers (IDTs) were used, which are comb-like structures of interlocking metal electrode fingers, patterned on the surface of piezoelectric materials such as $LiNbO_3$. An example schematic of an IDT can be seen in Figure 4.4. IDTs induce elastic stress in the material when a voltage is applied across them, and when the voltage is oscillated, SAWs are generated and propagate in both directions perpendicular to the electrodes' long axis. Peak amplitude SAWs are generated when the AC source frequency corresponds to the IDT periodicity, and the fundamental frequency f_0 is given by:

$$f_0 = \frac{v_{SAW}}{\lambda} \tag{4.1}$$

where v_{SAW} and λ are the SAW velocity and wavelength respectively. Higher frequency SAWs are also generated at higher order harmonic frequencies. In a reciprocal process, IDTs can also detect SAWs from an electrical signal generated by a corresponding elastic stress, so when two IDTs are opposed a SAW delay line (with one source IDT and one detection IDT) is formed. Typically in SAW delay lines, propagation distances and transducer apertures are on the order of millimetres, with IDTs of 20-1000 electrode fingers. IDTs can also have multiple interlocking electrode fingers rather than the single-digit scenario illustrated in Figure 4.4 [40]. For example the IDTs used for the experiments in this thesis were double-digit, to give multiple resonant frequencies.

The frequency response around the IDT fundamental frequency can be found by considering electrode fingers of uniform widths (a) and pitches (p) such that there is a metallisation ratio of 50% [40]. Assuming no diffraction or propagation losses occur and the IDT is non-reflective, the IDT has N electrode fingers centred at $x = x_1, x_2, ..., x_n$ etc and $x = 0$ is just outside the IDT, as illustrated

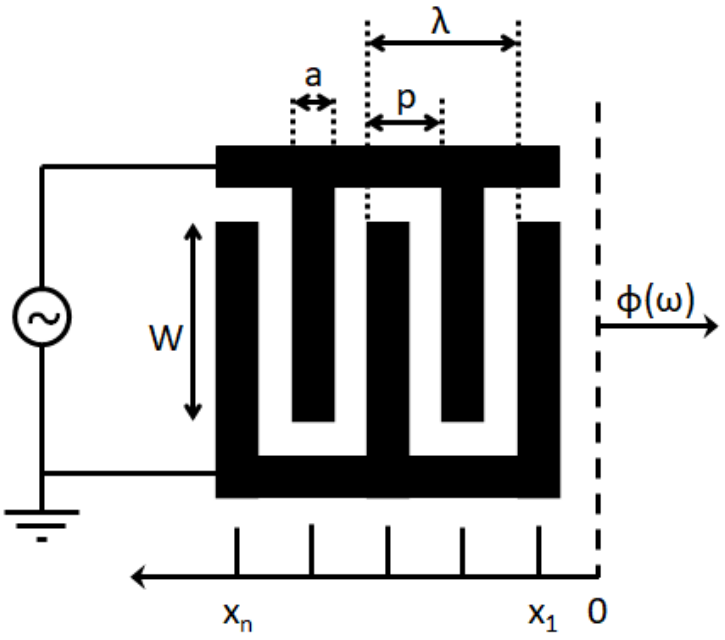

FIGURE 4.4: Adapted from [40]. A schematic of an IDT with n electrode fingers of width a, pitch p, aperture W and the fundamental SAW wavelength is labelled as λ.

in Figure 4.4. As discussed above, SAWs are generated in both x-directions when an AC voltage is applied, but in this case only the negative x-direction is considered as that is where a detecting IDT would be located. The flat horizontal domain at the top of Figure 4.4 is known as the 'live busbar', and this is where the voltage is applied to the electrode connected to it, while those attached to the bottom busbar are grounded. Each live electrode finger behaves as an individual SAW source and, assuming it is not affected by all the other electrodes, the amplitude of the SAW induced by the n^{th} electrode has the form $e^{ik(x-x_n)}$, where k is the wavenumber. A polarity $\hat{P}_n$, which distinguishes between grounded and live electrodes, is defined for each electrode n, so that for grounded electrodes $\hat{P}_n = 0$ and live electrodes $\hat{P}_n = 1$. This means that the SAW generated by the n^{th} electrode finger has an amplitude:

$$\phi_n(x,\omega) = VE(\omega)\hat{P}_n e^{ik(x-x_n)}e^{i\omega t} \tag{4.2}$$

where ω is the frequency, V is the applied voltage and $E(\omega)$ is the element factor, representing the individual electrodes' responses which allows for physical process. The SAW amplitude at $x = 0$ can be written as a linear summation of the contribution from each IDT electrode finger:

$$\phi_n(\omega) = \sum_{n=1}^{N} \phi_n(0,\omega) = VE(\omega)e^{i\omega t} \sum_{n=1}^{N} \hat{P}_n e^{-ikx_n} \tag{4.3}$$

This expression will hold for any polarity sequences $\hat{P}_n$, for example 'single-digit' IDTs ($\hat{P}_n = 0, 1, 0, 1, ...$) or 'double-digit' IDTs ($\hat{P}_n = 0, 0, 1, 1, 0, 0, 1, 1, ...$) as used experimentally in this thesis.

Excluding V and $E(\omega)$ allows the frequency response to be represented conveniently by an array factor $A(\omega)$:

$$A(\omega) = \sum_{n=1}^{N} \hat{P}_n e^{-ikx_n} \tag{4.4}$$

For single-digit IDTs $A(\omega)$ can be written as a sum of M_p terms which have a spacing of $\Delta x = 2p$ and electrode centres at $x_n = np$, and where the number of periods in the IDT is $M_p = N/2$:

$$A(\omega) = \sum_{m=1}^{M_p} e^{-2ikp} \tag{4.5}$$

When this summation is treated as a geometric progression it can be rewritten as:

$$A(\omega) = \frac{\sin(M_p kp)}{\sin(\theta kp)} e^{-i(M_p+1)kp} \tag{4.6}$$

This expression for $A(\omega)$ is plotted (in arbitrary units) close to f_0 in Figure 4.5 [55]. Amplitude peaks occur at $kp = n\pi$ in Equation 4.6, which can be rewritten as $2p = n\lambda$. This means the fundamental frequency response occurs at $n = 1$ and for higher values of n, higher harmonics are exhibited. Similar behaviour is displayed by double-digit IDTs.

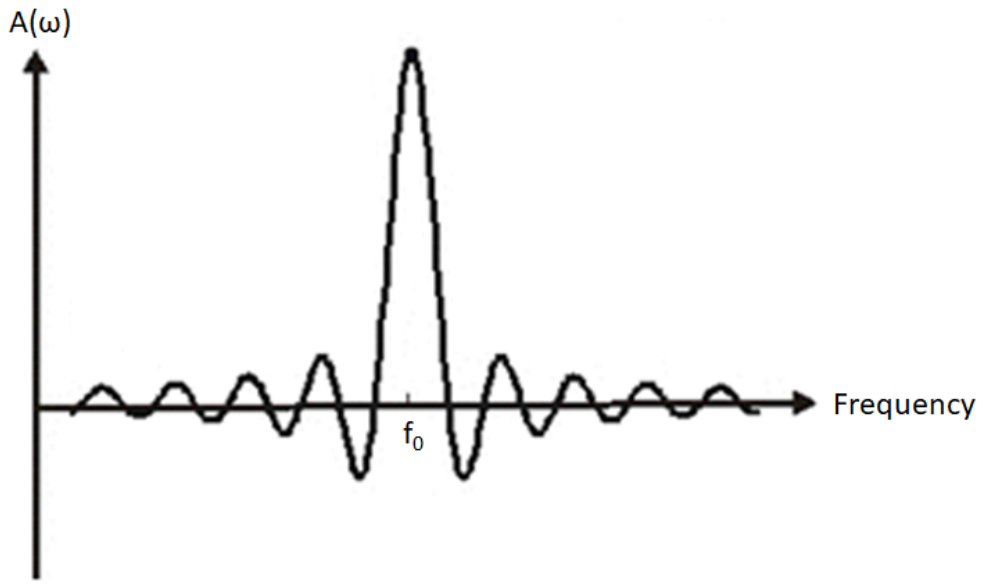

FIGURE 4.5: Adapted from [55]. Array factor $A(\omega)$ plotted (in arbitrary units) in the region of the fundamental frequency f_0 of a uniform single-digit IDT.

IDT frequency responses can also be manipulated through a process known as apodisation, where electrode lengths are varied with respect to the transducer aperture W, but all the transducers used in this thesis have constant electrode finger lengths.

4.4 Metamaterial Fabrication and Experimental Methods

The steps of the overall fabrication process of the metamaterial array are illustrated in Figure 4.6.

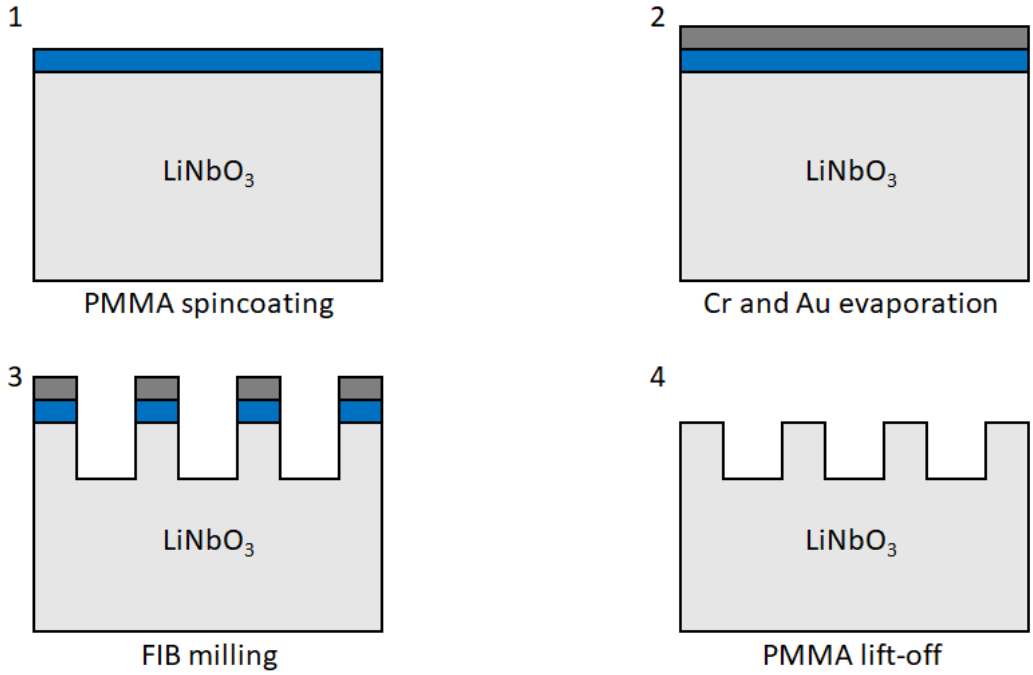

FIGURE 4.6: The four overall steps of the fabrication process for a typical SAW device used in this thesis.

4.4.1 Device Preparation

Diamond-shaped 128° YX-cut $LiNbO_3$ substrates from MESL Microwave/COM DEV International with 2 opposing pre-patterned aluminium interdigital transducers (IDTs) with 8 double-digit fingers, a centre-to-centre IDT separation of 5.4 mm and aperture of 3.25 mm were used. The substrates required a number of steps in order to be prepared for focused ion beam (FIB) etching. They were first washed with acetone, then rinsed with isopropanol and dried. A resistive 400 nm layer of 950K A6 PMMA was then spin-coated onto the surface at 4000 rpm, followed by a 2 thermally evaporated layers, 5 nm of Cr and 95 nm of Au. Since pattern etching took place in a combined FIB-SEM (focused ion beam-scanning electron microscope) system, this conductive metal layer was necessary to avoid a build-up of charge on the substrate surface which can disrupt the FIB beam, and the samples were grounded to stubs with carbon tape as shown in Figure 4.7(a).

4.4.2 Focused Ion Beam Etching

The prepared substrates were then placed in a FEI Nova 600 dual-beam FIB-SEM system as shown in Figure 4.7(b). The FIB component used a gallium ion column, with a range of 5 - 30 kV of accelerating voltage and a range of 1 pA - 20 nA of probe current, giving a resolution of 5 nm. The SEM component had a range of 200 V - 30 kV of accelerating voltage, and a probe current of up to 20 nA, giving a resolution of 1.0 nm at 30 kV. Imaging was performed by a secondary electron detector.

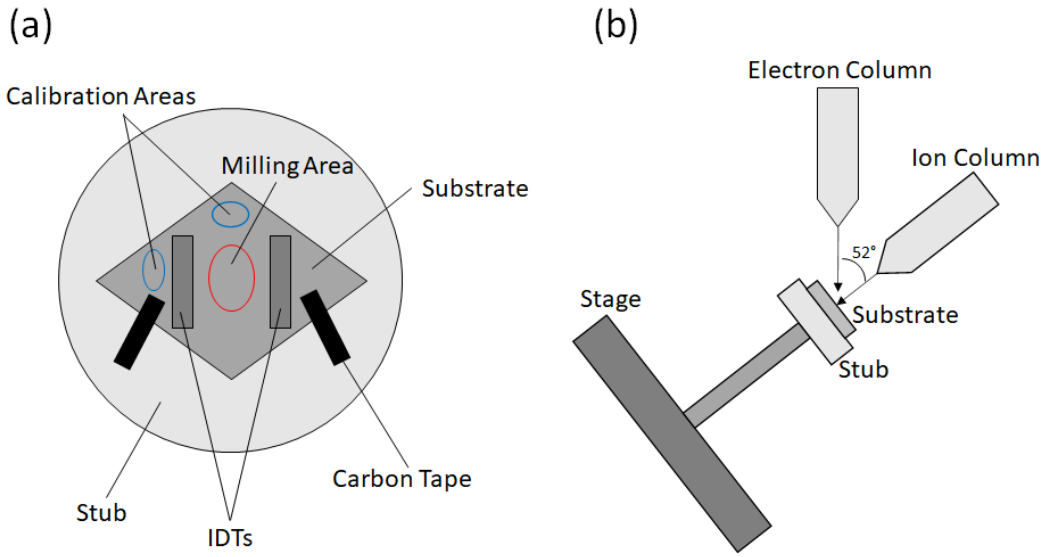

FIGURE 4.7: A schematic of the SAW device substrate, ready for milling in the FIB-SEM system. (a) The substrate mounted on a stub and grounded with carbon tape, ready for calibration holes to be milled within the blue areas, and for the metamaterial array to be milled within the red area between the IDTs. (b) The substrate on the stub mounted at the eucentric height between the electron and ion beam columns.

The substrate surface was moved to be normal to the ion beam path, which is 52° from the vertical, and adjusted so that the electron and ion beams are both incident at the same point on the device surface, known as the eucentric height. Both beams were focused and the stigmation adjusted, and the equipment was pumped down over several hours to achieve a vacuum for improved milling conditions.

Before each milling session, a series of calibration annular holes of constant radii (inner and outer radii of 3.5 and 4.5 µm respectively) had to be milled with different FIB doses (combinations of specified depth and beam current) in order to consistently mill the correct hole dimensions. This took place in the areas of the device outside the SAW apertures as indicated by the blue circles in Figure 4.7(a). The resulting true depths of the calibration holes were measured by SEM using a cross-section. Platinum was deposited with a gas injection system of $C_9H_{16}Pt$, in which the gas adsorbed to the substrate surface, and its chemical bonds were broken when exposed to the secondary electrons from the lower current FIB. The Pt was deposited over a section of each hole for imaging contrast, then a stepping cross-section trench was milled and the depth measured. This process can be seen in Figure 4.8, and two example calibration holes with Pt can be seen in Figure 4.9(right).

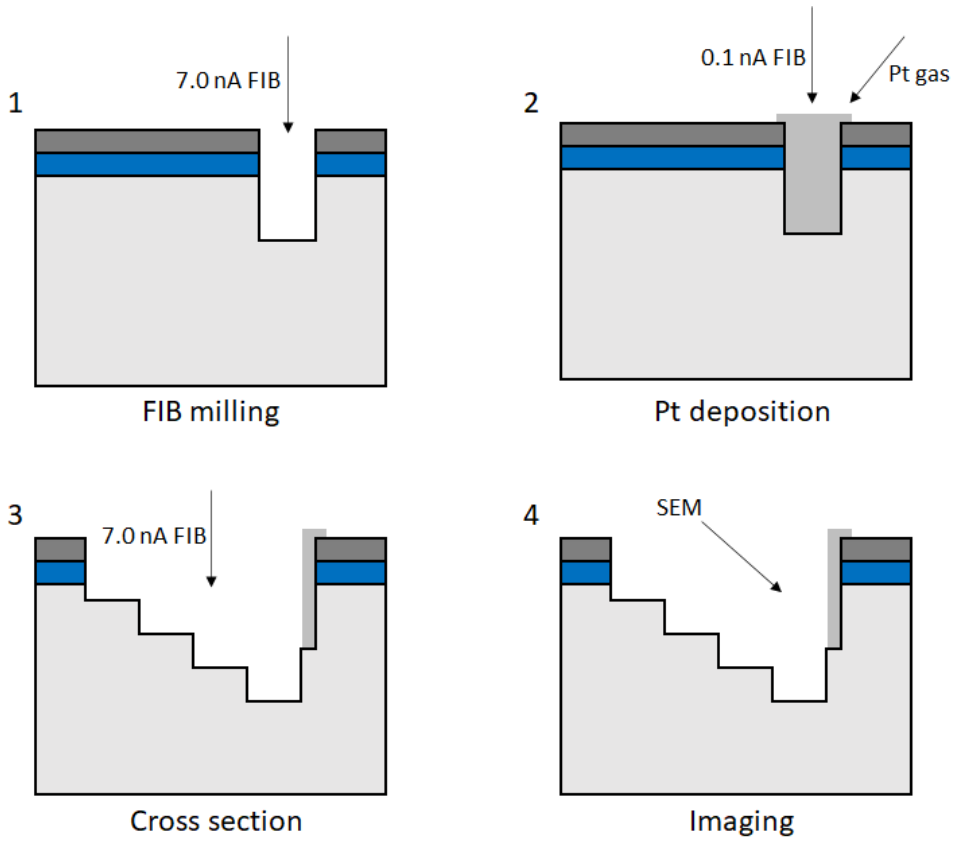

FIGURE 4.8: A demonstration of the depth calibration process using platinum deposition and cross-sectioning.

When the measured depth of the calibration holes and FIB dose converged on the correct depth, a square array of four annular holes 6 µm deep, with inner and outer radii of 3.5 and 4.5 µm respectively, and a pitch of 12 µm could be milled within the red circled area in Figure 4.7, over a series of milling sessions. With a 7.0 nA FIB current, milling could only take place over an area of 220 x 250 µm (the size of the FIB aperture at the particular magnification and beam current) at one time before having to move the stage, resulting in manual array stitching between each section of the array and thus some minor defects in the final device. The final array covered the entire transducer aperture (approximately 250 rows of 4 elements), a small section of which can be seen in Figure 4.9(left).

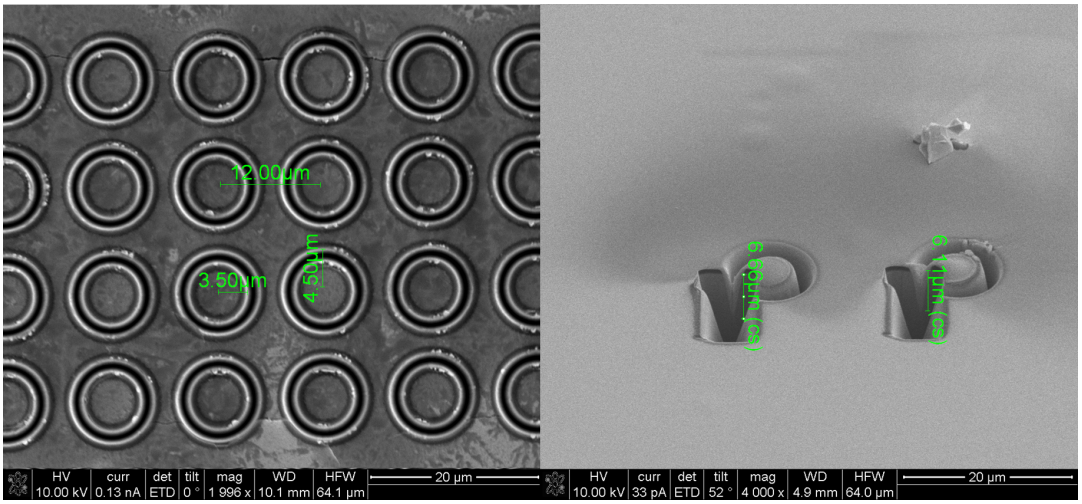

FIGURE 4.9: (left) SEM image of a section of the fabricated array in $LiNbO_3$, (right) iterative cross-section procedure converging on 6 µm depth, with Pt deposited for contrast.

4.4.3 Sample Mounting

After etching, the substrates were placed in acetone for lift-off of the PMMA/metal layer, and fixed with conductive silver paint on copper printed circuit boards (PCBs) with SMA connectors soldered onto the end of the signal tracks. Bonds of gold wire between the IDT bonding pads and the PCB were created with a Kulick and Soffa 4123 Wedge Bonder, which ultrasonically vibrated thin gold wire threaded through a silicon carbide wedge to melt it onto the copper PCB

surface. These bonds allowed voltage to be applied across the device through the SMA connectors at the bottom of the signal tracks, and hence SAWs to be launched and detected. A photo of a SAW device mounted on and bonded to the PCB, ready for characterisation, can be seen in Figure 4.10.

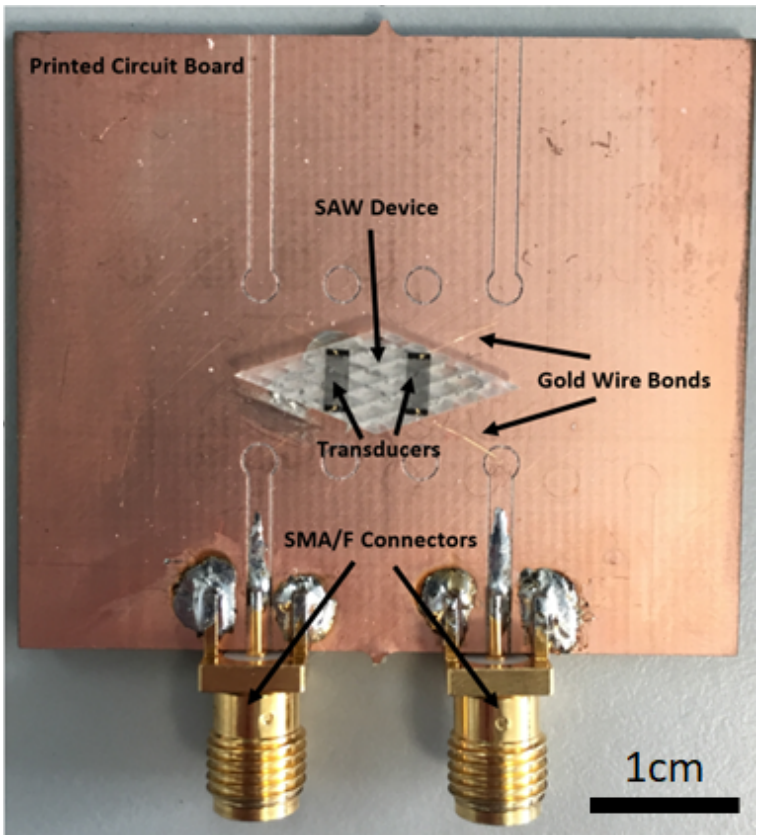

FIGURE 4.10: A photo of the SAW device mounted on and bonded to the copper PCB with gold bonding wires and SMA connectors.

4.5 Experimental Techniques and Characterisation

Characterisation of devices was undertaken at room temperature in air at atmospheric pressure, then in a vacuum chamber. The vacuum chamber was flushed three times with nitrogen to remove any water vapour condensation on the device surface before vacuum measurements are made, since this could artificially increase mass loading effects.

4.5.1 Oscilloscope System

An oscilloscope system was used to investigate the SAW transmission through the metamaterial device, by measuring the amplitude of the electric signal from the receiving transducer. A schematic of the system setup can be seen in Figure 4.11. RF signal up to 205 MHz was pulsed through the device through the source IDT using an Agilent 8648C RF signal generator for the source and a Kiethley 3390 arbitrary waveform generator for the pulse, at frequencies at which the SAWs have the largest amplitudes (the first 6 IDT resonant frequencies, 11, 33, 97, 119, 183 and 205 MHz), and SAW waveforms detected at the receiving IDT were analysed for amplitude and other wave characteristics with a LeCroyWaveRunner 204Xi-A digital oscilloscope.

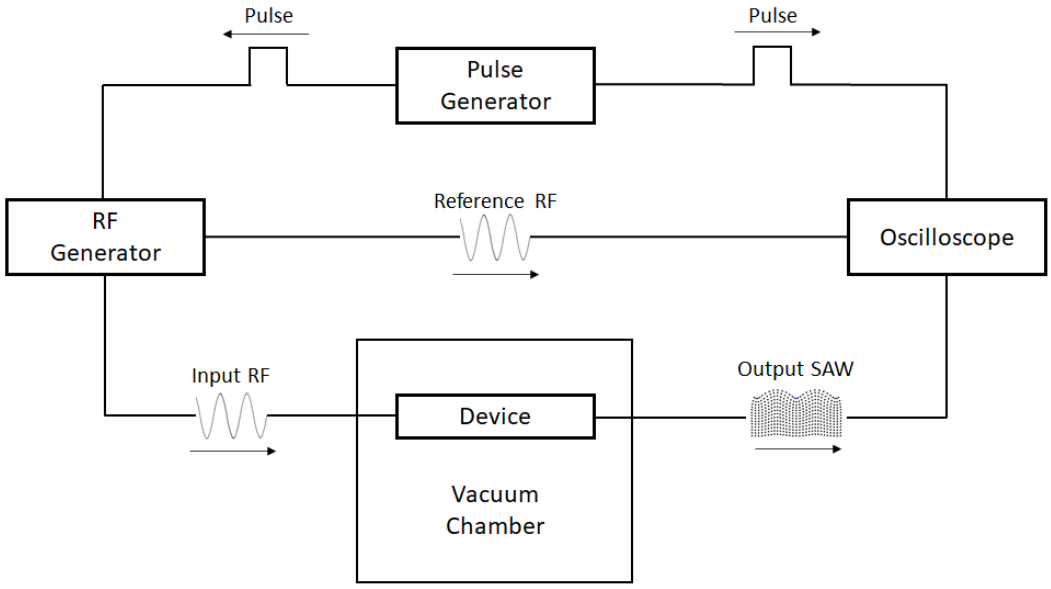

FIGURE 4.11: A schematic of the oscilloscope measurement system.

A typical SAW measurement as seen on the oscilloscope is shown in Figure 4.12 where the yellow waveform in Channel 1 (C1) is the pulse signal, the red waveform in Channel 2 (C2) is the input reference signal, the first blue waveform in Channel 3 (C3) is the output signal from the SAW device and the second blue waveform in Z3 is a zoomed section of C3. Z3 waveforms were subsequently

exported and analysed. The amplitudes of the output signals have an envelope due to the frequency response of the transducers as shown in Figure 4.5.

FIGURE 4.12: A screenshot from a typical SAW measurement taken by the oscilloscope system. Channel 1 (C1) is the pulse signal, Channel 2 (C2) is the input reference signal, Channel 3 (C3) is the output signal from the SAW device and Z3 is a zoomed section of C3.

4.5.2 Data Reduction and Analysis

A segment a few wavelengths in length was the chosen from the widest part of the waveform saved from the oscilloscope, as the waveform was contained in an envelope. An example of this can be seen in Figure 4.13. A sine wave was fitted to this segment using a SciPy curve_fit function where the frequency was known, and the amplitude was extracted from the resulting fitting report, from which attenuation coefficients (discussed in Chapter 6) could then be calculated.

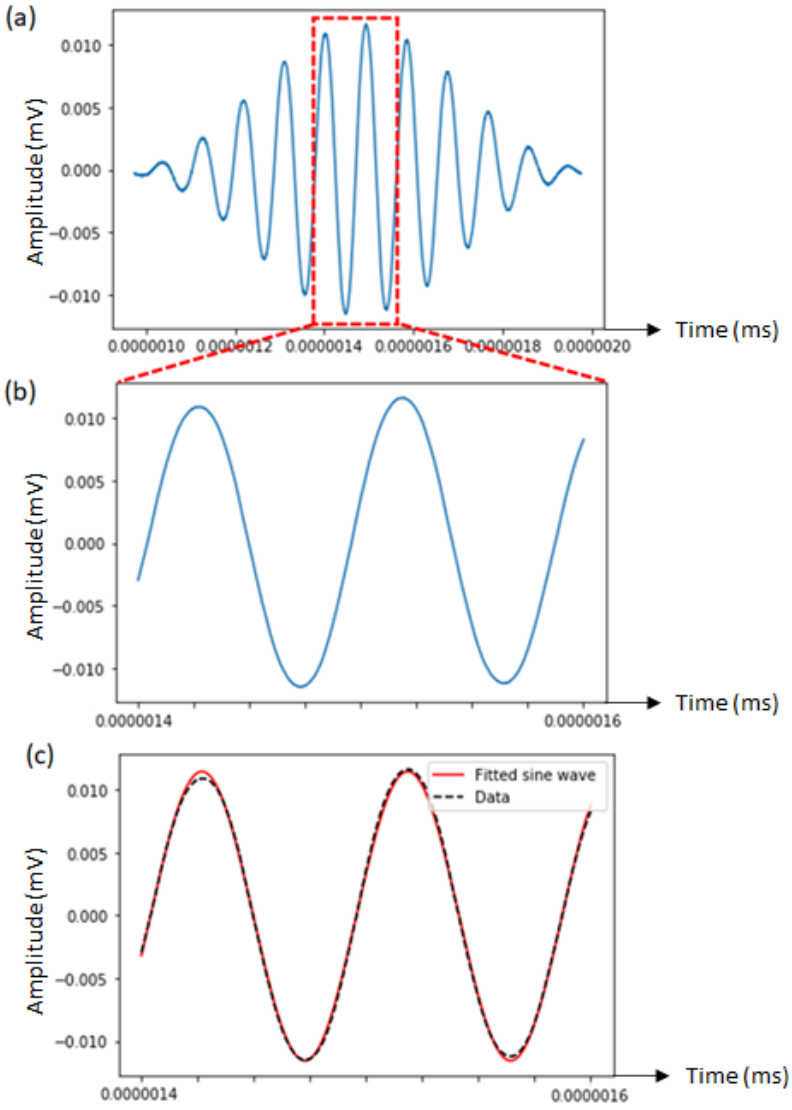

FIGURE 4.13: (a) an example oscilloscope waveform (11 MHz) plotted in Python, where the red dashed box represents the chosen segment at the widest part of the envelope, (b) the chosen segment, (c) the chosen segment with fitted sine wave.

4.6 Laser Doppler Vibrometry

Imaging and direct measurements of the SAWs themselves were also possible thanks to laser Doppler vibrometry (LDV), which is a technique able to quantify vibrations on the surface of materials through measurements of lasers which are reflected from surfaces on which SAWs propagate. LDV specifically measures the Doppler shift f_d induced by the velocity of the out-of-plane displacement generated by the SAW, given by:

$$f_d = \frac{2v(t)}{\lambda}\cos(\theta) \tag{4.7}$$

where $v(t)$ is the displacement velocity, λ is the wavelength of the incident laser and θ is the angle between the velocity vector and incident laser [56]. Shifting the frequency of the incident laser (for example with a Bragg cell) can induce a carrier frequency f_c, and a photodetector can detect the beat frequency between the two paths ($f_c + f_d$). By demodulating the beat frequency (usually on the order of tens of MHz), the out-of-plane displacement can be measured. A schematic of a typical LDV system can be seen in Figure 4.14.

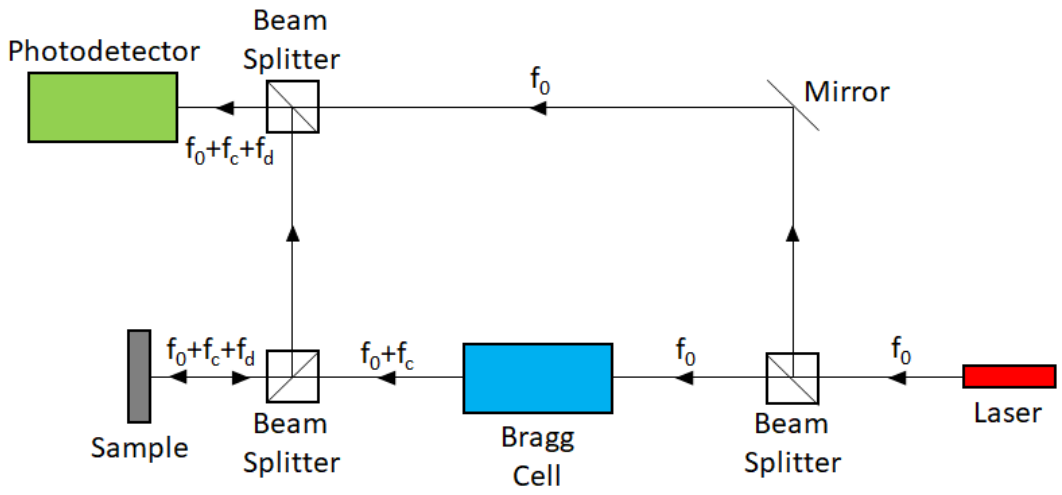

FIGURE 4.14: A schematic of a typical laser Doppler vibrometer system.

In the same way as for the oscilloscope system, measurements also took place under vacuum and atmospheric pressure conditions. For both pressure conditions, the device was housed in a Linkam stage, carefully positioned on the LDV stage. Using a Polytec UHF-120 lase Doppler vibrometer with a 50 magnification objective, frequency domain scans of the device surface were performed for each SAW frequency, which were generated by the LDV system itself with continuous wave RF signals to the source IDT. A 500 nm wavelength laser scanned the patterned scanned a section of the array and its immediate surroundings in a grid pattern, and averages of maximum amplitudes at three grid points

in the region just before the SAW encountered the array and three grid points just after the SAW encountered the array were taken, by manually finding the maximum by cycling through frames of the animation generated by the LDV. A screenshot of the LDV data gathering process can be seen at an example SAW frequency of 33 MHz in Figure 4.15. LDV data required no subsequent curve fitting, and attenuation coefficients were again calculated from the SAW amplitudes, as discussed in Chapter 6.

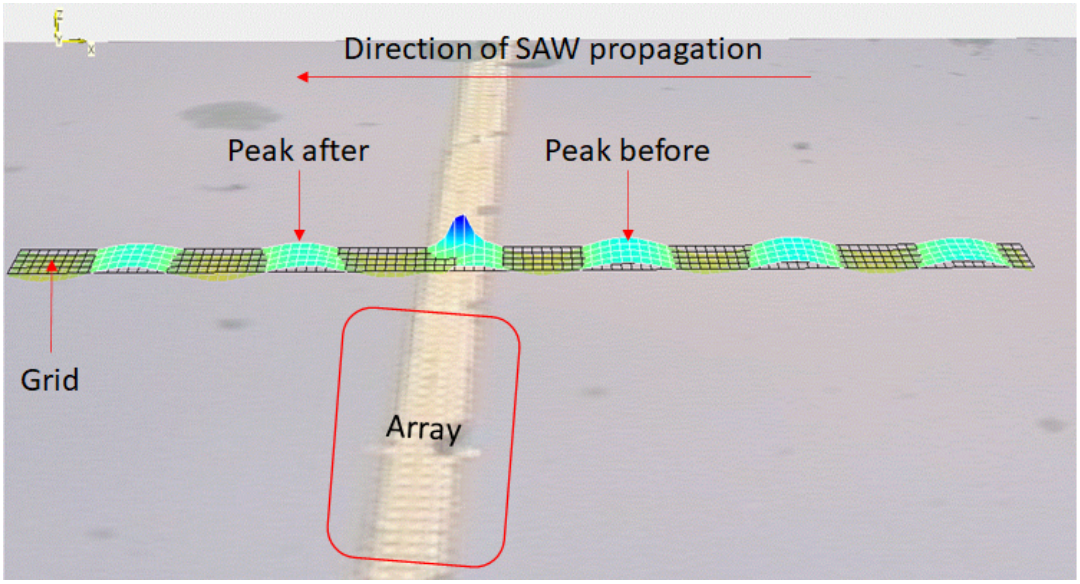

FIGURE 4.15: A screenshot of the LDV data gathering process at a SAW frequency of 33 MHz. The yellow-coloured circular pattern is the metamaterial array, and the peak SAW amplitudes on the grid can be seen in turquoise. The peaks from which the maximum amplitudes were extracted are labelled.

4.7 Summary

The crystallography of lithium niobate, a piezoelectric often used in SAW devices, was described in section 4.2, and in section 4.3 an explanation of how interdigital transducers (IDTs) can be used for SAW generation and detection was presented. The experimental methods behind the fabrication and characterisation of the particular SAW device patterned with a square array of annular

holes used in this thesis, such as focused ion beam etching, electrical characterisation with an oscilloscope system, and laser Doppler vibrometry, were described in section 4.4.

Chapter 5

Tuning Surface Acoustic Wave Bandstructures in Phononic Crystals and Local Resonator Arrays

5.1 Overview

As discussed in Chapter 2 SAWs can be controlled and manipulated in a number of ways, including the use of phononic crystals (PnCs) but more recently, periodic local resonator arrays, which have also attracted attention as their bandstructures are affected by the characteristics of the individual resonating elements as well as the geometry. This allows for greater freedom of design compared to conventional PnCs.

New SAW devices with better performance and functionality compared to existing devices can potentially be realised by exploiting the properties of PnCs and local resonator arrays. For example, tunable filters for radar and communications applications could be created if bandgaps can be dynamically tuned. Phononic metamaterials, including both PnCs and local resonator arrays, can

also be engineered for sensing applications, since SAW propagation is affected by the presence of external stimuli. An improved understanding of the behaviour of PnCs and local resonator arrays in the presence of additional materials (other than the substrate and air) is needed if such novel devices are to be realised.

However, a full analytical analysis of the effect of introducing additional materials on the properties of phononic metamaterials is not straightforward for a number of reasons. Firstly, as discussed in Chapter 2 there are no analytical solutions to the surface acoustic wave equation, for example due to an unbounded surface in the vertical direction and piezoelectric coupling in very anisotropic substrates. These factors apply to just the single substrate material, meaning that any interactions with additional inclusion material introduce a further layer of complexity.

In this chapter, a computational study is therefore presented of the effects of filling both cylindrical and annular holes in lithium niobate substrates, representing conventional phononic crystals and local resonator arrays respectively, with different materials. Using finite element modelling, bandstructure analyses are performed on the filled cylindrical and annular holes as well as a study of the bandgap attenuation, with aims to identify the best candidates for bandgap tuning (through a relationship between bandgap features and material characteristics) and sensing respectively by comparing the results of the FEM study with a simple analytical model.

5.2 Geometry

Two types of surface patterning on a lithium niobate substrate were investigated. The first geometry was a square array of cylindrical holes, which forms a conventional phononic crystal, in which the holes were 6 µm deep, with a top radius of 4.5 µm, and where the lattice constant of the array was 12 µm. The

holes were slightly conical, to reflect what can be fabricated in practice, with a bottom radius of 3.5 µm.

The second geometry was a square array of annular holes, which forms an array of local resonators, shares these dimensions but also possesses an inner radius of 2.5 µm. Schematics of the 3D geometry of both hole types can be seen in Figure 5.1. In the analytical model a single unit cell was considered, and top down views of the top of both types of holes can be seen in Figure 5.2. The darker grey domains in Figure 5.2 can be filled with material, which introduces scattering across and between unit cells.

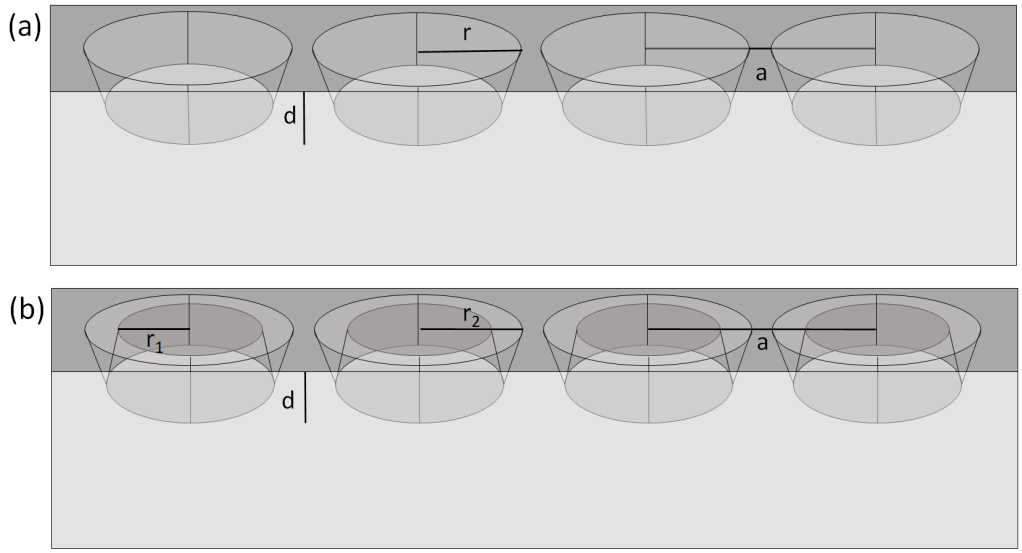

FIGURE 5.1: Schematic diagrams (not to scale) of 4 adjacent unit cells of (a) the cylindrical hole geometry, where the depth d is 6 µm, the top radius r is 4.5 µm and the lattice constant a is 12 µm, and (b) the annular hole geometry, where the depth d is 6 µm, the top inner radius r_1 is 2.5 µm, the top outer radius r_2 is 4.5 µm and the lattice constant a is 12 µm. The darkest shade of grey represents the top of the substrate, the middle shade represents the hole edges and bottom surfaces, and the lightest shade represents the side boundaries, made transparent for easier visualisation of the holes. In practice, this is where periodicity conditions are applied in the simulation.

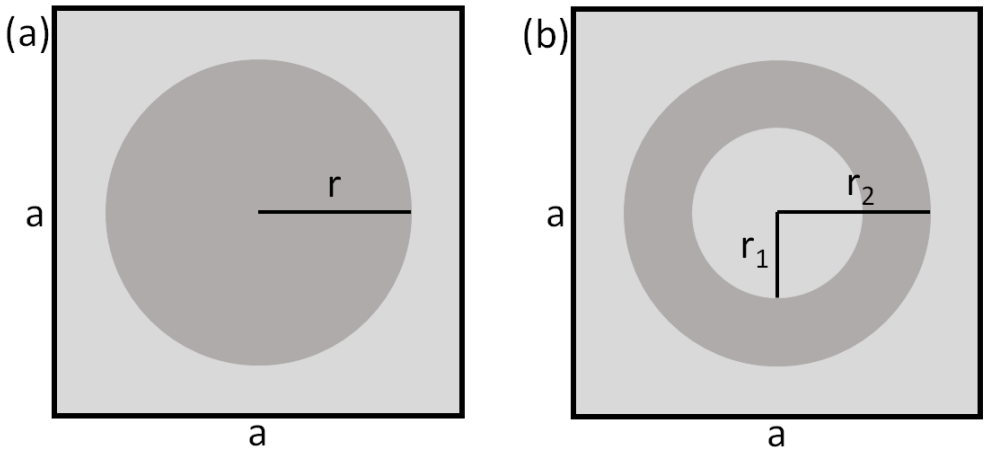

FIGURE 5.2: To scale, at the top of the hole/lithium niobate surface. The lighter grey domains represent the lithium niobate substrate, while the darker grey domain represents the hole. Top down schematics of an individual unit cell of (a) the cylindrical hole geometry, where the depth d is 6 µm, the top radius r is 4.5 µm and the pitch/lattice constant a is 12 µm, and (b) the annular hole geometry, where the depth d is 6 µm, the top inner radius r_1 is 2.5 µm, the top outer radius r_2 is 4.5 µm and the pitch/lattice constant a is 12 µm.

5.3 Analytical Modelling

Two different regimes of scattering were considered - Mie scattering (occurring within the unit cell), and Bragg scattering (occurring between adjacent unit cells) [17]. The fundamental resonance frequency due to Bragg scattering along the $\Gamma - X$ path is given by:

$$f_{Bragg} = \frac{V_{avg}}{2a} \tag{5.1}$$

where a is the period of the array, and the average SAW velocity, V_{avg}, is given by:

$$V_{avg} = \pi \left(\frac{r}{a}\right)^2 V_i + \left(1 - \pi \left(\frac{r}{a}\right)^2\right) V_M \tag{5.2}$$

for cylindrical holes, where V_i is the SAW velocity of the material within the holes, V_M is the SAW velocity within the surrounding lithium niobate (approx.

3980 m s^{-1}), r is the radius of the holes and a is the lattice constant. For annular holes, the average velocity is modified to:

$$V_{avg} = \left(\frac{\pi r_2^2 - \pi r_1^2}{a^2}\right) V_i + \left(1 - \frac{\pi r_2^2 - \pi r_1^2}{a^2}\right) V_M \tag{5.3}$$

where r_1 is the inner radius and r_2 is the outer radius, and all other terms remain the same.

The fundamental frequency for Mie scattering in cylindrical holes is given by:

$$f_{Mie} = \frac{V_i}{4r} \tag{5.4}$$

where all terms are defined as above. The fundamental radial mode (across the ring) in annular holes occurs when $\lambda/2$ equals the width of the ring, and since $V_i = f_{Mie}\lambda_i$, the fundamental frequency is modified to:

$$f_{Mie} = \frac{V_i}{2(r_2 - r_1)} \tag{5.5}$$

where, again, r_1 is the inner radius and r_2 is the outer radius.

5.4 Finite Element Modelling

5.4.1 Bandstructures

Bandstructures were obtained from a COMSOL Multiphysics eigenfrequency study (following work by Ash et al. [39]) on a lithium niobate ($LiNbO_3$) resonator supercell, which is equivalent to one unit cell of Figure 5.1, and can be seen in Figure 5.3. Floquet periodicity conditions were applied on opposite parallel sides to simulate an infinite square array, and a perfectly matched

layer (PML) was applied at the bottom boundary to absorb any bulk wave excitation without reflection. The bandgap centre was calculated from the first (lowest frequency) clear bandgap between 2 eigenfrequencies, the frequency values of which were extracted at the Brillouin zone edge X (wavenumber $k = 0.5$ in units of π/a), as indicated by the circles in Figure 5.4.

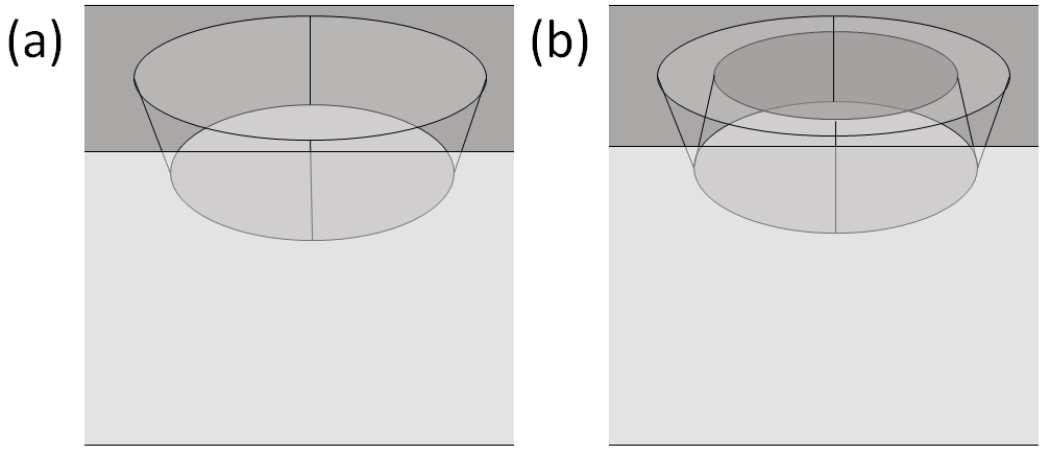

FIGURE 5.3: Schematics of the individual resonator supercell of (a) cylindrical holes and (b) annular holes.

Indicative bandstructures across the first irreducible Brillouin zone ($\Gamma - X - M - \Gamma$) for empty holes can be seen in Figure 5.4. Only the $\Gamma - X$ bandstructure was investigated in this chapter, since Figure 5.4 shows the first clear bandgap extending across the whole Brillouin zone for both types of hole. Simulating full bandstructures for all scenarios is computationally expensive, so choosing just the $\Gamma - X$ path is justified as it is a good representation of the whole Brillouin zone. The same is also true when the holes are filled with material, and indicative full bandstructures are shown in Figure 5.5.

When the holes (the darker grey domains in Figure 5.2) were empty, bandgaps were observed at X with central frequencies of 141.2 MHz and 119.0 MHz for the cylindrical and annular holes respectively, consistent with the findings of Ash et al. and Kyrimi et al. [39] [57].

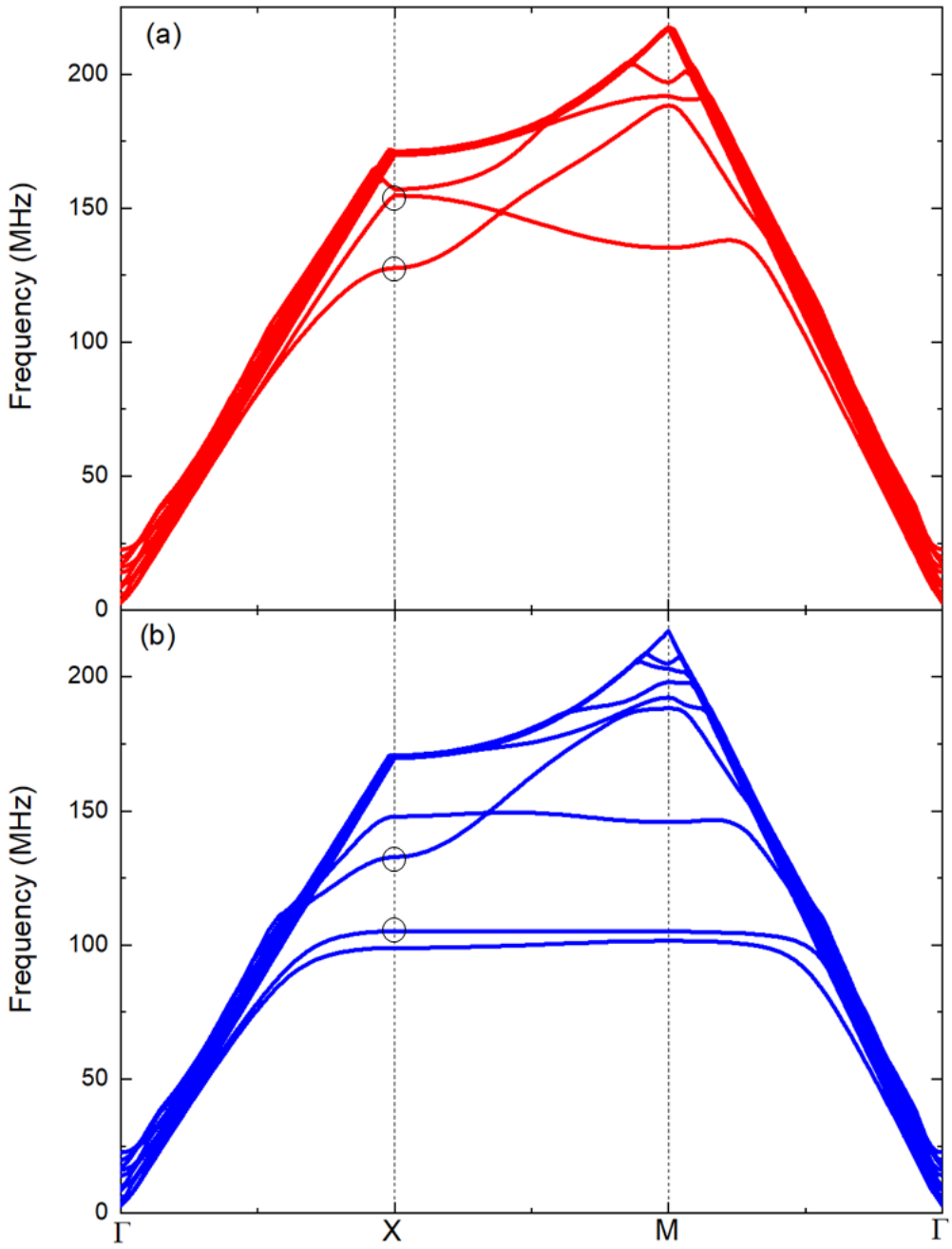

FIGURE 5.4: Bandstructures for the first irreducible Brillouin zone for (a) empty cylindrical holes and (b) empty annular holes. With the exception of a band touching point between X and M for the cylindrical holes, the first clear bandgap extends across the whole Brillouin zone, justifying the choice of extracting the bandgap characteristics at X as a representation of the full Brillouin zone. The circles represent the eigenfrequencies chosen for the first clear bandgap, the frequencies of which were extracted.

The holes were then filled with different materials. In COMSOL, materials not pre-defined in the material library can be created with combinations of

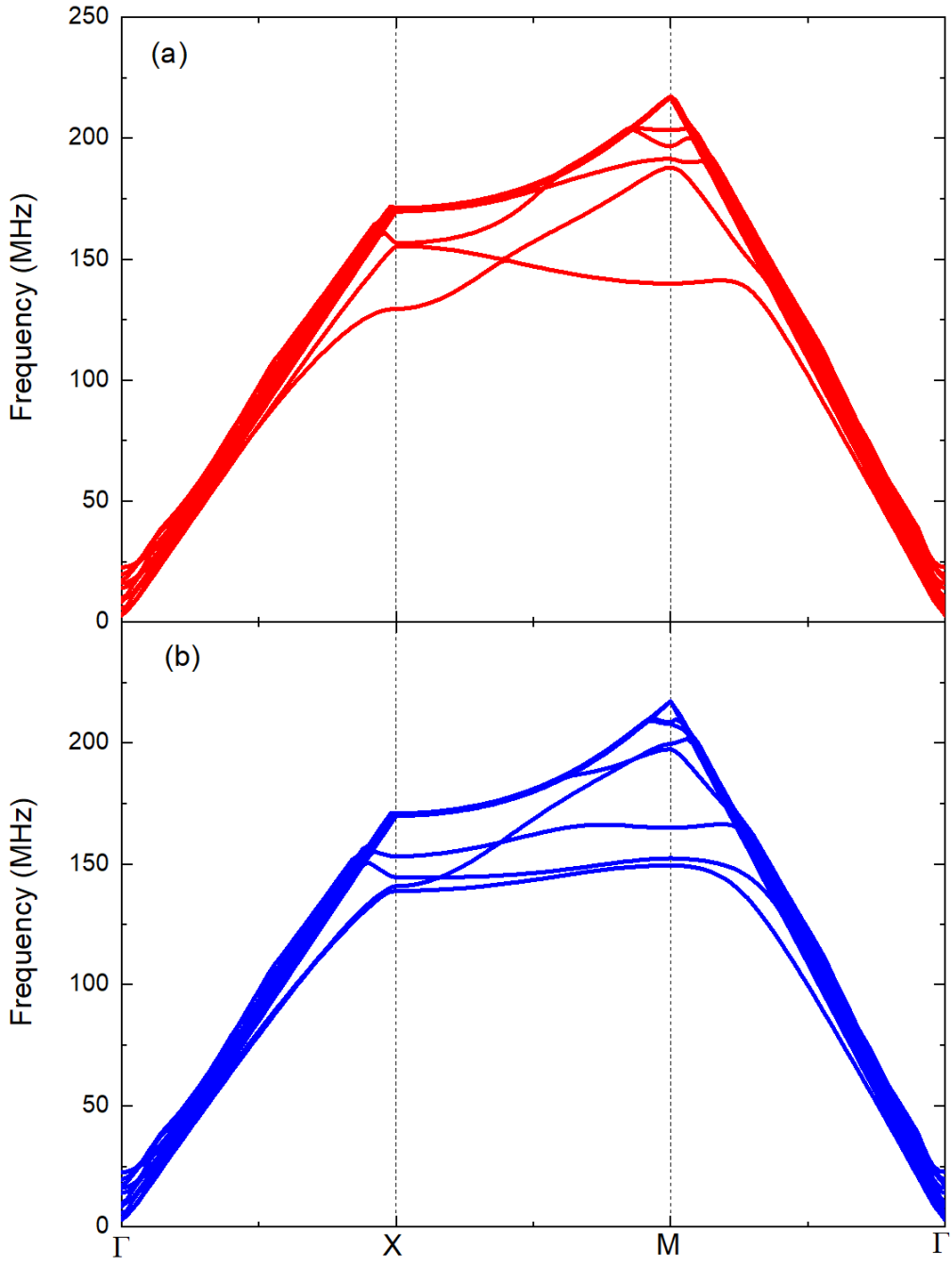

FIGURE 5.5: Bandstructures for the first irreducible Brillouin zone for (a) cylindrical holes and (b) annular holes, both filled with Material 30 from Table 5.1.

user-chosen parameters, the default combination being Young Modulus (YM), density and Poisson Ratio. In this chapter, 50 different combinations of YM and density were used (resulting in different SAW velocities), a summary of which can be seen in Table 5.1. All the materials defined had a Poisson Ratio

of 0.3, which is a value similar to or shared by many common materials. For example, glass, stainless steel and PMMA all have Poisson Ratios within ± 0.02 of 0.3.

SAW velocities for each material were found by performing an eigenfrequency study (as above) on a supercell of a solid block comprised of the material (rather than of lithium niobate) with no surface patterning, and calculating the gradient of the first eigenfrequency. Materials missing a corresponding SAW velocity in Table 5.1 (such as Material 14) did not produce bandgaps when either type of hole was filled with those materials.

In Figure 5.6 the calculated central bandgap frequency extracted from the simulated bandstructure is plotted as a function of the SAW velocity of the filling material, V_i, for cylindrical ((a) solid red symbols) and annular ((b) open blue symbols) holes. Values of the bandgap frequency calculated using Equations 5.1 - 5.4 are also plotted in Figure 5.6, and show that the data follow 2 distinct regimes, aligning at lower V_i with Mie scattering, and at higher V_i with Bragg scattering. Modes (displacement magnitude) were also extracted from bandgap limits at the Brillouin zone boundary, which give an indication of the appearance of Mie and Bragg resonance. Examples of these resonances can be seen in Figure 5.7.

At lower V_i for the cylindrical holes, at the bandgap limits, the displacement is concentrated towards the centre of the hole inclusion, and modes here are described by circular Mie modes, in particular the 2nd order resonance mode (in Equation 5.4 the fundamental mode corresponds to $\lambda = r$, so for the 2nd order mode, $\lambda = 2r$), so two dark red antinodes are seen in Figure 5.7(a) rather than one. At higher V_i, more Bragg-like modes are observed, with the highest displacement occurring symmetrically at the edges of the unit cell, as in Figure 5.7(c). In the overlapping V_i region, combinations of mode shapes can be seen. For the annular holes at lower V_i the bandgap centre is determined by resonance

TABLE 5.1: A summary of the 50 different combinations of Young Modulus and density, and the resulting SAW velocities.

Material ID	**Young Modulus (GPa)**	**Density (kg m^{-3})**	**SAW Velocity (m s^{-1})**
Material 1	100	1000	5721
Material 2	50	1000	4045
Material 3	1	1000	572
Material 4	0.5	1000	404
Material 5	0.1	1000	180
Material 6	100	500	8090
Material 7	100	100	18091
Material 8	100	50	25585
Material 9	100	1	180914
Material 10	100	0.5	255851
Material 11	1	500	809
Material 12	0.1	500	255
Material 13	0.01	500	80
Material 14	0.01	1000	
Material 15	0.05	1000	127
Material 16	0.05	500	180
Material 17	10	1000	1809
Material 18	10	500	2558
Material 19	0.5	1000	404
Material 20	0.5	500	0.01
Material 21	100	2000	4045
Material 22	50	2000	2860
Material 23	100	3000	3303
Material 24	50	3000	
Material 25	100	4000	
Material 26	50	4000	
Material 27	150	2000	
Material 28	150	3000	
Material 29	150	4000	
Material 30	5	500	1809
Material 31	2	1000	809
Material 32	3	1000	990
Material 33	2.5	1000	904
Material 34	2	500	1144
Material 35	3	500	1144
Material 36	2.5	500	1279
Material 37	1.5	500	990
Material 38	2	1000	809
Material 39	1.5	1000	700
Material 40	1	2000	404
Material 41	1.5	2000	495
Material 42	2	2000	572
Material 43	2.5	2000	639
Material 44	5	2000	904
Material 45	1	3000	330
Material 46	1.5	3000	404
Material 47	2	3000	467
Material 48	0.5	3000	233
Material 49	0.5	4000	202
Material 50	1	4000	286

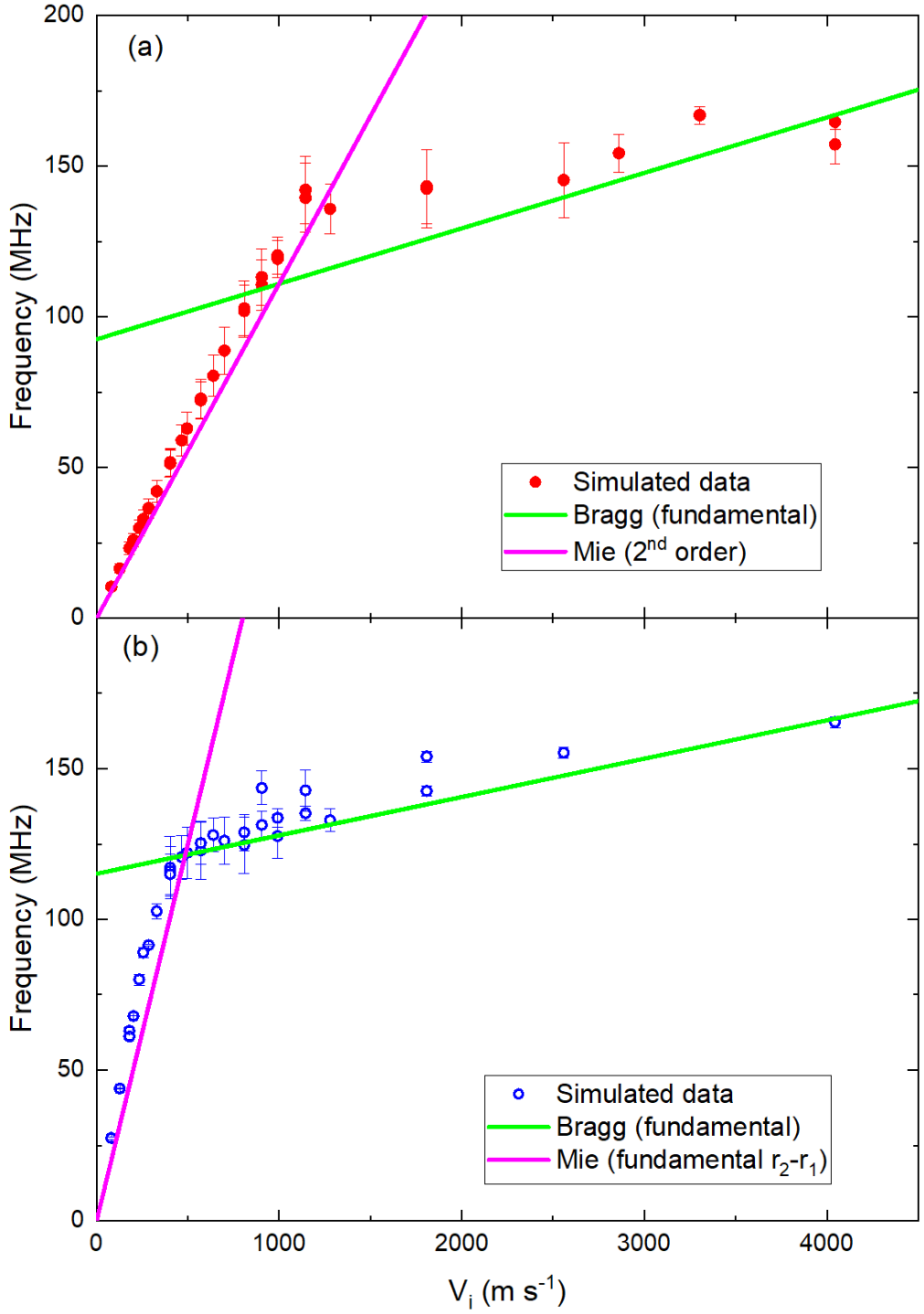

FIGURE 5.6: Central bandgap frequencies as a function of filling material SAW velocity V_i for (a) cylindrical holes and (b) annular holes, where the uncertainty bars represent the upper and lower bandgap limits. The magenta line in both subfigures represents the relevant Mie resonant regime while the green line represents the relevant Bragg resonant regime.

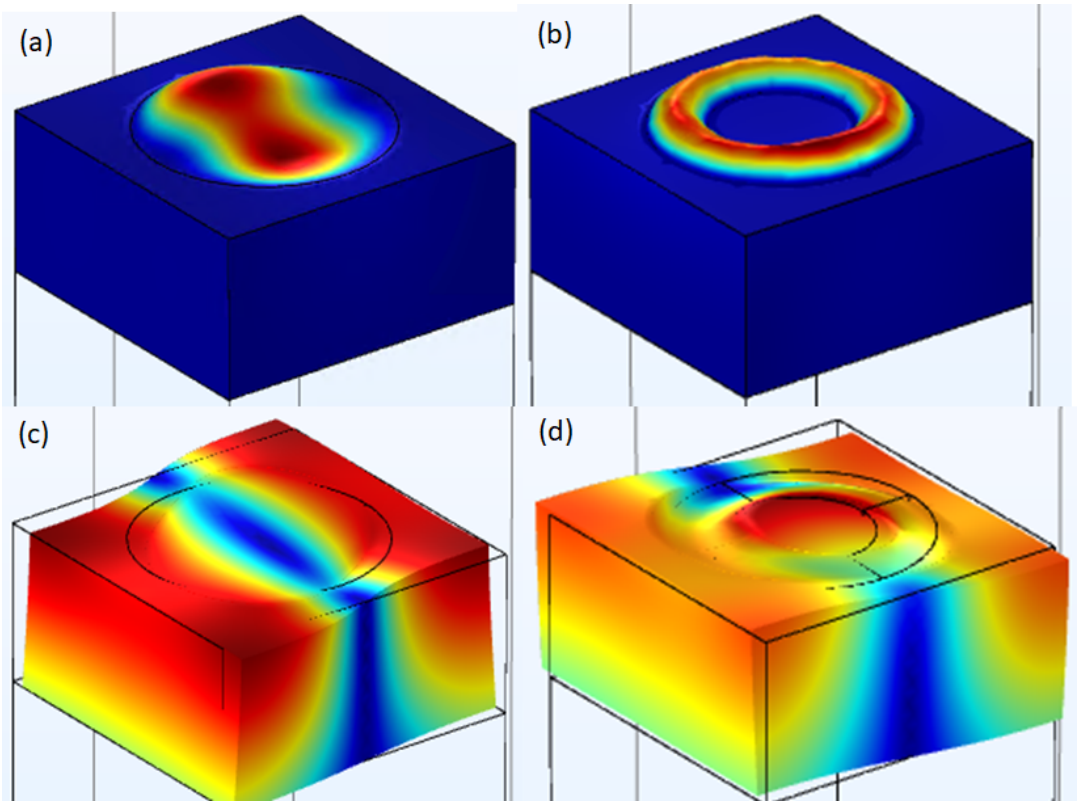

FIGURE 5.7: Indicative mode shapes, where the darkest red represents the largest displacement while the blue represents the smallest displacement. (a) 2nd order Mie resonance in a cylindrical hole (Material 50, 40 MHz), (b) fundamental radial Mie resonance ($r_2 - r_1$) in an annular hole (Material 50, 98 MHz), (c) fundamental Bragg resonance in a cylindrical hole (Material 30, 129 MHz), (d) fundamental Bragg resonance in an annular hole (Material 30, 140 MHz).

in the annulus (Mie regime) and agrees with the annular radial modes (the fundamental mode across the annular ring) predicted by the analytical model. At higher V_i Bragg scattering dominates, and displacement resonance is present across the unit cell, which is further evidence for $\Gamma - X$ Bragg scattering as the frequencies extracted from the simulation are consistent with those calculated from theory. Figures 5.6 and 5.7 also show that at lower V_i for annular holes, displacement is highest within the inclusion at the bandgap limits and is described by two ring modes, radial (across the ring) and circumferential (around the ring). For higher V_i at the bandgap limits, more Bragg resonance characteristics can be observed, with displacement modes extending across the unit cell and within the central region. For values of V_i spanning both regimes, a

combination of mode shapes can be seen.

The array of cylindrical holes forms a conventional phononic crystal where the bandgap characteristics primarily arise from the crystal geometry, meaning that the only factor affecting the position of the bandgap should be the period of the holes, a (12 µm). When the holes are empty, the main mechanism behind the origin of the bandgap is Bragg scattering in this case. However, adding materials to the holes introduces a Mie resonance at low V_i, which can be seen in Figure 5.7(a). At high values of V_i, Bragg scattering dominates.

When empty, the annular holes form an array of local resonators, with resonant frequencies determined by the displacement of the central pillar [39]. However, as material is added to the annular holes, as for cylindrical holes, the simulated bandgap frequencies are largely consistent with Mie and Bragg scattering at low and high values of the velocity respectively. At lower values of V_i in the Mie regime, displacement of the central pillar appears suppressed by the addition of material, seen in Figure 5.7(b), with the displacement confined to the annular ring. At high values of V_i, where Bragg scattering is dominant, there is still some displacement within the central pillar, suggesting that the characteristics of the array will be determined by a mixture of local resonator and Bragg like behaviour.

Differences between the simulated and calculated (using Equations 5.1 - 5.5) values of bandgap frequency may also be due to the 3D nature of the holes, and the conical nature of the inclusion, as Equations 5.1 and 5.4 assume the inclusion radius is constant with depth and is therefore only strictly valid at the surface for these geometries. This is particularly significant for the annular holes as they possess more conical elements than the cylindrical holes.

Finally, the effect of introducing materials on the bandgap widths was also considered, and simulated values of normalised bandgap width ($\Delta w/c\%$, where

Δw is the bandgap width and c is the bandgap centre) are plotted as a function of velocity, for both cylindrical and annular hole arrays, in Figure 5.8.

The widest bandgaps occur when scattering is highest, i.e. a combination of both Mie and Bragg scattering, and this can be seen particularly clearly for the annular holes near where the Mie and Bragg resonance lines cross in Figure 5.6. However, further analysis of the dependence of the bandgap width on the SAW velocity is complicated, due to the multiple mechanisms leading to the formation of a bandgap in these systems, and these results are shown for completeness only.

In conclusion, there is good agreement between the values of bandgap frequency extracted from the simulated bandstructure, and values calculated from the analytical model, for both the cylindrical and annular hole arrays, suggesting that Mie and Bragg scattering are important processes in both cases. For both systems, the bandgap frequency is more strongly dependent on the SAW velocity when the inclusion material has a relatively low velocity compared to the base material of lithium niobate, with a stronger dependence seen in the annular hole cases, as expected from the geometry, although more investigation is needed as to the underlying physics of both systems. This suggests that, even if the local resonator behaviour of the annular holes has been somewhat suppressed by the addition of an extra materials, annular holes are potentially a better route for creating tuneable phononic metamaterials.

5.4.2 Bandgap Attenuation

As well as tuneability, bandgap attenuation was obtained from transmission models in the frequency domain in COMSOL Multiphysics, following a method developed by Ash et al. [39]. 4 hole elements were patterned on a thin slab of $LiNbO_3$ as shown in Figure 5.1. Infinite Floquet periodicity conditions were again used on the long parallel sides. SAWs were launched over a range of

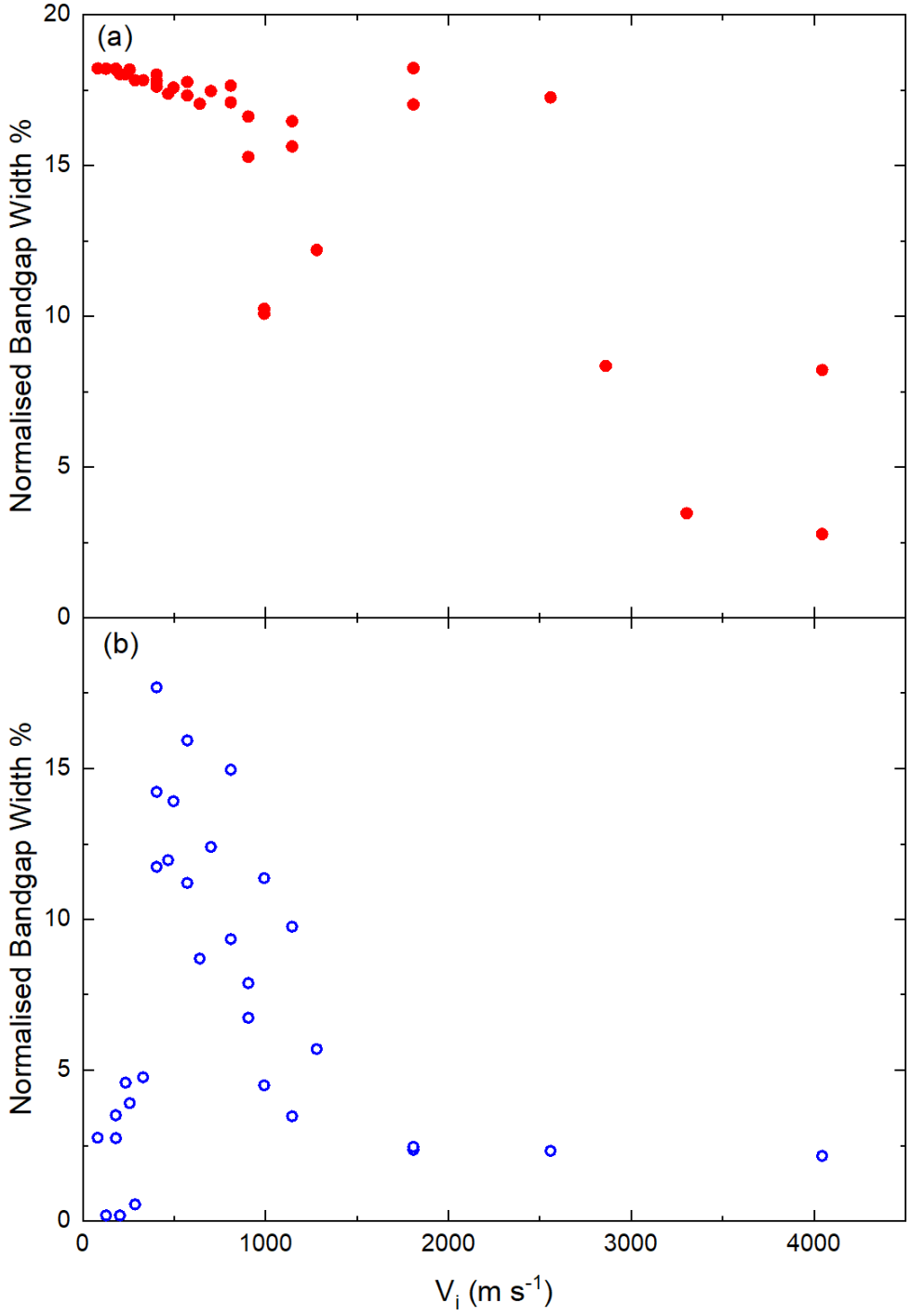

FIGURE 5.8: Normalised bandgap width as a function of filling material SAW velocity V_i for (a) cylindrical holes and (b) annular holes.

frequencies (1 - 250 MHz) from an edge load force, along a cut line perpendicular to the direction of propagation some distance away from the array.

When the holes were empty, the frequency at which the root-mean-square

(RMS) displacement of the SAW was lowest was extracted from a cut line positioned parallel to the direction of propagation and after the array, as shown schematically in Figure 5.9. Attenuation was then extracted at this frequency to allow for the fact that the maximum attenuation does not always occur at the centre of the bandgap predicted by the bandstructure model (for some materials, there is a discrepancy of up to 20 MHz), since the transmission model is only infinite on either side of the holes in the y-direction, and finite in the direction of SAW propagation (x-direction).

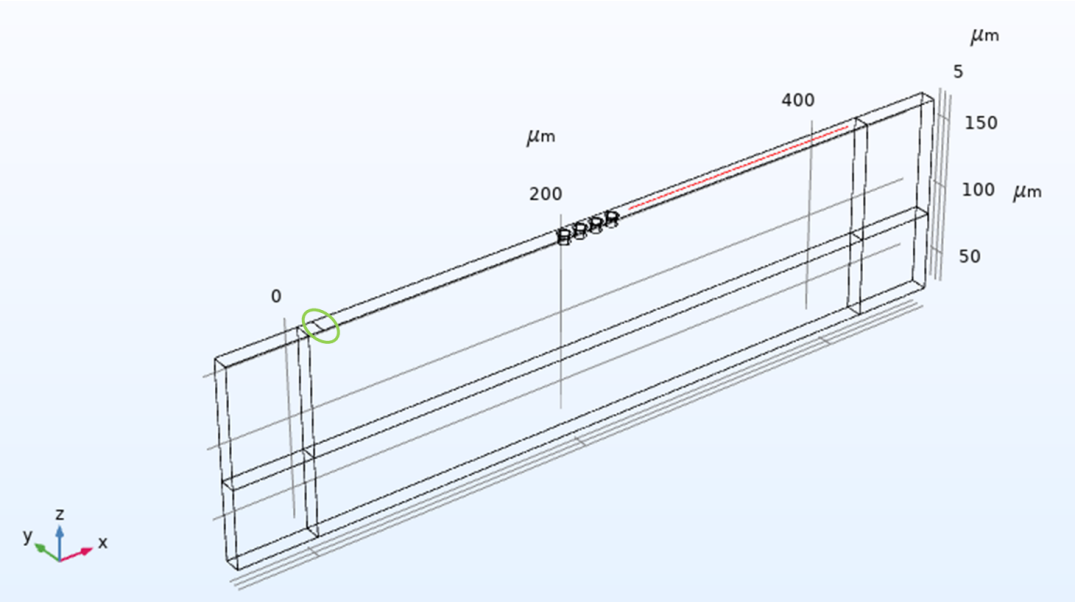

FIGURE 5.9: Example schematic of the transmission model geometry for 4 annular holes (the cylindrical hole model is exactly the same apart from the hole geometry). The SAW source is circled in green, and the cut line along which SAW displacements are extracted is plotted in red.

The x-displacement amplitude A_{holes} was then extracted along the same cut line, but at the frequency at which the RMS displacement was lowest. The same procedure was repeated on a blank (unpatterned) slab using the lowest RMS frequency as before, but extracting the x-displacement amplitude A_{blank} at the frequency corresponding to the model with the holes. Bandgap attenuation Γ in dB was then calculated using Equation 5.6:

$$\Gamma = 20 \log_{10} \left(\frac{A_{holes}}{A_{blank}} \right) \tag{5.6}$$

When the holes are empty, Γ has a value of -21.9 dB for cylindrical holes and -26.8 dB for annular holes, consistent with the findings of Ash et al. [39], who found Γ values of -19.0 dB and -24.5 dB for cylindrical pillars and annular holes (of a slightly different depths and radii) respectively.

The same process was then repeated to find the attenuation as the holes were filled with the different materials listed in Table 5.1 in the previous section (note that attenuation was extracted using materials for which there was a bandgap in the simulated bandstructures). Values of attenuation are plotted as a function of velocity in Figure 5.10, by calculating the bandgap attenuation again using Equation 5.6.

Although for both annular and cylindrical holes, the bandgap attenuation tends to increase with increasing velocity, attenuation is generally larger in the annular hole arrays compared to the cylindrical hole arrays. This is illustrated by plotting the ratio of the bandgap attenuation in the annular holes compared to that in the cylindrical holes, Figure 5.11, which shows that attenuation in the annular holes can be up to 3x greater than in the cylindrical holes. The biggest difference in the attenuation in the two types of arrays was at a velocity of approximately 600 m s^{-1}, where the bandgap is likely to be formed by a combination of Mie and Bragg scattering. There is also a large amount of scatter, suggesting that other factors affect the bandgap attenuation as well as V_i.

One reason why the attenuation in the annular holes is higher is that the annular hole arrays possess more interfaces where scattering can occur, leading to the SAWs losing greater energy when they propagate across the array.

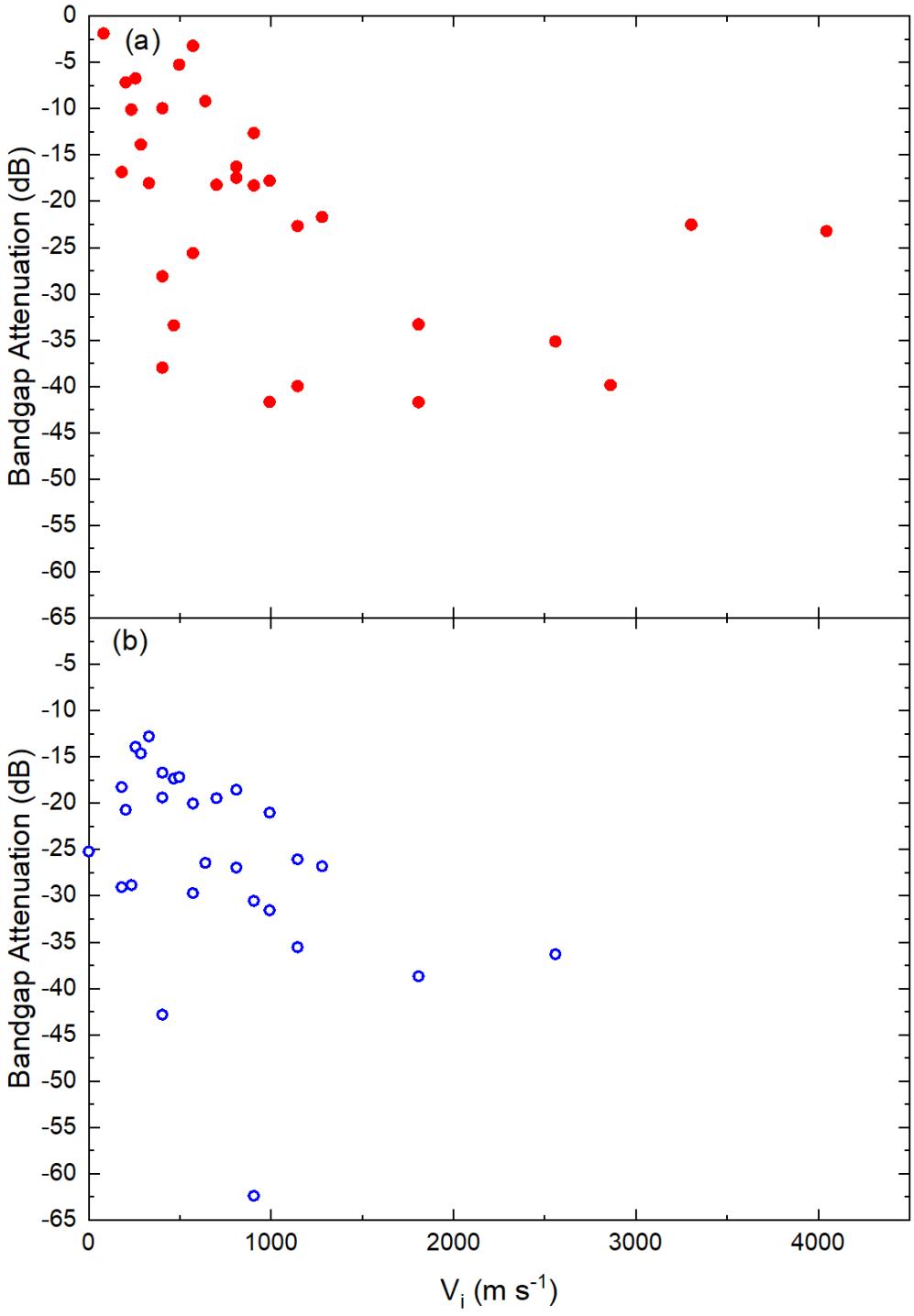

FIGURE 5.10: Bandgap attenuation as a function of filling material SAW velocity for (a) cylindrical holes and (b) annular holes.

The effect of the presence of materials within the holes can also be quantified by calculating Γ_{fill}, the attenuation caused by filling the holes:

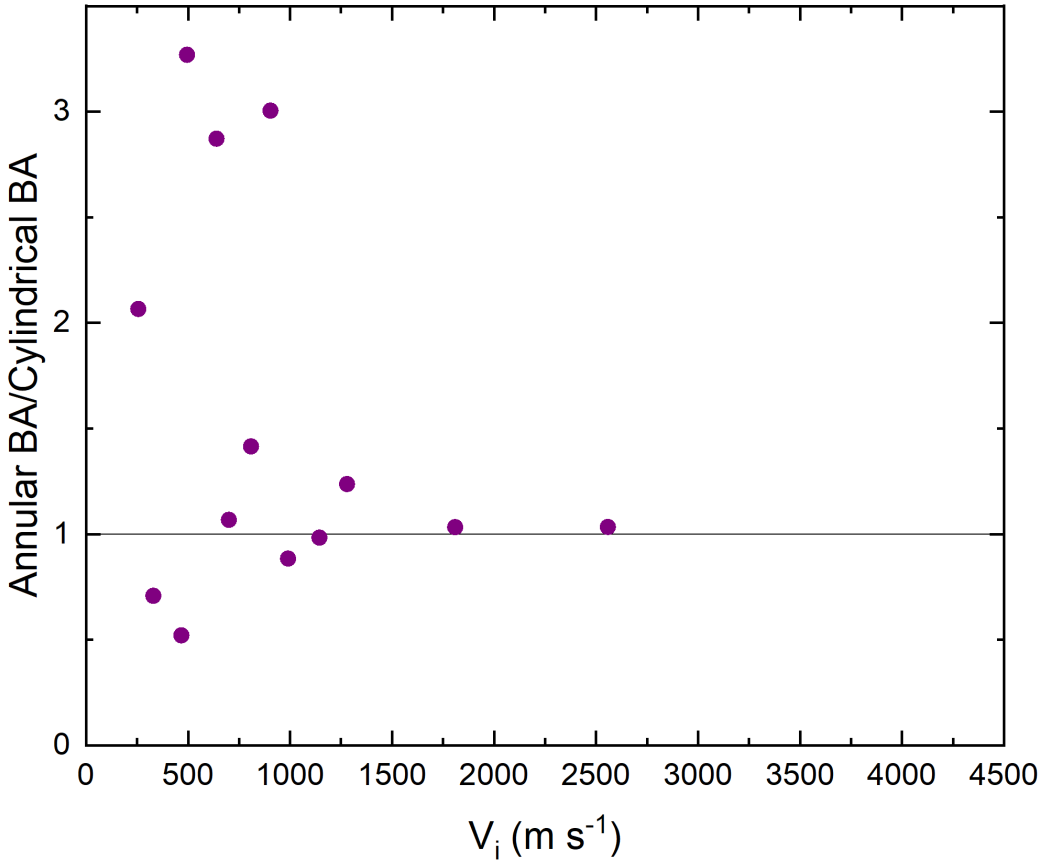

FIGURE 5.11: The ratio of annular hole bandgap attenuation over cylindrical hole bandgap attenuation as a function of filling material SAW velocity. Since most of the values are above 1, it is clear that annular holes exhibit more bandgap attenuation than cylindrical holes.

$$\Gamma_{fill} = 20 \log_{10} \left(\frac{A_{filled}}{A_{empty}} \right) \tag{5.7}$$

This attenuation is plotted as a function of velocity for both cylindrical and annular holes in Figure 5.12, and again demonstrates that overall annular holes exhibit higher attenuation that cylindrical holes when filled with material, and are therefore more sensitive to the presence of an additional material. The ratio of Γ_{fill} for annular and cylindrical holes is plotted as a function of velocity in Figure 5.13, with values at most velocities again being above 1.

This higher bandgap attenuation in annular hole arrays as additional materials are added to the system suggests that the use of annular hole arrays might

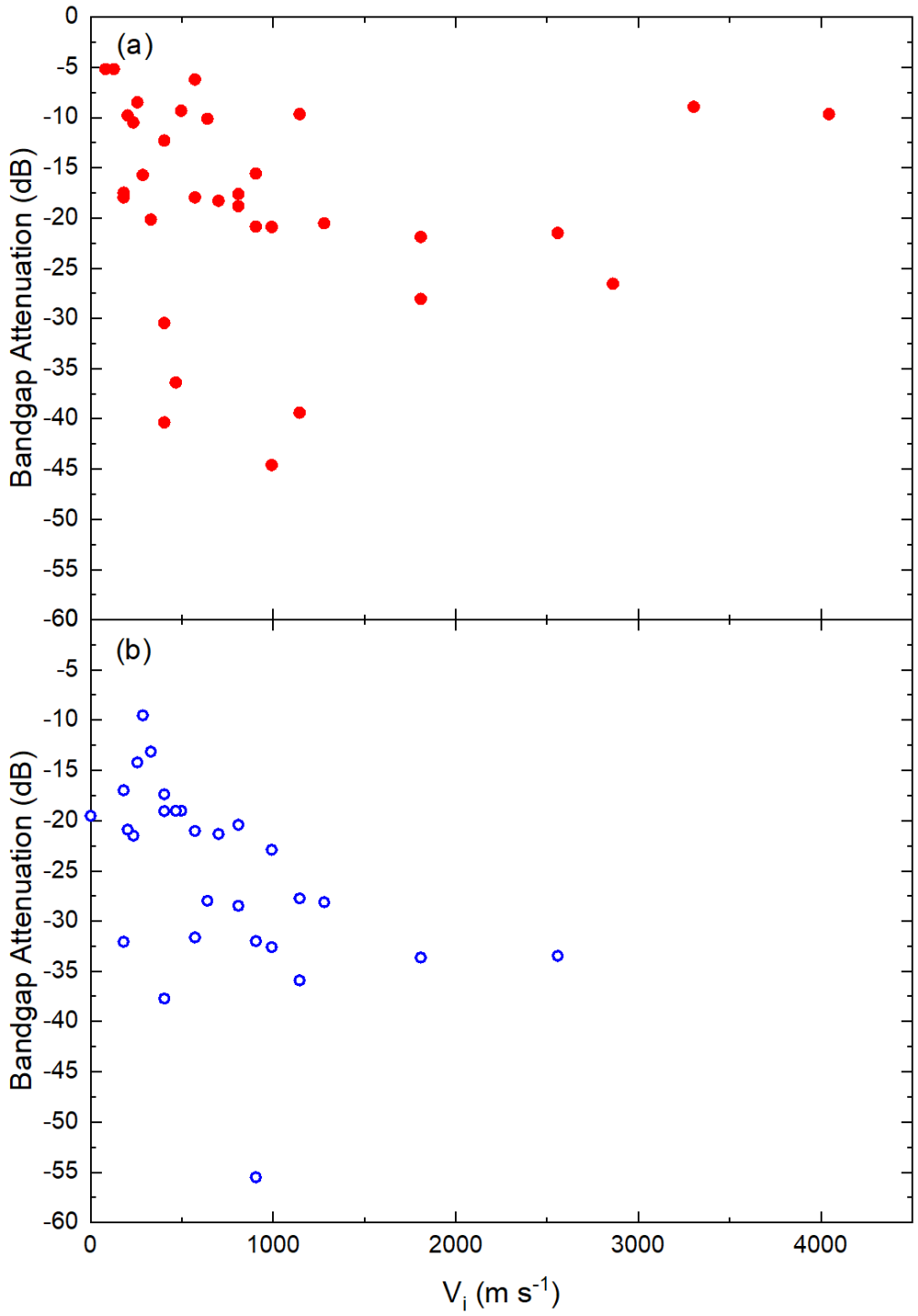

FIGURE 5.12: Bandgap attenuation of filled holes compared to empty holes as a function of filling material SAW velocity for (a) cylindrical holes and (b) annular holes.

lead to greater sensitivity (in that obvious and easily measurable effects are observed when the inclusion material is slightly varied) in devices designed for applications such as mass loading sensing.

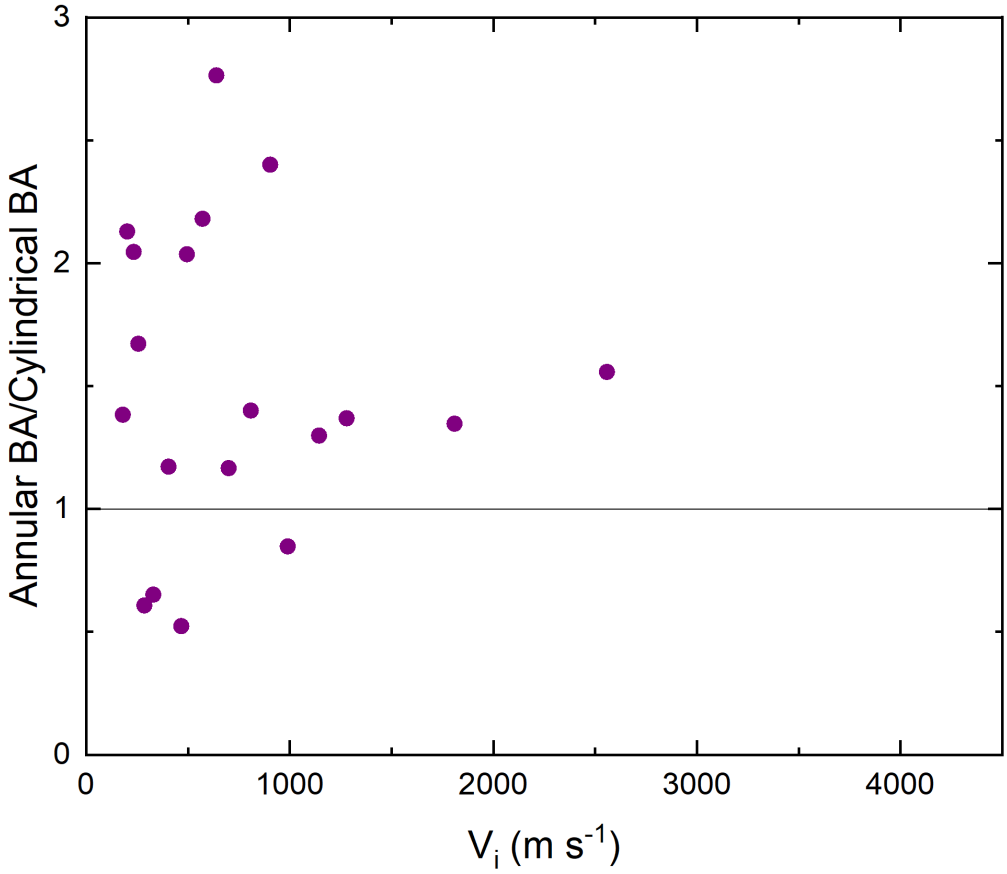

FIGURE 5.13: Calculated compared to empty holes rather than an unpatterned surface. The ratio of annular hole bandgap attenuation over cylindrical hole bandgap attenuation as a function of filling material SAW velocity. Since most of the values are above 1, it is clear that annular holes exhibit more bandgap attenuation than cylindrical holes.

5.5 Summary

Bandstructures were obtained from finite element simulations for arrays of cylindrical and annular holes, as the holes were filled with materials with different SAW velocities V_i. By comparison to bandgap frequencies calculated using an analytical model, it was found that each type of hole array exhibited a Mie scattering regime at lower V_i and a Bragg scattering regime at higher V_i. The dependence of the bandgap frequency on the velocity was found to be higher for the annular holes than for cylindrical holes, suggesting that the annular holes are potentially a better route for creating tuneable phononic metamaterials. The displacement within the arrays was also investigated. At low values of

V_i, the displacements were consistent with Mie scattering for both annular and cylindrical holes. At high values of V_i, the displacements in both hole arrays were consistent with Bragg scattering, but in the annular holes displacement of the central pillar could also be seen.

The bandgap attenuation was also investigated with a finite element simulation and calculated with respect to either a blank surface or empty holes. In both cases the annular holes displayed a higher bandgap attenuation, by up to a factor of 3x compared to the attenuation in arrays of cylindrical holes. The largest difference in the attenuation between the two types of arrays was at the SAW velocity when both Mie and Bragg scattering are thought to contribute to the formation of a bandgap, suggesting that it might be the greater number of interfaces in the annular holes that lead to this greater attenuation. The use of annular hole arrays might lead to greater sensitivity in devices designed for applications such as mass loading sensing.

Chapter 6

Mass Loading Effects in a Phononic Metamaterial

6.1 Overview

SAW devices lend themselves to a wide range of diverse applications, including telecommunications, microfluidics (particle separation, cell sorting, fluid manipulation and mixing), and sensing (chemical, pressure, humidity). Recent work by Kumar et al. [58] has even found that SAW pressure sensors can be exploited in hospitals for the monitoring of COVID-19 patients.

The out-of-plane displacement component means that SAWs, confined to the surface of materials, are susceptible to attenuation. There are many ways in which SAWs can be attenuated, such as boundary scattering or changes in elastic properties of propagation media, but in the presence of gases, liquids, or any other material present on the substrate surface, a process known as mass loading attenuation can occur. SAW mass loading attenuation can manifest itself through a number of mechanisms, but is commonly measured using a chemical adsorption layer on top of the substrate, through which chemical or conductivity changes caused by the external environment are measured through a frequency, velocity or phase shift of the SAW in an oscillator circuit after

propagating through the adsorption layer [32]. High levels of sensitivity to these changes has led to applications in gas sensing for safety. Less explored is the direct measurement of SAW amplitude on device surfaces to calculate the mass loading attenuation of the SAW, where difficulty is often posed in precisely measuring picometre amplitudes, but this method shows great promise for gas pressure sensing applications.

In between generation and detection, SAW propagation can also be controlled on the main surface of devices between interdigital transducers (IDTs) through the use of surface patterning, some effects of which were explored in Chapter 5. Phononic metamaterials are useful in SAW delay line applications due to their exhibition of high bandgap attenuation, and it has already been demonstrated in Chapter 5 that they are sensitive to changes in their environment.

Annular hole array elements, as found by Ash et al. [39] and explored partially in Chapter 5, show great promise since only a few elements are needed to produce the equivalent bandgap attenuation as many hole or pillar elements in the same substrate, with the particular advantage of them being easier and quicker to fabricate than conventional phononic crystals. The individual array elements also have more degrees of freedom in design for tuning.

Slobodnik [34] explored mass loading effects on substrates in the absence of surface patterning, so in this chapter a phononic metamaterial is introduced (a square array of annular holes), which exhibits an extraordinary increase in attenuation due to mass loading across the metamaterial array at the bandgap frequency. In this chapter this phenomenon is explored experimentally and computationally, and it is proposed that similar devices show great promise in increasing the sensitivity of SAW gas pressure sensors.

6.2 Mass Loading Theory

There are several different sources of mass loading attenuation on SAW devices which can be broken down into individual attenuation coefficients. The attenuation coefficient of mass loading due to the presence of gas (in Nepers per metre, similar to dB but using the natural logarithm rather than base 10) in the absence of surface patterning, α, can be predicted according to theory developed by Slobodnik [34], seen in Equation 6.1:

$$\alpha = \frac{fP}{\rho_s v_s^2} \left(\frac{\gamma M}{RT} \right)^{1/2} \tag{6.1}$$

where f is the SAW frequency, P is the pressure of the gas, ρ_s is the substrate density, v_s is the speed of sound in the substrate, γ is the ratio of specific heats, M is the molar mass of the gas, R is the universal gas constant and T is the temperature.

Values of the attenuation coefficient calculated for air at a pressure of 1 atmosphere are plotted as a function of SAW frequency on the blue line in Figure 6.1. At a SAW frequency of 100 MHz, the mass loading attenuation coefficient for a blank device is approximately 0.5 Np m^{-1}.

In practice, SAW amplitudes were measured and converted into attenuation coefficients. A visual explanation of the origin of the mass loading coefficients as demonstrated on an example device can be seen in Figure 6.2, whereas a fully labelled schematic of the fabricated device can be seen in Figure 6.3. For mass loading on a blank device (unpatterned), amplitudes were measured in air and vacuum, and the attenuation coefficient α_g was calculated as:

$$\alpha_g = -\frac{1}{L_B} \ln \left(\frac{A_g}{A_0} \right) \tag{6.2}$$

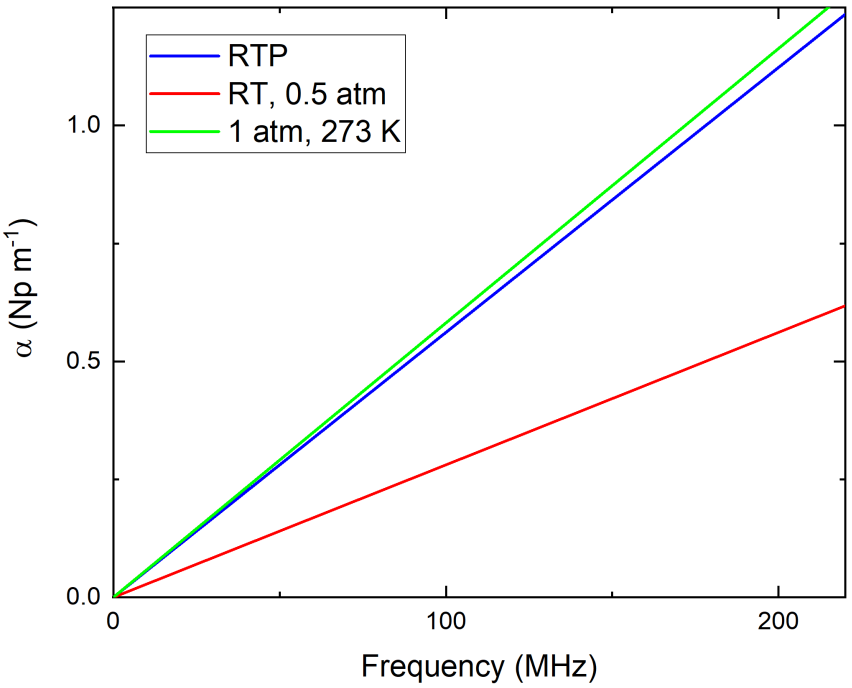

FIGURE 6.1: The mass loading attenuation coefficient calculated for air plotted as a function of SAW frequency for 3 different pressure and temperature conditions - RTP i.e. 1 atm and 293 K (blue line), 0.5 atm and 293 K (red line), and 1 atm and 273 K (green line).

where L_B is the propagation length, A_g is the SAW amplitude in the presence of gas, and A_0 is the SAW amplitude in vacuum.

Surface patterning also contributes to attenuation, and this attenuation coefficient α_{ph} was calculated by comparing the measured amplitude on a patterned device to that of a blank device (both in vacuum), seen in Equation 6.3:

$$\alpha_{ph} = -\frac{1}{L_{ph}} \ln\left(\frac{A_{ph}}{A_0}\right) \tag{6.3}$$

where L_{ph} is the length of the resonator array pattern, A_{ph} is the SAW amplitude on a patterned device and A_0 is the same as in Equation 6.2. When calculating this parameter from laser Doppler vibrometry data or simulations,

the expression for the attenuation coefficient due to the resonator array is modified to:

$$\alpha_{ph} = -\frac{1}{L_{ph}} \ln\left(\frac{A_{2v}}{A_{1v}}\right) \tag{6.4}$$

where A_{2v} is the (average) measured SAW amplitude close to the final array element in vacuum, and A_{1v} is the (average) measured SAW amplitude close to the first array element in vacuum.

Since measured amplitudes on the oscilloscope system (discussed later) include all contributions to attenuation, the attenuation coefficient due to mass loading just across the patterned area of the device, α_{pg}, can be written as:

$$\alpha_{pg} = \frac{-\left(\ln\left(\frac{A_{pg}}{A_{ph}}\right) + \alpha_g L_{np}\right)}{L_{ph}} \tag{6.5}$$

where A_{pg} is the SAW amplitude on a patterned device in the presence of gas, L_{np} is the non-patterned path length, and any repeated terms remain the same as before from Equations 6.2 and 6.3.

When calculating this parameter from LDV data or simulations, the attenuation coefficient due to mass loading across the patterned area is modified to:

$$\alpha_{pg} = -\frac{1}{L_{ph}} \ln\left(\frac{A_{2g}}{A_{1g}}\right) - \alpha_{ph} \tag{6.6}$$

where A_{2g} is the (average) measured SAW amplitude close to the final array element in the presence of gas, A_{1g} is the (average) measured SAW amplitude close to the first array element in the presence of gas, and any repeated terms remain the same as before from Equation 6.4.

The bandgap attenuation coefficient Γ (in dB) can also be extracted in a similar way as described in Chapter 5. These quantities can be calculated for each frequency from the measured amplitude A in each scenario. In vacuum Γ is defined:

$$\Gamma_{vac} = 20 \log_{10} \left(\frac{A_{holes.vac}}{A_{blank.vac}} \right) \tag{6.7}$$

while in air the expression is modified to:

$$\Gamma_{air} = 20 \log_{10} \left(\frac{A_{holes.air}}{A_{blank.vac}} \right) \tag{6.8}$$

6.3 Device Design and Measurements

A schematic of the device, including the location of the resonator array between the interdigital transducers and the resonator geometry can be seen in Figure 6.3. A summary of the methods behind the device design, preparation and characterisation can be found in Chapter 4, from section 4.4 onward.

Only one patterned device was fabricated and measured to give the results presented here. For the oscilloscope system, each SAW frequency was measured on a blank device and on a patterned device, once in air and once in vacuum.

6.4 Experimental Results

6.4.1 Oscilloscope System

The mass loading attenuation coefficients for unpatterned (α_g) and patterned (α_{pg}) devices measured on the oscilloscope are plotted as a function of SAW frequency in Figure 6.4. The values for α_g on the unpatterned device are consistent

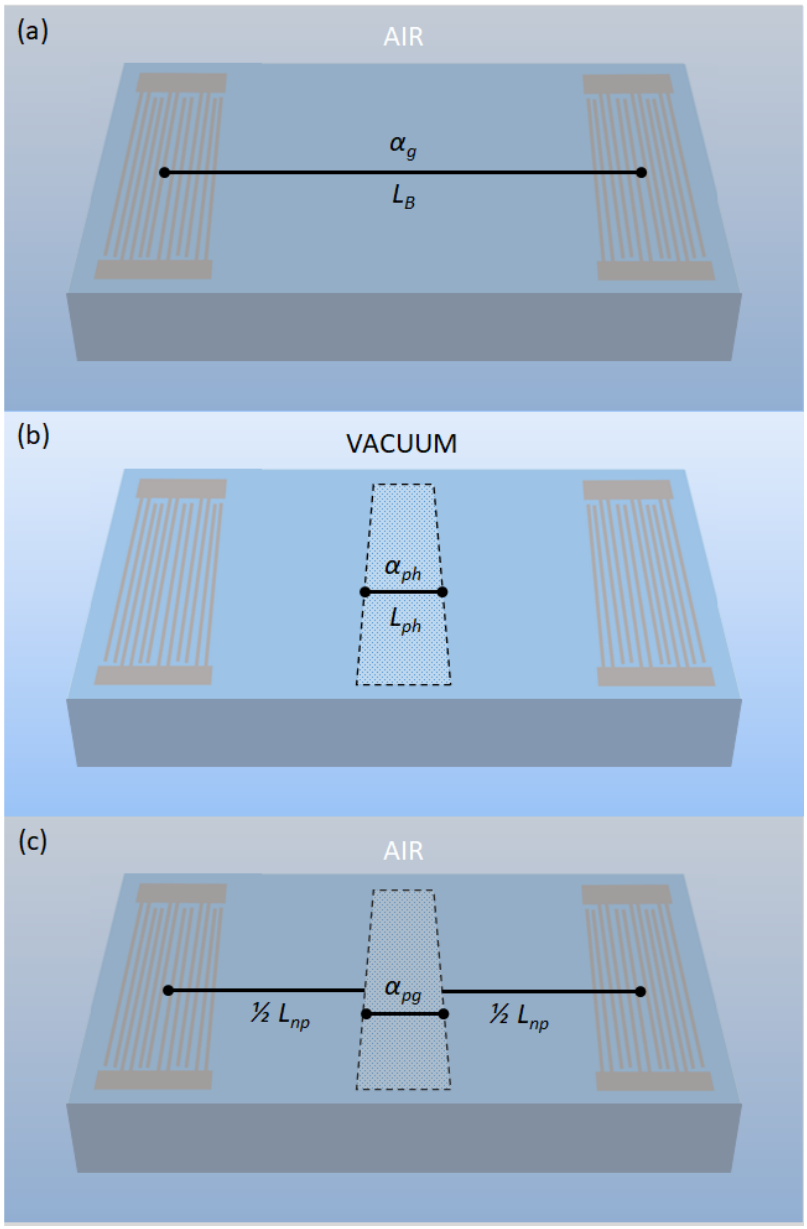

FIGURE 6.2: Not to scale. The striped grey domains at either end represent the interdigital transducers (IDTs) where SAWs are launched and detected respectively. The rectangular dotted domain represents the area where surface patterning is present. (a) blank device in air, where α_g is measured along L_B, (b) patterned device in vacuum, where α_{ph} is measured along L_{ph} and (c) patterned device in air, where α_{pg} is measured along L_{ph} and α_g (measured from (a)) contributes along L_{np}.

with the theory (Equation 6.1), which predicted an attenuation coefficient that linearly increases with frequency. When the resonator array (phononic metamaterial pattern) is present, nearly all the attenuation coefficients α_{pg} are at least two orders of magnitude higher, with the largest attenuation coefficient

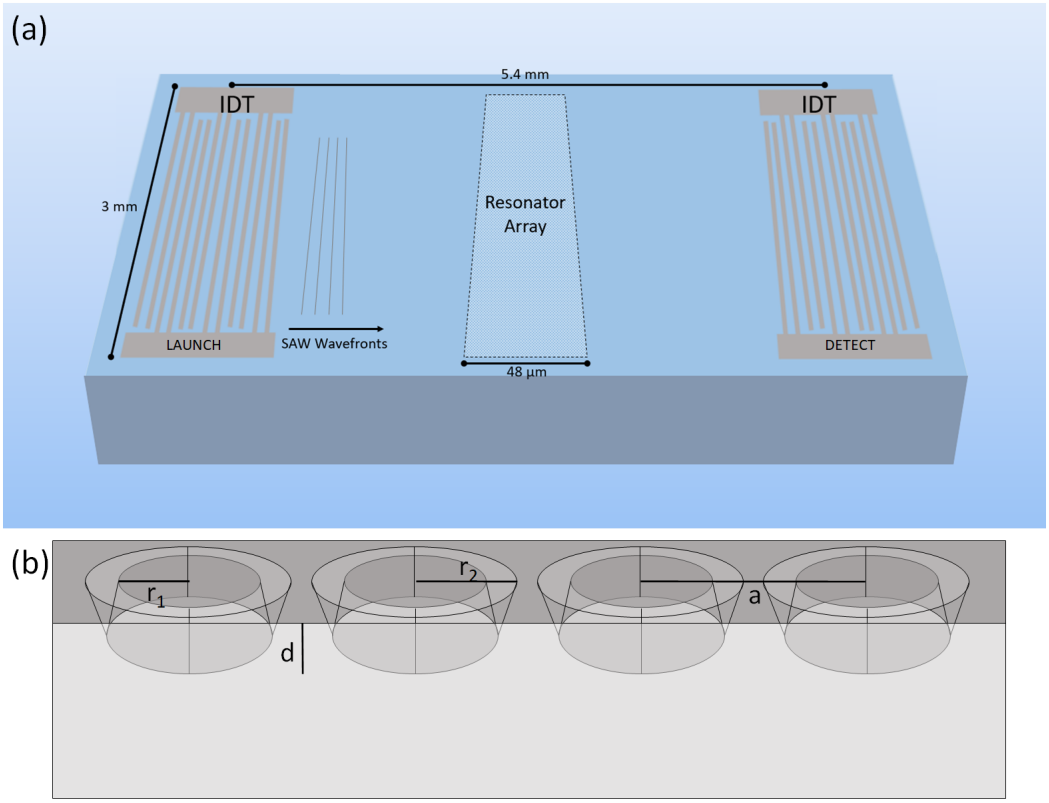

FIGURE 6.3: Not to scale. (a) Device schematic showing the location of the resonator array patterned between the interdigital transducers (IDTs) of a SAW delay line, (b) schematic diagram of the resonator geometry, where the inner radius r_1 is 3.5 µm, the outer radius r_2 is 4.5 µm, the depth d is 6 µm and the lattice constant a is 12 µm.

being observed at the frequency of the lowest SAW bandgap, 97 MHz (hereafter referred to as the bandgap frequency - other higher order bandgaps exist in this system but the lowest one is most important for this chapter), with a value of 1711 Np m^{-1}, which is more than 2000 times higher than what was measured at the same frequency on the blank device, and over 3000 times higher than what was predicted by the theory in the absence of surface patterning. In Equation 6.5 the dominating factor is A_{pg}, suggesting that most of the enhancement is due to the movement or vibration of the pattern.

Sources of uncertainty may arise from the sensitivity of the oscilloscope and associated experimental setup. In addition, imperfect flushing of the vacuum

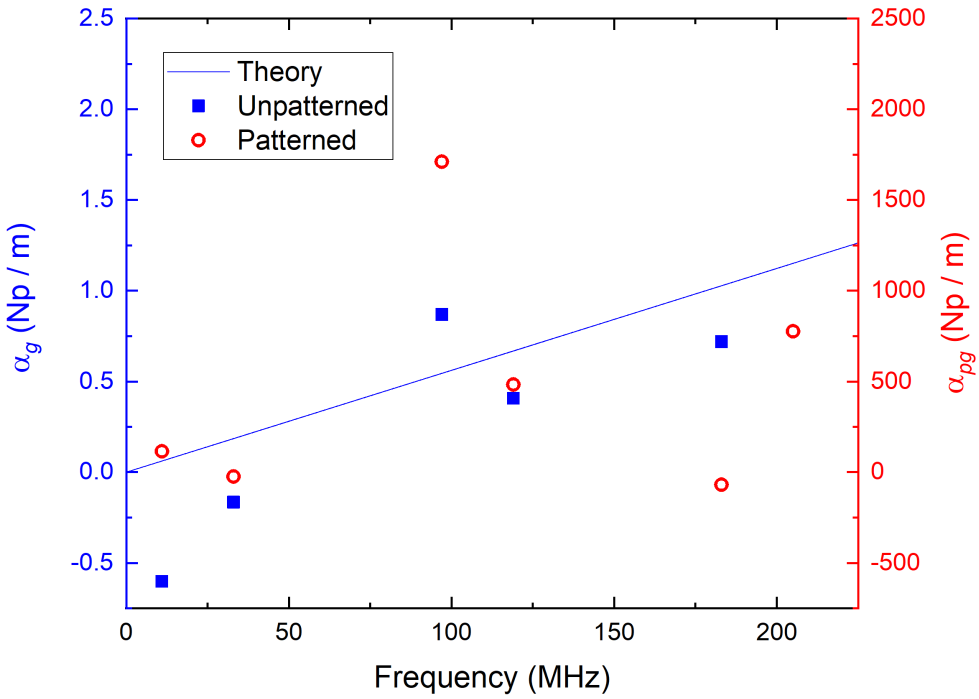

FIGURE 6.4: Measured gas loading attenuation coefficient for an unpatterned device, α_g (blue symbols, left y-axis), and due to the resonator array, α_{pg}, (red symbols, right y-axis. The straight blue line (left y-axis) is the calculated gas loading for an unpatterned device.

chamber can also lead to water vapour condensing on the device surface, manifesting in an artificial increase in mass loading. However, due to the highly resolved digitising of the waveform by the oscilloscope and the excellent fit of the sine-fitting function used to obtain and calculate SAW amplitudes, calculated uncertainties in the values of the mass loading attenuation coefficients were too small to be visible at the scales shown in Figure 6.4 and have therefore been omitted.

Taking these factors into consideration, it is clear that the patterned device exhibits high mass loading attenuation due to the presence and motion of the pattern, which is particularly demonstrated by the significantly higher value at the bandgap frequency.

Bandgap attenuation coefficients Γ (Equation 6.7) were calculated for the patterned device at each IDT frequency in both vacuum and air, and are plotted in Figure 6.5. At 97 MHz, Γ_{vac} has a value of -10.3 dB (-118 Np), consistent with the findings of Ash et al. [39] who measured a value of -12.6 dB (-145 Np). Overall slightly more attenuation is observed in air than in vacuum, but the biggest difference at 97 MHz where Γ_{air} is almost 1 dB (almost 11 Np) higher than Γ_{vac} at at -11.1 dB (-128 Np). This is more evidence that surface patterning increases attenuation due to mass loading.

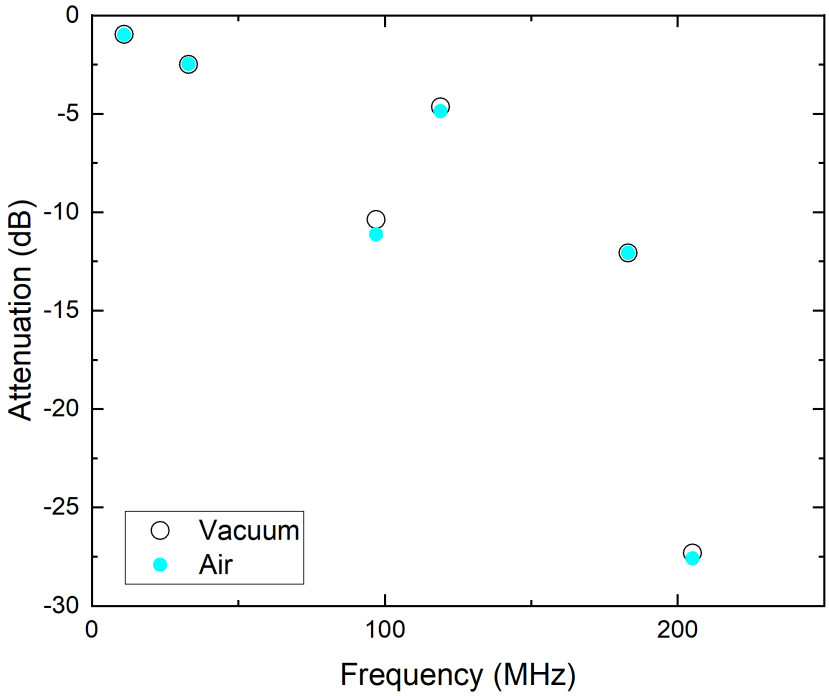

FIGURE 6.5: Measured attenuation Γ (in dB) for the patterned device in vacuum and in air plotted as a function of frequency.

6.4.2 Laser Doppler Vibrometry

The mass loading attenuation coefficient due to the resonator array (α_{pg}) extracted from LDV measurements plotted as a function of frequency can be seen in Figure 6.6. Here the attenuation coefficients are three orders of magnitude

higher than those observed on the unpatterned device, and the largest attenuation coefficient is still observed at the bandgap frequency, 97 MHz, with a value of around 22000 Np m^{-1}.

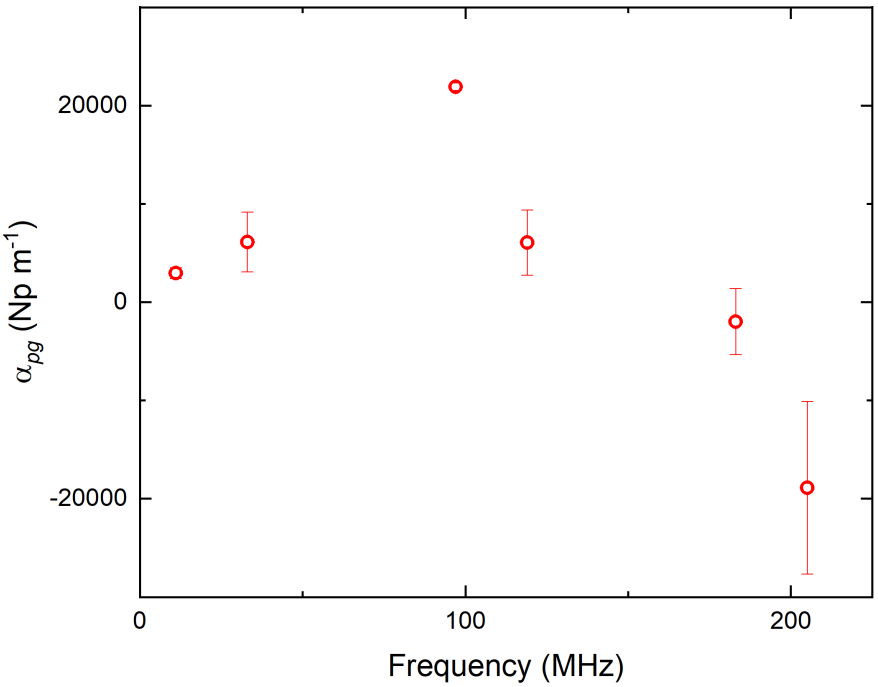

FIGURE 6.6: Measured gas loading attenuation coefficient due to the resonator array, α_{pg}, extracted from laser Doppler vibrometry measurements, plotted as a function of frequency.

When investigating the LDV attenuation coefficients, values of the mass loading attenuation coefficient are 10 times higher again than the resonator array measured with the oscilloscope system. Overall the mass loading attenuation coefficients follow a similar frequency dependence, with the highest mass loading attenuation observed clearly at 97 MHz, with a value more than three times higher than the next nearest value. Possible reasons for the difference in magnitude compared to the oscilloscope system include the fact that only out-of-plane displacements are measured on the LDV whereas the oscilloscope system is sensitive to all displacements experienced by the IDTs i.e. shear components and bulk waves etc. The oscilloscope system is also sensitive to mass loading on

the non-patterned area of the device, which introduces a degree of complexity into unravelling the different attenuation coefficients, whereas the LDV only measures the SAW directly before and after the array. The LDV operates in the frequency domain rather than the time domain of the scope, meaning a 'snapshot' of the SAW is investigated for amplitudes which are subsequently extracted directly with units of picometres. The data gathering process also has a number of averaging steps in both pre- and post-processing, possibly leading to loss of resolution from not using the sine-fitting function. Negative values of α_{pg} have been assumed to be insignificant, especially at higher frequencies where higher order bandgaps may be present, and other reflective effects may occur which may falsely increase the amplitude after the pattern.

The mass loading attenuation coefficients due to the resonator array (α_{pg}) extracted from oscilloscope and LDV measurements, normalised to the corresponding value at the bandgap for each measurement system, are plotted as a function of frequency in Figure 6.7. This demonstrates that both measuring techniques exhibit a similar frequency dependence at different orders of magnitude (with the exception of the values at 205 MHz, where there might be a higher order bandgap as seen in the simulated full bandstructures in Figure 5.4 in Chapter 5, which may lead to difficulty in interpreting SAW effects observed at higher frequencies). Both have a maximum mass loading attenuation coefficient at the bandgap frequency, 97 MHz, with values more than twice as high as the next nearest value and up to four times as high as other values. This is further evidence of an extraordinary increase in mass loading due to the resonator array in the bandgap.

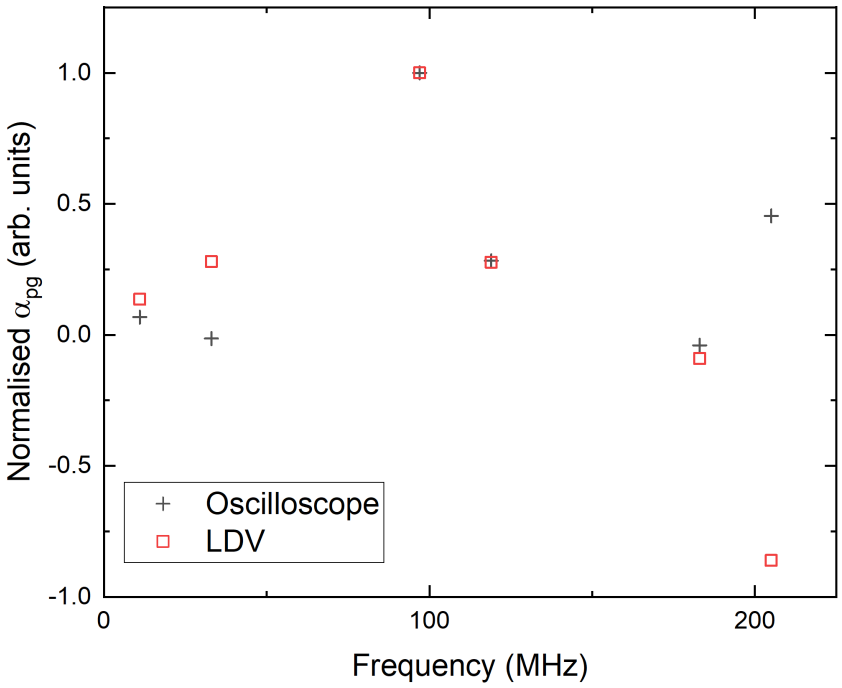

FIGURE 6.7: Mass loading attenuation coefficients due to the resonator array (α_{pg}) extracted from oscilloscope and LDV measurements, normalised to the value at the bandgap frequency (97 MHz) for each system (1711 Np m^{-1} for the oscilloscope system and 21922 Np m^{-1} for the LDV), plotted as a function of frequency.

6.5 Simulations

6.5.1 Setup

The experimental geometry (unpatterned $LiNbO_3$ substrate with infinite Floquet periodicity conditions, and subsequently with 4 annular hole elements) was recreated in transmission models in COMSOL Multiphysics following work by Ash et al. [39], and investigated in both a vacuum and in air. The geometry was identical to the transmission model in Chapter 5, but the annular holes had slightly different dimensions to reflect what was fabricated, and also an air domain was added above the substrate surface (using Pressure Acoustics, frequency domain interface and Acoustic-structure boundary multiphysics).

SAWs were generated by an edge load along a cut line perpendicular to the direction of propagation, negating the need to include transducers in the model geometry and electrostatics setup. The average SAW amplitude was extracted from the out-of-plane displacement field component measured along a cut line running the entire length of the blank model, and subsequently the amplitudes of individual wave peaks before and after the resonator array on a patterned model were extracted at each frequency. The out-of-plane displacement field component was chosen over the RMS or out-of-plane displacement amplitude (used in Chapter 5) as the oscillation was primarily symmetrical about 0 (the device surface) and most closely mirrors the measurements taken from the LDV. The wavelength was also consistent with distance and frequency unlike some of the other displacement field or amplitude components. Equations 6.4 and 6.6 could be used again to calculate the attenuation coefficients. The bandstructure of one individual hole was also investigated in vacuum, again following work by Ash et al. [39], using an eigenfrequency study of one unit cell.

6.5.2 Results

The simulated bandstructure of the $\Gamma - X$ path in the first Brillouin zone of the resonator array obtained from the resonator supercell in vacuum can be seen in Figure 6.8. It can be seen that the third IDT resonant frequency, 97 MHz, lies very close to the lowest simulated SAW bandgap, which has a lower limit of 98.1 MHz, while the fourth IDT resonant frequency, 119 MHz, falls within the bandgap. Other higher order bandgaps open up at higher frequencies. The simulated bandstructure produced agrees well with Ash et al. [39] who observed a bandgap around 97 MHz in vacuum. The introduction of air here is not trivial due to the coupling of an additional and completely different physics interface in a separate domain (whereas in Chapter 5, the coupling was between two separate domains with the same physics interface) and even with extensive discussions

with and support from engineers at COMSOL, additional bandstructures were produced with limited success and have not been included in this chapter.

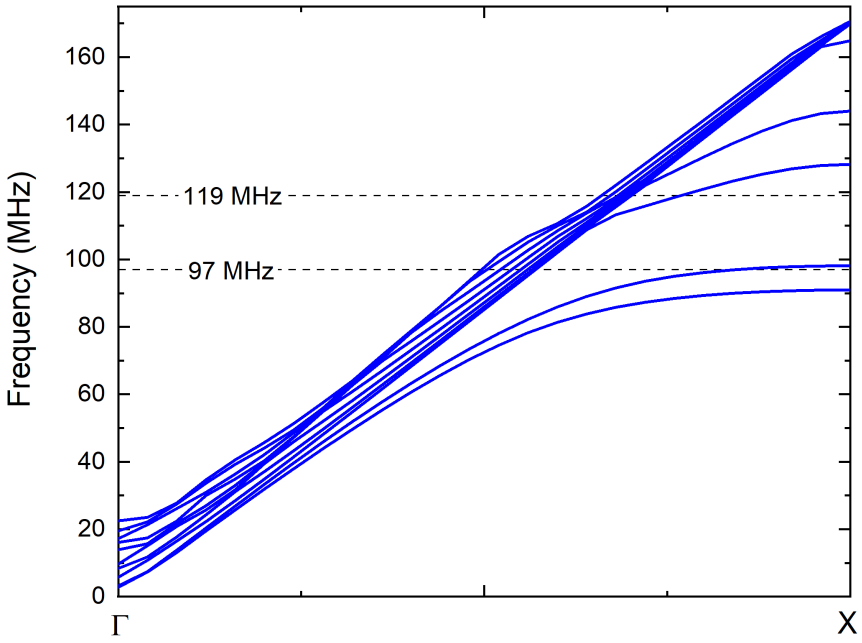

FIGURE 6.8: Simulated bandstructure of the $\Gamma - X$ path in the first Brillouin zone for an infinite square array of annular holes in vacuum.

According to experimental results, 97 MHz lies within the lowest SAW bandgap on the patterned device as seen in Figure 6.5, but according to the simulated bandstructure in Figure 6.8, the highest attenuation should occur at 119 MHz since that frequency falls within the bandgap.

Indicative displacement mode shapes at the simulated bandgap limits (98 MHz and 128 MHz) in vacuum can be seen in Figure 6.9. At 98 MHz the highest displacement is at the top of the pillar, meaning that the surface there could be most susceptible to changes in out-of-plane displacement in the presence of gas around that frequency (observed experimentally). At the 128 MHz a Bragg-like mode (see Chapter 5) can be seen with comparatively little displacement of the pillar, with higher displacement at the unit cell edges.

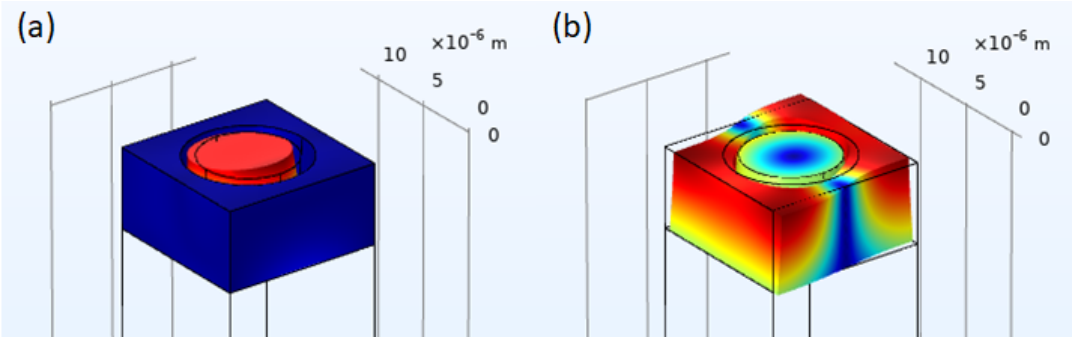

FIGURE 6.9: Indicative mode shapes simulated in vacuum at (a) 98 MHz, the lower bandgap limit and (b) 128 MHz, the upper bandgap limit. The darkest red shade indicates the highest displacement while the darkest blue indicates zero displacement.

The out-of-plane displacement field component can be seen in Figure 6.10. At 98 MHz (a), out-of-plane displacement is concentrated inside the pillar with zero displacement of the surrounding substrate, while at 128 MHz, almost no out-of-plane displacement occurs in the pillar, with the majority of the displacement occurring near the unit cell corners. The higher proportion of displaced surface within the unit cell at 128 MHz (compared to 98 MHz) suggests that SAW frequencies around that value may be more susceptible to mass loading.

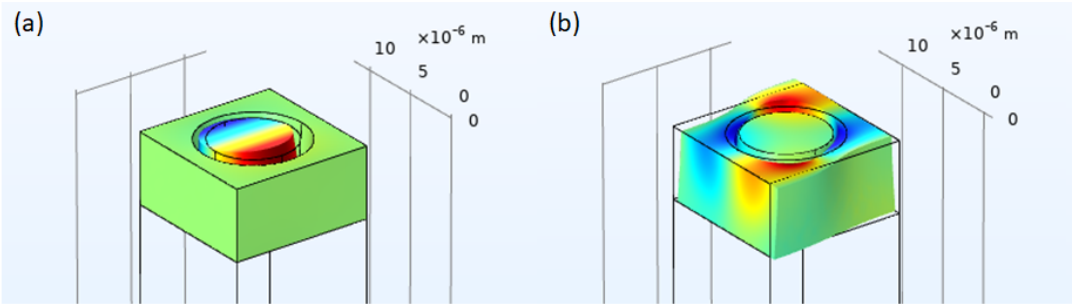

FIGURE 6.10: Indicative mode shapes simulated in vacuum at (a) 98 MHz, the lower bandgap limit and (b) 128 MHz, the upper bandgap limit. The darkest red shade indicates the highest displacement while the darkest blue indicates zero displacement.

The simulated bandgap attenuation coefficient in vacuum, Γ_{vac}, has a value of -26.8 dB (-308 Np) at a frequency of 88 MHz, consistent with the findings of Ash et al. [39], who found a Γ_{vac} value of -24.5 dB (-282 Np) for simulated annular holes of a slightly different geometry. When air is added, Γ_{air} is almost double Γ_{vac} with a value of -45.8 dB (527 Np) which is a significant increase.

The mass loading attenuation coefficients extracted from simulations are plotted as a function of frequency in Figure 6.11, where the blue symbols in Figure 6.11(a) represents the unpatterned device model and the red symbols in Figure 6.11(b) represents the resonator array model. Again, the behaviour of the simulated unpatterned device is consistent with the theory, with a linear increase in attenuation coefficient with frequency and at a similar order of magnitude. However, when the resonator array is present, the simulation does not reproduce the increase in gas loading attenuation at 97 MHz which was measured with both the oscilloscope and the LDV. The highest attenuation coefficient (with the exception of the value at 205 MHz) occurs at 119 MHz, well within the simulated SAW bandgap, with a value of 5 Np m^{-1} (to which the data in Figure 6.11(b) has been normalised for easier comparison to the behaviour of the experimental systems). While it may occur at a different frequency, this is still consistent with the behaviour observed experimentally, with the highest mass loading attenuation being observed at the bandgap frequency of each respective system.

The theoretical expression for mass loading attenuation was only explored by Slobodnik at frequencies several orders of magnitude higher than those investigated here, and it has been assumed that the expression obtained by Slobodnik applies at all frequencies. The expression also includes a temperature term, the effects of which however have been assumed to be negligible as all experiments were undertaken at a constant temperature of 21.5 °C and default COMSOL settings are always at RTP.

6.6 Summary

SAW attenuation due to mass loading of air was obtained by directly measuring SAW amplitude on a SAW device using an oscilloscope system and by laser Doppler vibrometry (LDV). An extraordinary increase of 2 to 3 orders of

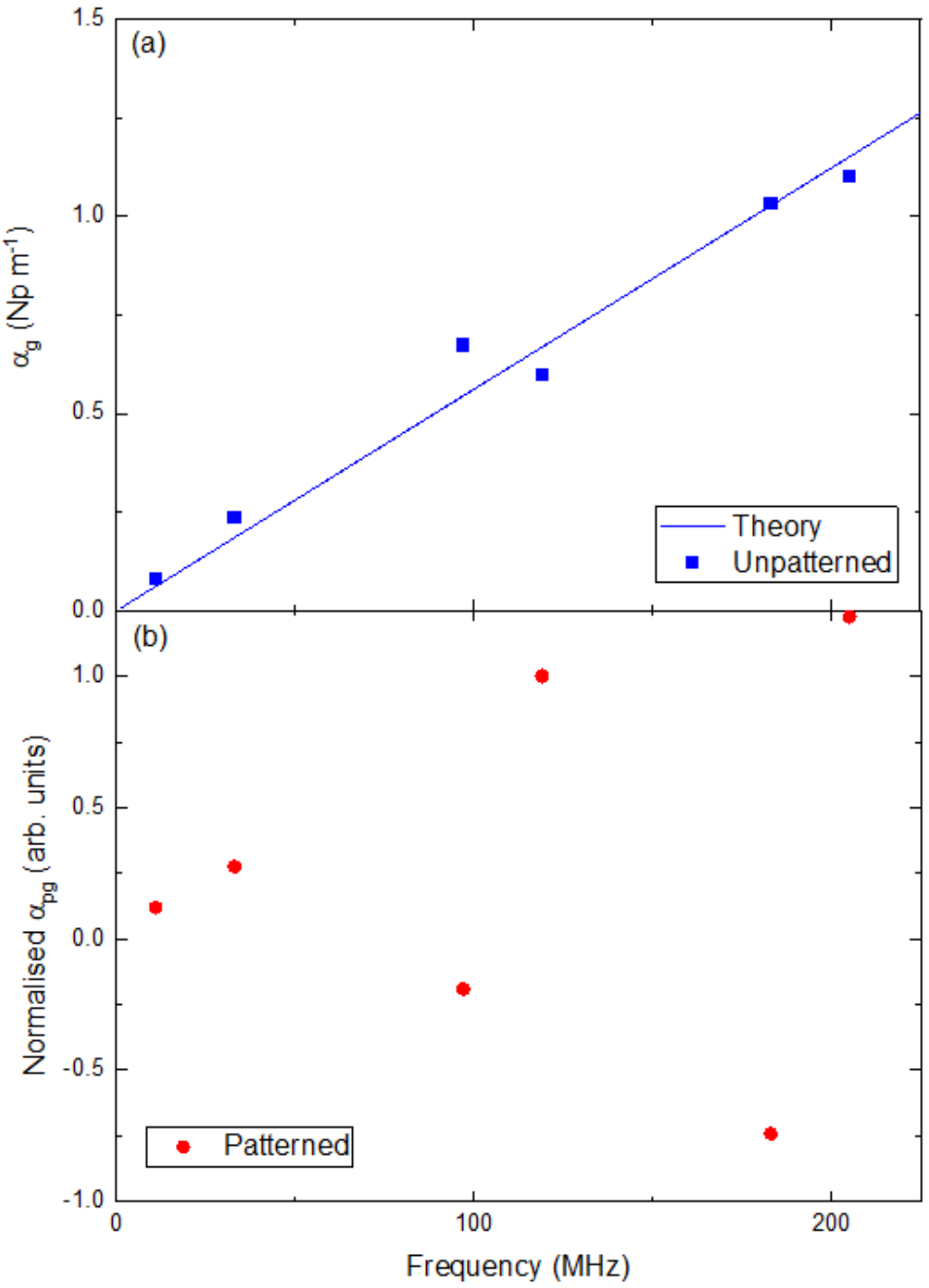

FIGURE 6.11: (a) simulated gas loading attenuation coefficients (symbols), α_g, as a function of frequency for an unpatterned device with the gas loading attenuation for an unpatterned device calculated from the theory (line), and (b) simulated gas loading attenuation due to the resonator array, α_{pg} (symbols), normalised to the value in the simulated bandgap (5 Np m^{-1} at 119 MHz).

magnitude in attenuation due to mass loading was observed at the bandgap

frequency of 97 MHz when a phononic metamaterial (a square array of annular holes) was present, with only 4 resonator elements needed to produce this result. The oscilloscope system and LDV measurements displayed similar frequency dependencies of mass loading attenuation coefficients, although at different orders of magnitude. Some mass loading effects were also reproduced using Finite Element modelling, although at a different bandgap frequency.

Comparisons between this approach and more conventional measures of SAW mass loading (such as via a velocity shift, or through a chemical adsorption layer) are difficult to make without a numerical conversion, nevertheless it appears that these device are extraordinarily sensitive to changes in pressure (between 1 and 3 orders of magnitude depending on the experimental approach) at the bandgap frequency. In addition, devices are straightforward to produce and use, with commercially available substrates, minimal fabrication steps, and standard laboratory equipment. This experimental approach and these devices show great promise for improving the sensitivity of SAW pressure sensors with their adaptability (both in terms of array design and subsequent applications), convenience and ease of fabrication.

Chapter 7

A Spherical Inclusion in a Phononic Metamaterial Array

7.1 Overview

The recent rise in popularity of 'lab-on-a-chip' devices has introduced a need to miniaturise analysis techniques traditionally used in biology, chemistry and medical laboratories. SAW microfluidics has gained increasing interest due to its high compatibility with these systems. Basic SAW devices are compact, versatile and quick to operate, features advantageous for fluid manipulation on the micro-scale. The leaky nature of SAWs means acoustic energy confined on the device surface is transferred into the fluid, meaning fluid manipulation due to the coupling with SAWs is contact-free. It is also straightforward to integrate devices into microfluidic systems, resulting in a vast number of potential applications. SAW microfluidic devices are able to perform a wide variety of types of actuation, including mixing [59], droplet translation [60], jetting [61] and atomisation [62]. They are also capable of biological and chemical sensing, important for biomedical diagnostics.

Acoustophoresis (the manipulation of matter with sound) of microparticles and

cells is a rapidly emerging field due to its easy applicability to biomedical diagnosis. An inherently gentle technique, manipulated particles are not damaged in the process, unlike, for example, in the case of optical tweezers where highly focused laser beams may cause biological cells to lyse. SAWs are an ideal candidate for devices which exploit this phenomenon, as standing SAWs couple into the fluid, generating pressure fields in fluid channels which can trap or focus particles or cells onto pressure nodes [63], allowing for sorting by size or mass, or even for direct probing of the material properties of the cell itself .

It was discussed in Chapters 5 and 6 that SAWs and SAW devices are sensitive to changes in their environment, through the presence of material or gas in and around the surface of phononic metamaterials. In this chapter, a computational study is presented of the SAW bandstructure characteristics and bandgap attenuation of the same phononic metamaterial structure explored in Chapters 5 and 6 (a square array of annular holes), with the addition of a small spherical inclusion within the hole, intended to represent an analogue of a simple cell-like structure. An understanding of the relationships between the SAW bandstructure and the inclusion material properties could inform the realisation of new devices, able to probe biological cells directly and gently, without the need for an external microfluidic system, with a view to integrate similar phononic metamaterial structures into existing techniques for biomedical diagnostics.

7.2 Simulations

7.2.1 Geometry

The model geometry was identical to that of the annular hole geometry in Chapter 5, with the exception of the size and geometry of the inclusion material domain. The cone-shaped inclusion was replaced with a small sphere of radius 0.75 µm on the left hand side of the hole, placed at such a height as to just

touch either side of the hole walls (the centre of the sphere was positioned 1.5 µm below the substrate surface). While it may be small compared to typical biological cells (with the exception of some bacteria), this size was chosen to be compatible with the existing geometry and to be proof of concept. A schematic of the geometry can be seen in Figure 7.1. The inclusion material in the sphere was varied as before with the same 50 combinations of Young Modulus and density, listed in Table 5.1 in Chapter 5.

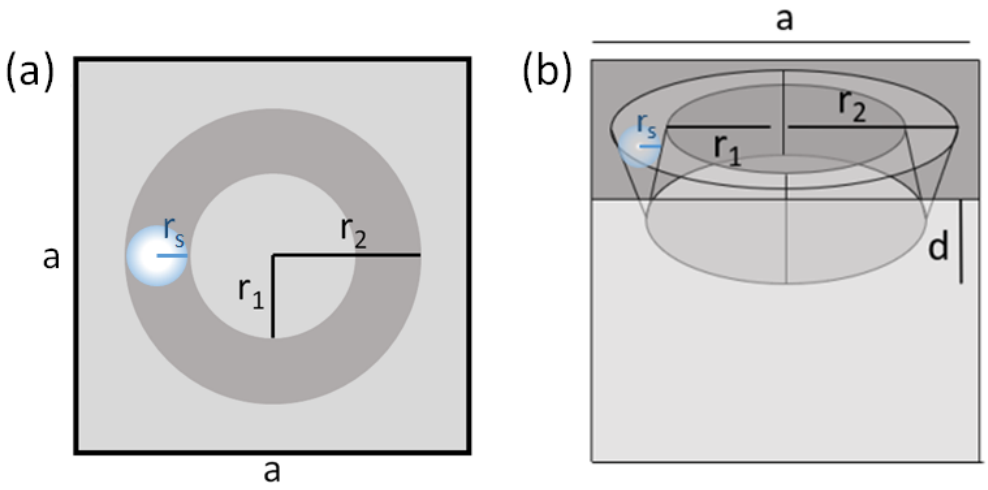

FIGURE 7.1: Not to scale. Schematics of one unit cell of the model geometry, (a) a top down view and (b), a view from the side. The blue shaded domain represents the sphere comprising the inclusion material. As before, the lattice constant a was 12 µm, the depth d was 6 µm, the inner radius r_1 was 2.5 µm and the outer radius r_2 was 4.5 µm. The sphere had a radius r_s of 0.75 µm, and was positioned so its centre was at a depth of 1.5 µm.

7.2.2 Bandstructures

The bandstructures were calculated in exactly the same way as in Chapter 5, as were the Bragg and Mie resonant frequencies for the system. For a sphere of radius r_s in an annular hole of inner radius r_1, outer radius r_2 and lattice constant a, the fundamental resonance frequency due to Bragg scattering along the $\Gamma - X$ path is given by:

$$f_{Bragg} = \frac{V_{avg}}{2a} \tag{7.1}$$

and the expression for the average velocity V_{avg} is given by:

$$V_{avg} = \left(\frac{r_s}{a}\right)^2 V_i + \left(1 - \frac{\pi r_2^2 - \pi r_1^2}{a^2}\right) V_M \tag{7.2}$$

where V_i is the SAW velocity in the inclusion material and V_M is the SAW velocity within the surrounding lithium niobate (approx. 3980 m s^{-1}).

Since the only domain comprising of the inclusion material was the sphere, the fundamental resonance frequency for Mie scattering is given by:

$$f_{Mie} = \frac{V_i}{4r_s} \tag{7.3}$$

where all repeated terms are defined above.

7.2.3 Bandgap Attenuation

The bandgap attenuation model had more permutations for position and hole-filling fraction when a single sphere was present in just one annular hole out of four. To investigate how the position of the hole containing the sphere affected the bandgap attenuation, a single sphere of PMMA was moved between the four holes, then a PMMA sphere was placed in each of the 4 annular holes.

It was found that bandgap attenuation was highest when the annular hole closest to the SAW source contained the sphere, and decreased approximately linearly as the sphere was moved further away. The bandgap attenuation is plotted as a function of hole index (the position of the hole containing the PMMA sphere in relation to the SAW source, where 1 is the closest and 4 is the furthest away) in Figure 7.2. When all four holes contained a PMMA sphere, the attenuation was

slightly lower than when the sphere was closest to the source (indicated by the lower black horizontal line in Figure 7.2). It was assumed that this behaviour was the same for any inclusion material, so only hole index 1 (the hole closest to the SAW source) contained a sphere for all inclusion materials.

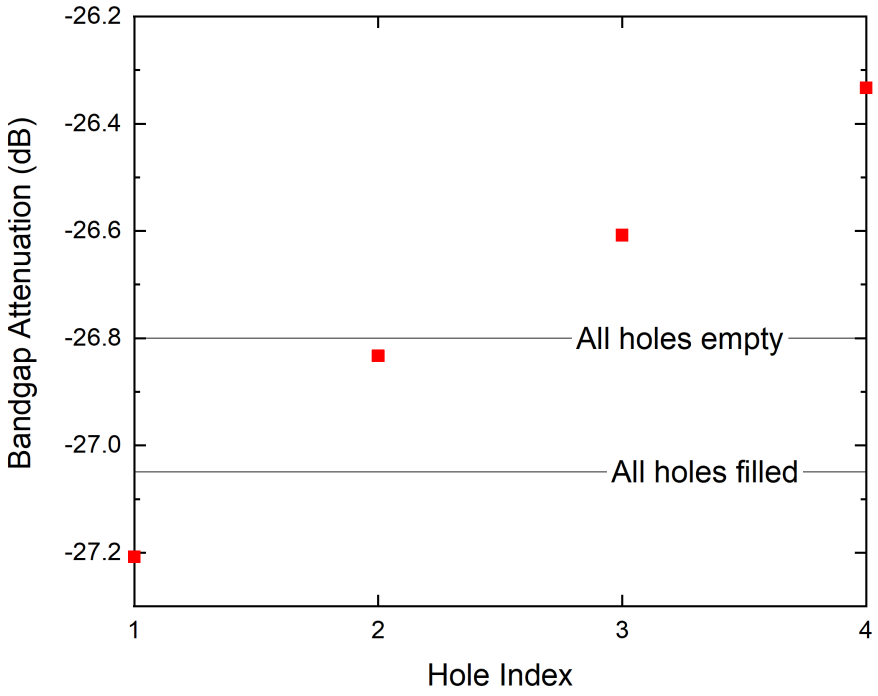

FIGURE 7.2: The bandgap attenuation plotted as a function of hole position index when 1 annular hole out of 4 contains a PMMA sphere. The upper horizontal black line indicates the value of the bandgap attenuation when all 4 annular holes are empty, and the lower horizontal black line indicates the value of the bandgap attenuation when all 4 annular holes contain a PMMA sphere.

Following Chapter 5, the inclusion material was varied in exactly the same way, and the bandgap attenuation Γ was calculated with Equation 7.4 as before.

$$\Gamma = 20 \log_{10} \left(\frac{A_{holes.sphere}}{A_{blank}} \right) \tag{7.4}$$

The sensitivity to the presence of a sphere of material within one of the annular holes was also quantified by calculating the bandgap attenuation coefficient

Γ_{sphere}, the attenuation caused by adding a sphere to one of the annular holes:

$$\Gamma_{sphere} = 20 \log_{10} \left(\frac{A_{holes.sphere}}{A_{holes.empty}} \right) \tag{7.5}$$

7.3 Results

7.3.1 Bandstructures

In Figure 7.3 the calculated central bandgap frequency extracted from the simulated bandstructure is plotted as a function of the inclusion material SAW velocity, V_i, for an annular hole containing a sphere ((a) open blue symbols with dots) and fully-filled annular holes ((b) open red symbols, which is the same data presented in Figure 5.6(b) in Chapter 5). Again, the uncertainty bars represent the simulated upper and lower bandgap limits (in MHz). Values of the predicted bandgap frequency calculated using Equations 7.1 - 7.3 are also plotted in Figure 7.3 as green and magenta lines for Bragg and Mie resonances respectively. Similar to the behaviour observed in Chapter 5, the bandgap centres of the annular holes containing spheres appear to follow at least two distinct velocity regimes, approximately corresponding to the Mie and Bragg resonances calculated from Equations 7.1 - 7.3. At higher V_i above 2500 m s^{-1}, a Bragg regime describes the data well, but at lower V_i deviation from both regimes is observed.

A Mie-like regime appears to occur from 0 to around 750 m s^{-1}, but at a lower gradient than calculated from Equation 7.3, as well as a Bragg-like regime from that point up to around 2000 m s^{-1} at a lower gradient than calculated from Equation 7.1. One reason for this deviation from the calculated Mie regime could be the asymmetry of the unit cell when a sphere is included. Equations 7.1 and 7.3 are also only valid at the unit cell surface. Both the Mie and Bragg resonances were calculated based on a sphere of radius 0.75 µm treated as if it

were at the surface rather than at a depth of 1.5 µm as in the model geometry. In addition, Equations 7.1 and 7.3 do not take the 3D nature of the sphere with regard to the depth into account, so are probably too simplistic to fully describe this scenario. Nevertheless, they enable a comparison between the fully-filled annular holes to be made more easily, but a more in-depth and 3-dimension analytical model may be required to explain the behaviour in more detail.

Indicative mode shapes (viewed from directly above the annular hole so as to see the displacement within the sphere) can be seen at the bandgap limits for four different inclusion materials in Figure 7.4. In almost all the modes, a Mie-like resonance can be seen across the sphere with very little displacement occurring elsewhere in the unit cell, which is in some agreement with the calculated Mie resonance line at lower V_i. The only clearly Bragg-like resonance can be seen in 7.4(h) which is on the Bragg resonance line in Figure 5.6(a), suggesting that true Bragg resonance does indeed occur at higher V_i. However in the overlapping V_i region, neither Mie or Bragg resonance fully describes the mode shapes, indicating a need for a more rigorous approach in reconciling the observed behaviour with an analytical model.

The bandgap centre, however, does have a stronger velocity dependence over the velocity range simulated for spherical inclusions than when the holes are fully-filled, suggesting that predictions may be made about the properties of the inclusion material from the bandstructure and vice versa more easily for spherical inclusions than filling the hole completely. Because of this, annular holes could be a good candidate for probing cell-like analogues trapped within them, and could therefore be adapted for use in biomedical diagnostics.

7.3.2 Transmission

In Figure 7.5 the bandgap attenuation Γ is plotted as a function of inclusion material SAW velocity V_i for a sphere in the index 1 annular hole, and four

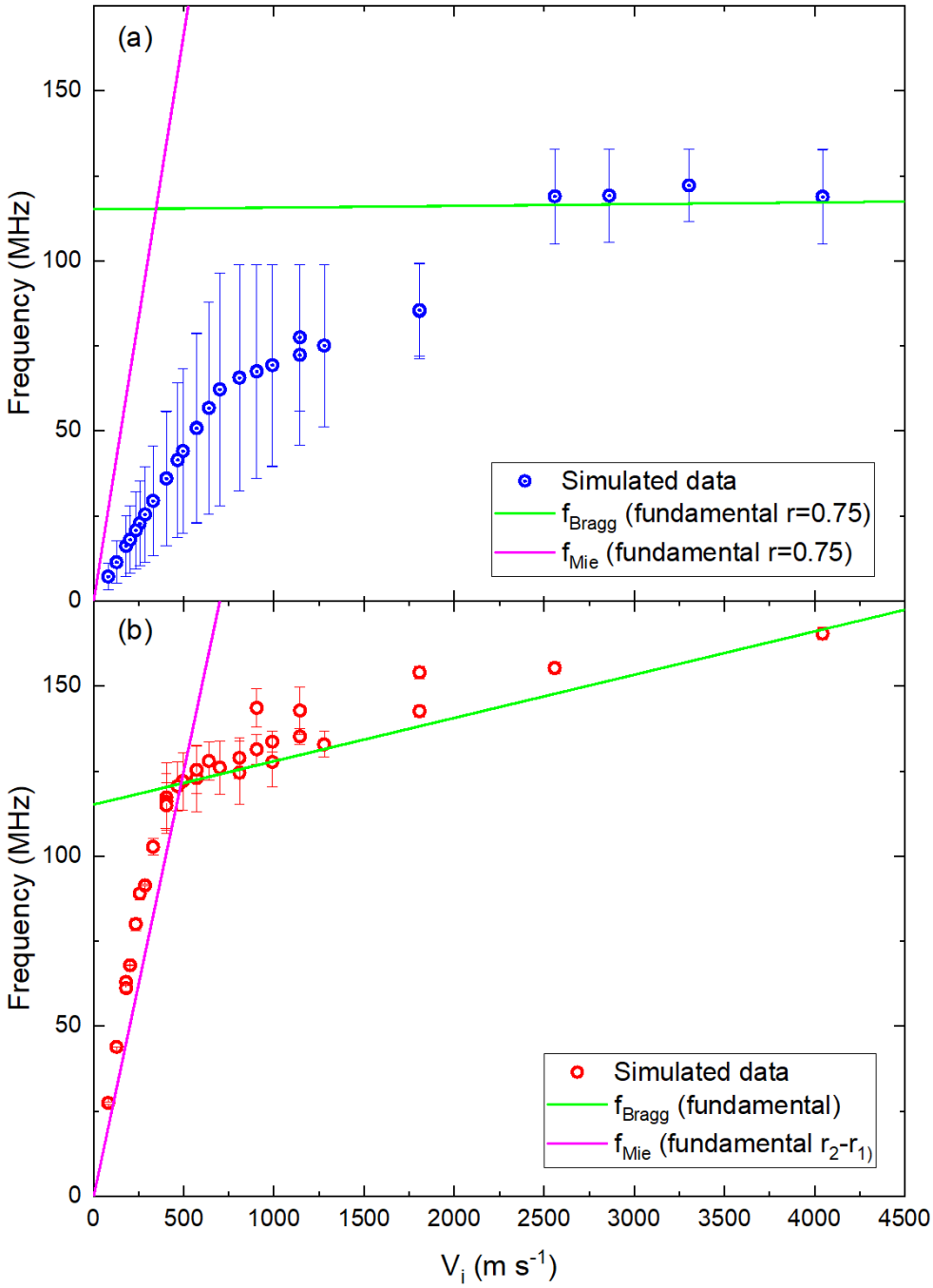

FIGURE 7.3: Central bandgap frequencies as a function of inclusion material SAW velocity V_i for (a) a sphere in an annular hole and (b) fully-filled annular holes, where the uncertainty bars represent the upper and lower bandgap limits. The magenta line in both subfigures represents the relevant Mie resonant regime while the green line represents the relevant Bragg resonant regime.

fully-filled annular holes (the same data presented in Figure 5.11 in Chapter 5). When the annular holes are all completely empty, Γ has a value of -26.8 dB.

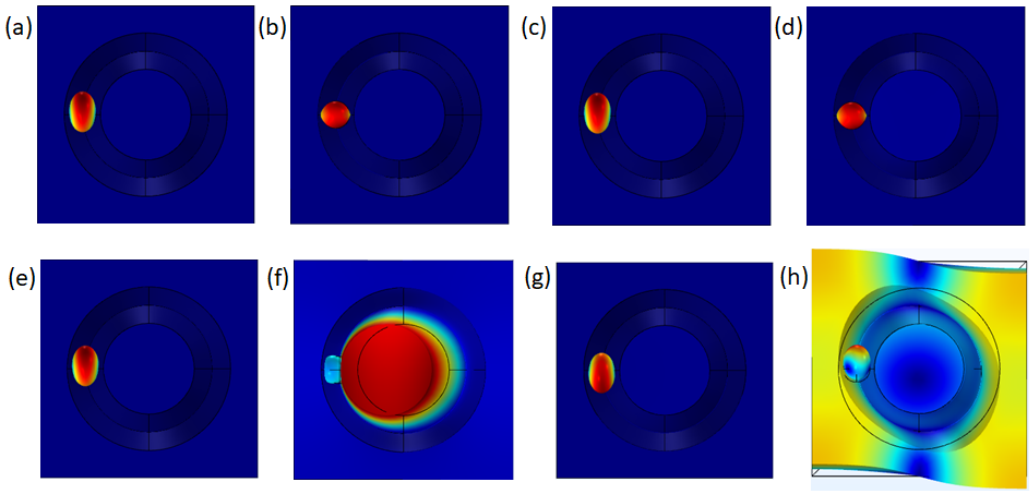

FIGURE 7.4: Indicative mode shapes viewed from directly above the annular hole so as to see the displacement within the sphere, where the darkest red represents the largest displacement while the blue represents the smallest displacement. (a) Material 41 lower bandgap limit, 19 MHz, Mie-like resonance across the sphere, (b) Material 41 upper bandgap limit, 68 MHz, Mie-like resonance across the sphere, (c) Material 39 (border-lining Bragg-like regime in Figure 7.3) lower bandgap limit, 28 MHz, Mie-like resonance across the sphere, (d) Material 39 upper bandgap limit, 96 MHz, Mie-like resonance across the sphere, (e) Material 30 (well within Bragg-like regime in Figure 7.3) lower bandgap limit, 72 MHz, Mie-like resonance across the sphere, (f) Material 30 upper bandgap limit, 99 MHz, displacement concentrated in the pillar with compression of the sphere, (g) Material 23 (well within Bragg regime in Figure 7.3) lower bandgap limit, 111 MHz, Mie-like resonance across the sphere, (h) Material 23 upper bandgap limit, 132 MHz, Bragg resonance across whole unit cell with asymmetrical displacement within the sphere.

Although not immediately obvious, for one sphere in the index 1 annular hole, more bandgap attenuation is observed overall than for four fully-filled annular holes, but the range of values is much smaller, from around -5 dB to around -40 dB compared to around -12 dB to around -63 dB. It can be seen in Figure 7.5(a) that for most values of V_i up to around 2500 m s^{-1}, the bandgap attenuation Γ is around -27 dB, indicating that adding a sphere to the index 1 annular hole does not have much of an effect on the bandgap attenuation in that range V_i. Above 2500 m s^{-1} there is a jump of around 15 dB to around -40 dB, which could correspond to Bragg interference between some of the hole elements as observed in Figure 7.3.

For both spherical inclusions and fully-filled annular holes, the bandgap attenuation tends to increase with increasing velocity. Attenuation is generally larger for the single spherical inclusion compared to the fully-filled annular holes. This is illustrated by plotting the ratio of the bandgap attenuation for the spherical inclusions compared to that in the fully-filled holes, Figure 7.6 which shows that attenuation by the spherical inclusion can be up to around 2x greater than in the fully-filled holes.

In Figure 7.7 the bandgap attenuation coefficient Γ_{sphere} (Equation 7.5, a measure of the sensitivity of the structure to the presence of the spherical inclusion) is plotted as a function of inclusion material SAW velocity V_i for a sphere in the index 1 annular hole, and four fully-filled annular holes (the same data presented in Figure 5.12 in Chapter 5). In Figure 7.7(a), again much less attenuation is observed than for the four fully-filled annular holes, with nearly a third of the values being positive, suggesting that some SAW enhancement occurs at some lower V_i values, with respect to when all the holes are empty. In general, above 1000 m s^{-1}, attenuation values are fairly constant between 0 and -15 dB, compared to a negative correlation with increasing V_i in a range of around -10 to -60 dB observed for fully-filled annular holes.

The ratio of Γ_{sphere} for the spherical inclusion and fully-filled holes is plotted as a function of velocity in Figure 7.8, with values at most velocities being below 1, indicating somewhat intuitively that the annular holes are less sensitive to the presence of a single spherical inclusion than being fully-filled.

The exhibition of higher bandgap attenuation and sensitivity to the presence of materials of different shapes and sizes suggests that the use of annular hole arrays might inform the realisation of devices with greater sensitivity for applications such as biological sensing and lab-on-a-chip diagnostics, without having to integrate complex microfluidic systems or additional analytical processes.

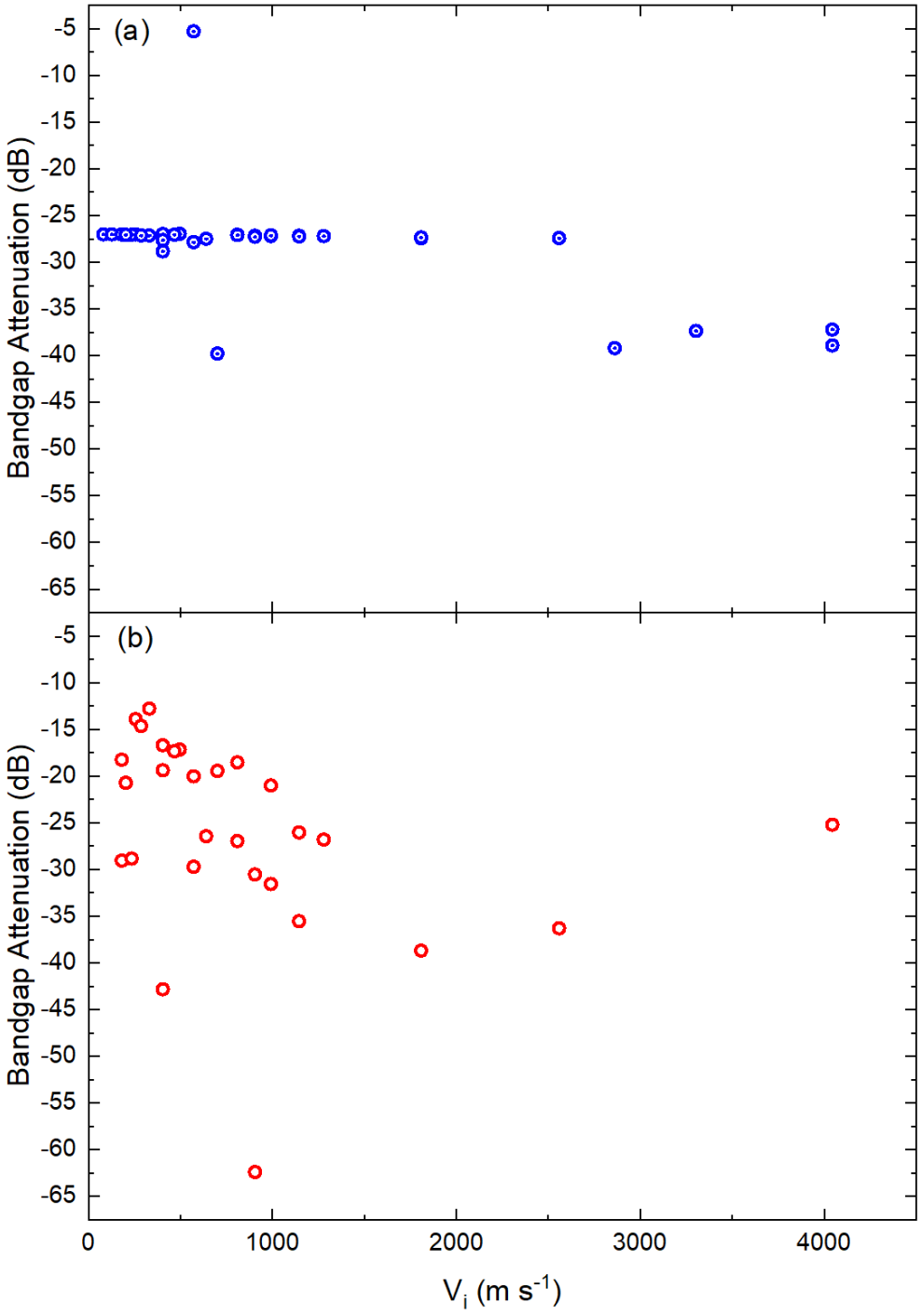

FIGURE 7.5: Bandgap attenuation Γ as a function of inclusion material SAW velocity V_i for (a) a single sphere in index 1 annular hole and (b) four fully-filled annular holes.

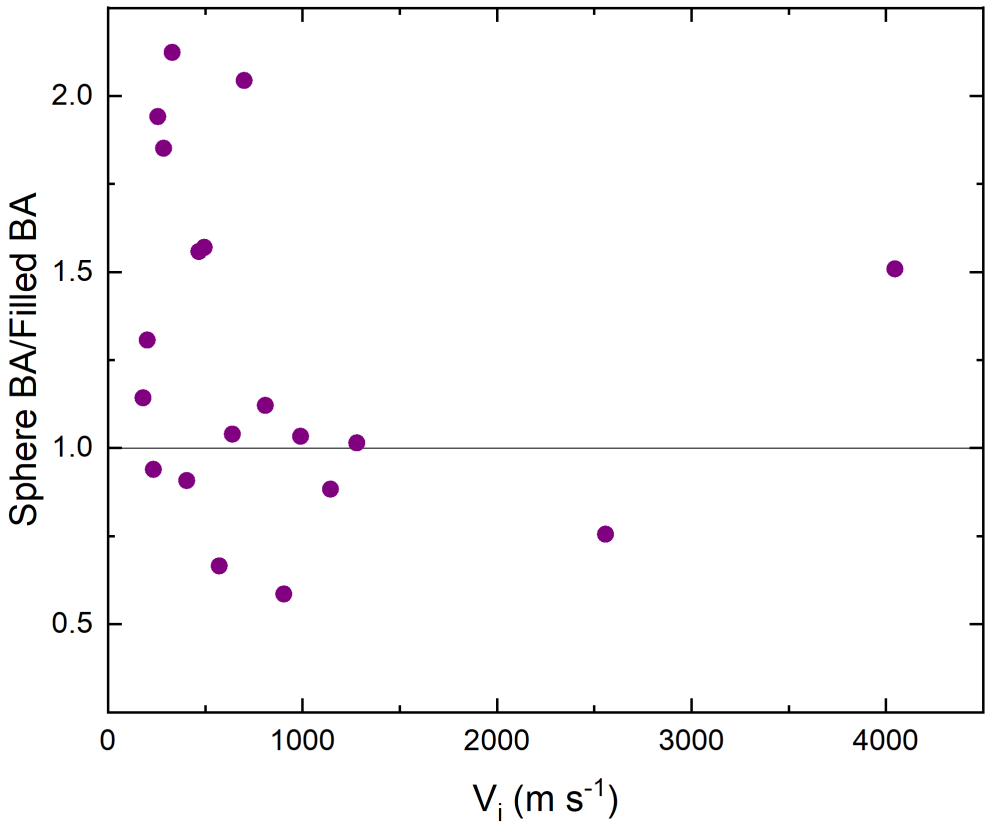

FIGURE 7.6: The ratio of the spherical inclusion bandgap attenuation (Γ) over fully-filled annular hole bandgap attenuation as a function of filling material SAW velocity V_i. Since most of the values are above 1, it is clear that a spherical inclusion exhibits more bandgap attenuation than fully-filled holes.

7.4 Summary

Bandstructures were obtained from finite element simulations for an array of annular holes, as the holes were filled with a small sphere comprised of materials with different SAW velocities V_i. By comparison to bandgap frequencies calculated using an analytical model as in Chapter 5, it was found that the array exhibited a Mie-like scattering regime at lower V_i, a Bragg-like scattering regime at a mid-range of V_i and a true Bragg scattering regime at high V_i. The dependence of the bandgap frequency on the velocity was found to be stronger when the annular holes contained the sphere than for when they are fully-filled, suggesting that the annular holes are potentially a good candidate for probing

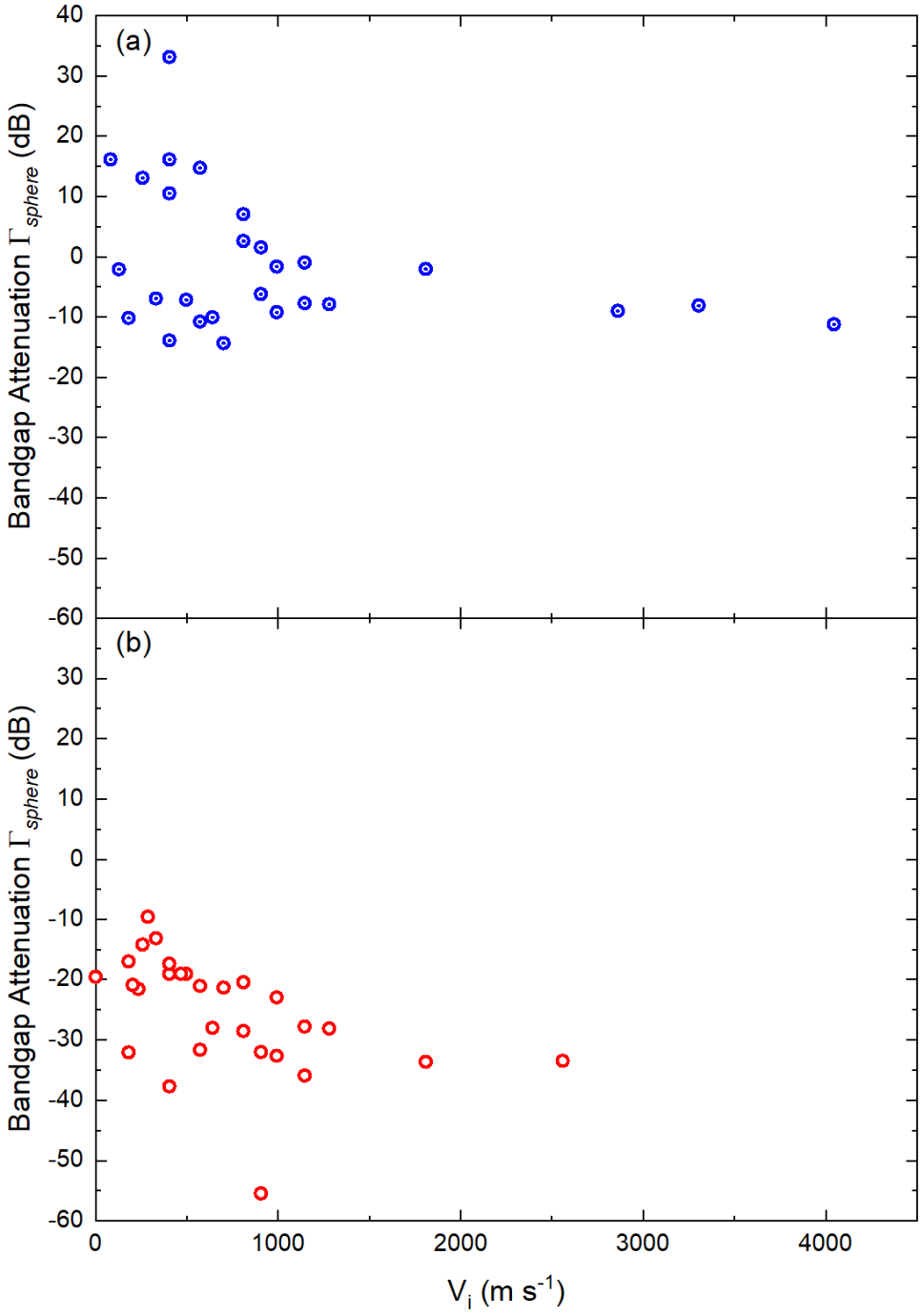

FIGURE 7.7: Bandgap attenuation coefficient Γ_{sphere} as a function of inclusion material SAW velocity V_i, compared to when the holes are empty (as in Equation 5.7) for (a) a single sphere in index 1 annular hole and (b) four fully-filled annular holes.

biological cell-like analogues. The displacement modes within the array were also investigated. At lower values of V_i, the displacements were consistent with Mie scattering across the spherical inclusion. At higher values of V_i, some Bragg

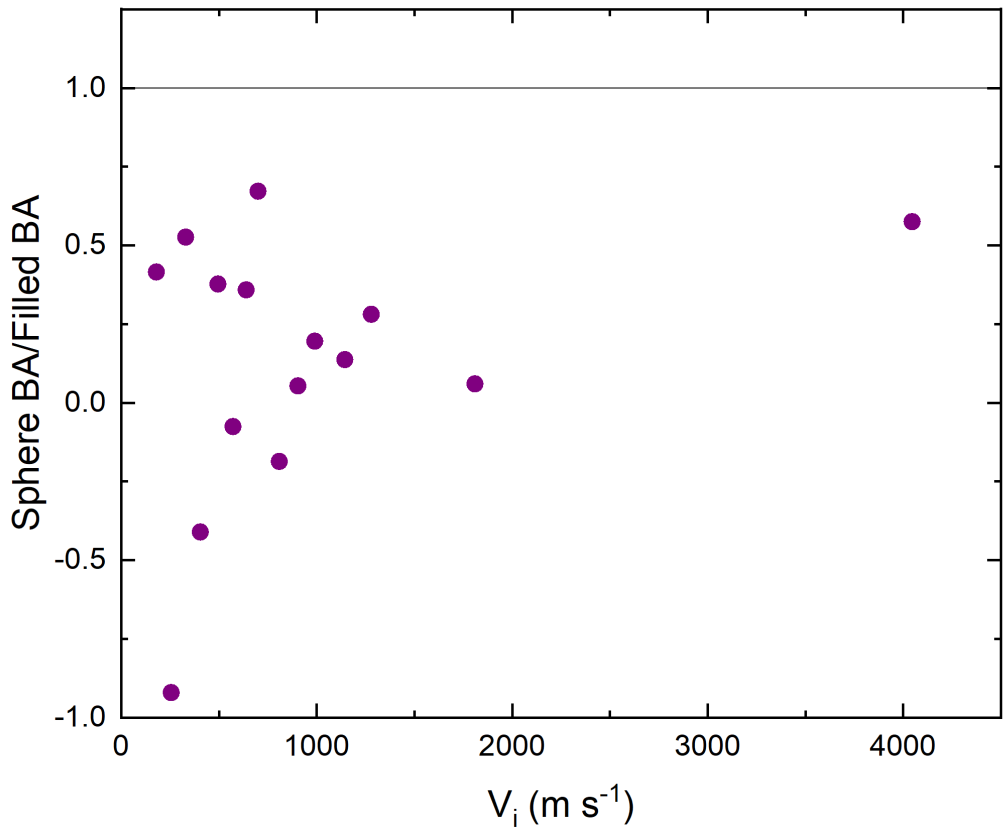

FIGURE 7.8: The ratio of the spherical inclusion bandgap attenuation coefficient (Γ_{sphere}) over fully-filled annular hole bandgap attenuation coefficient (compared to when the holes are empty) as a function of filling material SAW velocity V_i. Since most of the values are below 1, it is clear that annular holes are less sensitive to the presence of a single spherical inclusion compared to being fully-filled.

scattering was observed across the unit cell surface.

The bandgap attenuation was also investigated with a finite element simulation and calculated with respect to either a blank surface or empty holes. In the first case, higher bandgap attenuation was exhibited overall by the single spherical inclusion than by fully-filled holes, by up to a factor of around 2x. In the second case, it was seen that annular holes are less sensitive to the presence of a single spherical inclusion compared to being fully-filled. The use of annular hole arrays might lead to the realisation of devices with greater sensitivity for applications such as biological sensing and lab-on-a-chip diagnostics.

Chapter 8

Conclusions and Outlook

The work described in this thesis focuses on how phononic metamaterial arrays can affect the sensitivity of surface acoustic waves (SAWs) to changes in their environment, by investigating bandstructures, displacement modes, bandgap attenuation and other attenuation coefficients. This was investigated under a number of conditions, firstly with a computational study of inclusion materials in fully-filled cylindrical and annular holes, then with an experimental study of SAW mass loading attenuation on an annular hole device which was recreated in a simulation, and finally with a similar computational study to the first, only that the geometry of the inclusion in the annular hole was modified to be spherical.

Beginning with RF signal processing, SAW interactions and devices have historically had a number of interesting uses but are increasingly attracting attention for sensing applications, as the out-of-plane component of SAW oscillation is susceptible to changes in the local environment. Introducing a pattern on the surface is also known to affect SAW propagation by introducing phononic bandgaps, which prevent specific SAW frequencies from propagating.

The concept of this work was to build upon the findings of Ash et al. [39] who suggested that annular hole arrays could be used for sensing applications, and to

begin to quantify their sensitivity under different conditions. SAW bandstructures were calculated with finite element (FEM) eigenfrequency simulations, and SAW propagation was investigated with FEM frequency domain simulations. Commercially available SAW delay lines, consisting of a lithium niobate substrate with pre-patterned aluminium interdigital transducers, were prepared for focused ion beam milling in a cleanroom environment, and an array of annular holes was patterned within the transducer aperture. Devices were characterised in air at atmospheric pressure and in a vacuum with an oscilloscope system which quantified SAW transmission, and laser Doppler vibrometry which measured SAW amplitudes directly.

The main findings of this work were that the bandstructures of annular holes filled with materials had a higher dependence on the inclusion material SAW velocity and exhibit more bandgap attenuation than when the holes were cylindrical, which suggests that an annular hole array is a good candidate for a tunable phononic metamaterial and for sensing applications. Annular hole devices also exhibited an extraordinary increase in SAW mass loading attenuation compared to unpatterned devices, verified by an oscilloscope measuring system, laser Doppler vibrometry and a computational study. Only 4 hole elements were required for this result. Finally the bandstructures of annular holes filled with a small biological cell-like spherical inclusion had a higher dependence on the inclusion material SAW velocity than when the holes were fully-filled, suggesting that annular holes may be a good candidate for biological sensing and lab-on-a-chip applications. In addition, all of the sensing explored in this thesis took place within the pattern inclusions themselves. This is in contrast to most of the literature, where sensing and probing takes place in or on defects or cavities in the pattern.

In this chapter, the experimental results described in this thesis are summarised, and future work is discussed. The tuning of SAW bandstructures in phononic

crystals and local resonator arrays is reviewed in section 8.1. In section 8.2, mass loading effects in a phononic metamaterial are reviewed and in section 8.3, a review of spherical inclusions in a phononic metamaterial array is presented. Suggestions for future research are discussed in section 8.4.

8.1 Tuning Surface Acoustic Wave Bandstructures in Phononic Crystals and Local Resonator Arrays

Bandstructures were obtained from finite element simulations for arrays of cylindrical and annular holes, as the holes were filled with materials with different SAW velocities V_i. By comparison to bandgap frequencies calculated using an analytical model, it was found that each type of hole array exhibited a Mie scattering regime at lower V_i and a Bragg scattering regime at higher V_i. The dependence of the bandgap frequency on the velocity was found to be higher for the annular holes than for cylindrical holes, suggesting that the annular holes are potentially a better route for creating tuneable phononic metamaterials. The displacement within the arrays was also investigated. At low values of V_i, the displacements were consistent with Mie scattering for both annular and cylindrical holes. At high values of V_i, the displacements in both hole arrays were consistent with Bragg scattering, but in the annular holes displacement of the central pillar could also be seen.

The bandgap attenuation was also investigated with a finite element simulation and calculated with respect to either a blank surface or empty holes. In both cases the annular holes displayed a higher bandgap attenuation, by up to a factor of 3x compared to the attenuation in arrays of cylindrical holes. The largest difference in the attenuation between the two types of arrays was at the SAW velocity when both Mie and Bragg scattering are thought to contribute

to the formation of a bandgap, suggesting that it might be the greater number of interfaces in the annular holes that lead to this greater attenuation. The use of annular hole arrays might lead to greater sensitivity in devices designed for applications such as mass loading sensing.

8.2 Mass Loading Effects in a Phononic Metamaterial

SAW attenuation due to mass loading of air was obtained by directly measuring SAW amplitude on a SAW device using an oscilloscope system and by laser Doppler vibrometry (LDV). An extraordinary increase of 2 to 3 orders of magnitude in attenuation due to mass loading was observed at the bandgap frequency of 97 MHz when a phononic metamaterial (a square array of annular holes) was present, with only 4 resonator elements needed to produce this result. The oscilloscope system and LDV measurements displayed similar frequency dependencies of mass loading attenuation coefficients, although at different orders of magnitude. Some mass loading effects were also reproduced using finite element modelling, although at a different bandgap frequency.

Comparisons between this approach and more conventional measures of SAW mass loading (such as via a velocity shift, or through a chemical adsorption layer) are difficult to make without a numerical conversion, nevertheless it appears that these device are extraordinarily sensitive to small changes in pressure (between 1 and 3 orders of magnitude depending on the experimental approach) at the bandgap frequency. In addition, devices are straightforward to produce and use, with commercially available substrates, minimal fabrication steps, and standard laboratory equipment. It is believed that this experimental approach and these devices show great promise for improving the sensitivity of SAW pressure sensors with their adaptability (both in terms of array design and

subsequent applications), convenience and ease of fabrication.

8.3 A Spherical Inclusion in a Phononic Metamaterial Array

Bandstructures were obtained from finite element simulations for an array of annular holes, as the holes were filled with a small sphere comprised of materials with different SAW velocities V_i. By comparison to bandgap frequencies calculated using an analytical model as in Chapter 5, it was found that the array exhibited a Mie-like scattering regime at lower V_i, a Bragg-like scattering regime at a mid-range of V_i and a true Bragg scattering regime at high V_i. The dependence of the bandgap frequency on the velocity was found to be stronger when the annular holes contained the sphere than for when they are fully-filled, suggesting that the annular holes are potentially a good candidate for probing biological cell-like analogues. The displacement modes within the array were also investigated. At lower values of V_i, the displacements were consistent with Mie scattering across the spherical inclusion. At higher values of V_i, some Bragg scattering was observed across the unit cell surface.

The bandgap attenuation was also investigated with a finite element simulation and calculated with respect to either a blank surface or empty holes. In the first case, higher bandgap attenuation was exhibited overall by the single spherical inclusion than by fully-filled holes, by up to a factor of around 2x. In the second case, it was seen that annular holes are less sensitive to the presence of a single spherical inclusion compared to being fully-filled. The use of annular hole arrays might lead to the realisation of devices with greater sensitivity for applications such as biological sensing and lab-on-a-chip diagnostics.

8.4 Future Work

8.4.1 Tuneable Phononic Metamaterials

An obvious next step for the work carried out in Chapters 5 and 7 would be to fabricate the systems and characterise them experimentally in order to validate behaviours observed in simulations. However, difficulty may be posed in filling the holes perfectly, particularly for the spherical inclusions, and of course many of the inclusion materials investigated in simulations do not exist in reality. In addition, the particular SAW device substrate used in Chapter 6 exploit a specific design of pre-patterned IDT, which only generate SAWs at discrete frequencies. Chirped IDTs allow for finer control of the SAW frequencies generated, which would allow for more accurate identification of bandgap limits.

One key limitation encountered in Chapter 7 was the geometrical applicability of the analytical model used to describe simulation results in Chapter 5. In addition, only two scattering mechanisms (Mie and Bragg) were considered. For all inclusion geometries (cylindrical, annular and spherical), developing a more rigorous analytical approach, valid at all length scales and depths and which takes into account the 3D nature of the system, would allow for a more predictable relationship between inclusion material SAW velocity V_i and central bandgap frequency, with a full description of the behaviour and resonance regimes.

A more thorough understanding of the dependence on the bandgap on inclusion material characteristics, not just material properties such as elastic moduli but also the geometry, would enable the realisation of tuneable SAW devices. Finer control over the tuning could lead to applications in frequency filters for telecommunications.

8.4.2 Phononic Metamaterials for Pressure Sensing

The experimental system in Chapter 6 has only been characterised at two discrete pressures, atmospheric pressure and vacuum. An investigation into the limits of its sensitivity, such as to incremental changes up to and beyond atmospheric pressure may inform its potential integration into more complicated and battery-less pressure sensing systems such as those already used for TPMS (Tyre Pressure Monitoring Systems) for the safety and efficiency of car tyres [64].

The mass loading simulations attempted in Chapter 6 also may have uncovered limitations of how COMSOL handles some multiphysics interfaces for some specific applications. Further computational investigation is certainly needed, either with COMSOL or an alternative modelling approach, FEM or otherwise.

8.4.3 Phononic Metamaterials for Biological Sensing

This technique is expected to be sensitive to some physical properties of cells (particularly red blood cells), such as elasticity, which tend to be compromised in disease due to factors such as oxidative stress as well as cell shape. This can manifest in a number of conditions, including sickle cell anaemia [65], spherocytosis [66] and malaria [67]. An obvious follow-up study to those in Chapters 5 and 7 would be to scale up the hole geometry to a more comparable size. For example, for a red blood cell with a diameter of 8 µm, an annular width of at least that is required in order for it to fit inside the hole for probing of its material properties. Only simplistic inclusion geometries have been considered so far, so more complex shapes (e.g. the biconcave red blood cell). If an annular hole system is to be used for probing real biological cells, then knowing the dependence of the bandgap on V_i and other material parameters again may allow biomedical diagnosis to be reached easily and accurately.

Scaling and fabricating the system described in Chapter 7 so a real red blood cell would fit in the inclusion could also be a potential avenue to be explored, using a larger annular hole system to probe the material properties and overall health of the cell. This naturally leads on to integrating annular holes into a microfluidic, acoustophoretic system for lab-on-a-chip applications, potentially allowing for greater control of SAWs coupling into fluid in microchannels, and subsequent applications in manipulation, detection and investigation of fluid, particles or biological cells.

Bibliography

[1] L. Rayleigh, "On waves propagated along the plane surface of an elastic solid", Proceedings of the London Mathematical Society **s1-17**, 4–11 (1885).

[2] H. Lamb, "On the vibrations of an elastic sphere", Proceedings of the London Mathematical Society **s1-13**, 189–212 (1881).

[3] A. E. H. Love, *Some problems of geodynamics* (Cambridge University Press, 1911).

[4] C. Campbell, *Surface acoustic wave devices for mobile and wireless communications* (San Diego Academic Press, 1981).

[5] R. M. White and F. W. Voltmer, "Direct piezoelectric coupling to surface elastic waves", Applied Physics Letters **7**, 314–316 (1965).

[6] M. S. Kushwaha, P. Halevi, L. Dobrzynski, and B. Djafari-Rouhani, "Acoustic band structure of periodic elastic composites", Phys. Rev. Lett. **71**, 2022–2025 (1993).

[7] M. Sigalas and E. N. Economou, "Band structure of elastic waves in two dimensional systems", Solid State Communications **86**, 141–143 (1993).

[8] E. N. Economou and M. Sigalas, "Stop bands for elastic waves in periodic composite materials", The Journal of the Acoustical Society of America **95**, 1734–1740 (1994).

[9] W. H. Bragg and W. L. Bragg, "The reflection of x-rays by crystals", Proceedings of the Royal Society of London. Series A, Containing Papers of a Mathematical and Physical Character **88**, 428–438 (1913).

[10] Y. P. Zhao and P. Wei, "The band gap of 1d viscoelastic phononic crystal", Computational Materials Science **46**, 603–606 (2009).

[11] M. Zubtsov, R. Lucklum, M. Ke, A. Oseev, R. Grundmann, B. Henning, and U. Hempel, "2d phononic crystal sensor with normal incidence of sound", Sensors and Actuators A Physical **186**, 118–124 (2012).

[12] F. De Espinosa, E. Jimeniz, and M. Torres, "Experimental assessment of an ultrasonic band gap in a periodic two-dimensional composite", **1**, 537–540 vol.1 (1997).

[13] J. O. Vasseur, P. A. Deymier, B. Chenni, B. Djafari-Rouhani, L. Dobrzynski, and D. Prevost, "Experimental and theoretical evidence for the existence of absolute acoustic band gaps in two-dimensional solid phononic crystals", Phys. Rev. Lett. **86**, 3012–3015 (2001).

[14] Y. Tanaka and S.-i. Tamura, "Surface acoustic waves in two-dimensional periodic elastic structures", Phys. Rev. B **58**, 7958–7965 (1998).

[15] V. Laude, M. Wilm, S. Benchabane, and A. Khelif, "Full band gap for surface acoustic waves in a piezoelectric phononic crystal", Phys. Rev. E **71**, 036607 (2005).

[16] G. Mie, "Beiträge zur Optik trüber Medien, speziell kolloidaler Metallösungen", Annalen der Physik **330**, 377–445 (1908).

[17] R. H. Olsson and I. El-Kady, "Microfabricated phononic crystal devices and applications", Measurement Science and Technology **20**, 012002 (2008).

[18] Z. Liu, X. Zhang, Y. Mao, Y. Zhu, Z. Yang, C. T. Chan, and P. Sheng, "Locally resonant sonic materials", Science **289**, 1734–1736 (2000).

[19] Z. Liu, C. T. Chan, P. Sheng, A. L. Goertzen, and J. H. Page, "Elastic wave scattering by periodic structures of spherical objects: theory and experiment", Physical Review B **62**, 2446–2457 (2000).

[20] R. Sainidou, B. Djafari-Rouhani, Y. Pennec, and J. O. Vasseur, "Locally resonant phononic crystals made of hollow spheres or cylinders", Phys. Rev. B **73**, 024302 (2006).

[21] A. Khelif, Y. Achaoui, S. Benchabane, V. Laude, and B. Aoubiza, "Locally resonant surface acoustic wave band gaps in a two-dimensional phononic crystal of pillars on a surface", Phys. Rev. B **81**, 214303 (2010).

[22] Z. Jia, Y. Chen, H. Yang, and L. Wang, "Designing phononic crystals with wide and robust band gaps", Phys. Rev. Applied **9**, 044021 (2018).

[23] K. L. S. Yip and S. John, "Acoustic modes of locally resonant phononic crystals: comparison with frequency-dependent mass models", Phys. Rev. B **103**, 094304 (2021).

[24] Y. Achaoui, A. Khelif, S. Benchabane, L. Robert, and V. Laude, "Experimental observation of locally-resonant and bragg band gaps for surface guided waves in a phononic crystal of pillars", Phys. Rev. B **83**, 104201 (2011).

[25] K. Sellami, H. Ketata, and M. H. Ben Ghozlen, "Locally resonant phononic crystals band-gap analysis on a two dimensional phononic crystal with a square and a triangular lattice", Optical and Quantum Electronics **51** (2019).

[26] Y. Achaoui, V. Laude, S. Benchabane, and A. Khelif, "Local resonances in phononic crystals and in random arrangements of pillars on a surface", Journal of Applied Physics **114**, 104503 (2013).

[27] J. B. Pendry, "Negative refraction", Contemporary Physics **45**, 191–202 (2004).

[28] V. G. Veselago, "The Electrodynamics of Substances with Simultaneously Negative Values of ϵ and μ", Soviet Physics Uspekhi **10**, 509 (1968).

[29] S. A. Cummer, J. Christensen, and A. Alú, "Controlling sound with acoustic metamaterials", Nature Reviews Materials **1**, 16001 (2016).

[30] J. Li and C. T. Chan, "Double-negative acoustic metamaterial", Physical Review E **70**, 055602 (2004).

[31] M.-H. Lu, L. Feng, and Y.-F. Chen, "Phononic crystals and acoustic metamaterials", Materials today **12**, 34–42 (2009).

[32] D. Mandal and S. Banerjee, "Surface acoustic wave (saw) sensors: physics, materials, and applications", Sensors **22**, 820 (2022).

[33] B. Liu, X. Chen, H. Cai, M. M. Ali, X. Tian, L. Tao, Y. Yang, and T. Ren, "Surface acoustic wave devices for sensor applications", Journal of semiconductors **37**, 021001 (2016).

[34] A. J. Slobodnik, "Attenuation of microwave acoustic surface waves due to gas loading", Journal of Applied Physics **43**, 2565–2568 (1972).

[35] A. Mehaney, "Biodiesel physical properties detection using one-dimensional phononic crystal sensor", Acoustical Physics **65**, 374–378 (2019).

[36] A. Khaligh, A. Bahrami, and H. Badri Ghavifekr, "Phononic crystal locally-resonant cavity for detecting vinegar acidity", Journal of Molecular Liquids **343**, 116972 (2021).

[37] H. Gharibi, A. Khaligh, A. Bahrami, and H. Badri, "A very high sensitive interferometric phononic crystal liquid sensor", Journal of Molecular Liquids **296**, 111878 (2019).

[38] A. Mehaney, H. Gharibi, and A. Bahrami, "Phononic eco-sensor for detection of heavy metals pollutions in water with spectrum analyzer", IEEE Sensors Journal **21**, 6733–6740 (2020).

[39] B. J. Ash, S. R. Worsfold, P. Vukusic, and G. R. Nash, "A highly attenuating and frequency tailorable annular hole phononic crystal for surface acoustic waves", Nature Communications **8** (2017).

[40] D. Morgan, *Surface acoustic wave filters with applications to electronic communications and signal processing*, 2nd ed. (London Academic Press, 2007).

[41] R. M. Arzt, E. Salzmann, and K. Dransfeld, "Elastic surface waves in quartz at 316 mhz", Applied Physics Letters **10**, 165–167 (1967).

[42] J. Koskela, J. Knuuttila, T. Makkonen, V. Plessky, and M. Salomaa, "Acoustic loss mechanisms in leaky saw resonators on lithium tantalate", IEEE Transactions on Ultrasonics, Ferroelectrics, and Frequency Control **48**, 1517–1526 (2001).

[43] A. Nath, A. Sudeepthi, and A. K. Sen, "Trapping of aqueous droplets under surface acoustic wave-driven streaming in oil-filled microwells", Langmuir **38**, 4763–4773 (2022).

[44] V. Laude, "Principles and properties of phononic crystal waveguides", APL Materials **9**, 080701 (2021).

[45] S.-W. Fan, S.-D. Zhao, L. Cao, Y. Zhu, A.-L. Chen, Y.-F. Wang, K. Donda, Y.-S. Wang, and B. Assouar, "Reconfigurable curved metasurface for acoustic cloaking and illusion", Physical Review B **101**, 024104 (2020).

[46] O. C. Zienkiewicz, R. L. Taylor, and J. Z. Zhu, *The finite element method: its basis and fundamentals* (Butterworth Heinemann, 2013).

[47] *Comsol multiphysics reference manual* (2019).

[48] *'setup and meshing of infinite elements, perfectly matched layers, and absorbing layers', comsol support blog, https://www.comsol.com/support/knowledgebase/1272.*

[49] A. Taflove and S. C. Hagenss, *Computational electrodynamics: the finite-difference time-domain method*, 2nd ed. (Boston Artech House, 2000).

[50] W. Frei, *'using perfectly matched layers and scattering boundary conditions for wave electromagnetics problems', comsol support blog, https://www.comsol.com/ blogs /using-perfectly-matched-layers-and-scattering-boundary-conditions-for-wave- electromagnetics-problems*, 2015.

[51] M. Badreddine Assouar and M. Oudich, "Dispersion curves of surface acoustic waves in a two-dimensional phononic crystal", Applied Physics Letters **99**, 123505 (2011).

[52] R. Weis and T. Gaylord, "Lithium niobate: summary of physical properties and crystal structure", Applied Physics A **37**, 191–203 (1985).

[53] L. Brits, *'euler angles', https://en.wikipedia.org/wiki/euler_angles*, 2008.

[54] A. J. Slobodnik and E. D. Conway, *Microwave acoustics handbook volume 1. surface wave velocities* (Bedford, Massuchusetts, 1970).

[55] M.-I. Rocha-Gaso, C. March-Iborra, Á. Montoya-Baides, and A. Arnau-Vives, "Surface generated acoustic wave biosensors for the detection of pathogens: a review", Sensors **9**, 5740–5769 (2009).

[56] E. P. Tomasini, G. M. Revel, and P. Castellini, *Encyclopedia of vibration, volumes 1-3: laser doppler vibrometry technique* (Elsevier, 2002).

[57] V. Kyrimi, B. Ash, and G. Nash, "A metasurface comprising spiral shaped local resonators for surface acoustic waves", Journal of Physics D: Applied Physics **52**, 345306 (2019).

[58] M. Kumar and D. Bhadu, "Design performance and frequency response analysis of saw-based sensor for dichloromethane gas sensing amidst the covid-19", Journal of Vibration Engineering Technologies **9**, 725–732 (2021).

[59] R. Shilton, M. K. Tan, L. Y. Yeo, and J. R. Friend, "Particle concentration and mixing in microdrops driven by focused surface acoustic waves", Journal of Applied Physics **104**, 014910 (2008).

[60] A. Wixforth, "Acoustically driven planar microfluidics", Superlattices and Microstructures **33**, 389–396 (2003).

[61] M. K. Tan, J. R. Friend, and L. Y. Yeo, "Interfacial jetting phenomena induced by focused surface vibrations", Phys. Rev. Lett. **103**, 024501 (2009).

[62] M. Kurosawa, T. Watanabe, A. Futami, and T. Higuchi, "Surface acoustic wave atomizer", Sensors and Actuators-A-Physical Sensors **50**, 69–74 (1995).

[63] J. Shi, X. Mao, D. Ahmed, A. Colletti, and T. J. Huang, "Focusing microparticles in a microfluidic channel with standing surface acoustic waves (ssaw)", Lab on a Chip **8**, 221–223 (2008).

[64] A. Kubba and K. Jiang, "A comprehensive study on technologies of tyre monitoring systems and possible energy solutions", Sensors **14**, 10306–10345 (2014).

[65] X. Li, M. Dao, G. Lykotrafitis, and G. E. Karniadakis, "Biomechanics and biorheology of red blood cells in sickle cell anemia", Journal of Biomechanics **50**, 34–41 (2017).

[66] R. Huisjes, A. Makhro, E. Llaudet-Planas, L. Hertz, P. Petkova-Kirova, L. P. Verhagen, S. Pignatelli, M. A. Rab, R. M. Schiffelers, E. Seiler, and et al., "Density, heterogeneity and deformability of red cells as markers of clinical severity in hereditary spherocytosis", Haematologica **105**, 338–347 (2020).

[67] N. Mohandas and X. An, "Malaria and human red blood cells", Medical Microbiology and Immunology **201**, 593–598 (2012).